ANALYSIS OF THE DAY SIDE EQUATORIAL ANOMALY

by

Jayaprabha Shankar

A thesis submitted in partial fulfillment
of the requirements for the degree

of

MASTER OF SCIENCE

in

Electrical Engineering

Approved:

Dr. Charles M. Swenson Major Professor	Dr. Todd K. Moon Committee Member
Dr. Wei Ren Committee Member	Dr. Byron R. Burnham Dean of Graduate Studies

UTAH STATE UNIVERSITY
Logan, Utah

2007

Abstract

Analysis of the Day Side Equatorial Anomaly

by

Jayaprabha Shankar, Master of Science

Utah State University, 2007

Major Professor: Dr. Charles M. Swenson
Department: Electrical and Computer Engineering

Equatorial Ionization Anomaly (EIA) is a region of peak plasma density found at ± 10 ° to 20 ° magnetic latitudes at F-region altitudes. In 2002, NASA launched the Global Ultra Violet Imager (GUVI), which can observe the EIA at various local times, longitudes, and seasons by the glow of the recombining electrons and ions in the plasma. This thesis presents the observations of the geomagnetic quiet time EIA and its global behavior at all local times using 1356 Å radiance data from high altitude GUVI limb scans. Limb data is prepared for analysis using reduction techniques that remove from the limb file, contaminating signatures of stars, glints, and low altitude day time neutral atmosphere emissions. A simple comparison of the subtracted data at different local times, longitudes, seasons, and magnetic activity reveals significant EIA variability with each of these factors. A global morphology of the quiet time EIA is developed using metrics such as the peak latitude and peak radiance, extracted from the EIA structures. The study shows that the EIA develops gradually in the day, peaking between 1100 to 1400 hours LT, and falls in the night time. Signatures of the prereversal drift enhancement due to enhanced post-sunset F-region vertical drifts appear during December solstice seasons between 19:00 to 21:00 local time. The GUVI EIA observations are compared with 1356 Å radiance data simulated from electron densities predicted by ionospheric models, namely USUGAIM and

TIMEGCM. Results show that the models overestimate the radiance values by a small amount. However, the EIA variability with local time and longitudes as predicted by the models compares well with the GUVI observations.

(104 pages)

To my loving parents...

Acknowledgments

Foremost, I thank my advisor, Dr. Charles M. Swenson, for his invaluable role in this research work. He has constantly steered my efforts in the right direction and has been ever helpful with solutions when I needed them most. I am thankful for the pool of resources, guidance and encouragement that he has given me all through this study.

A great deal of contribution to this work comes from Sid Henderson, as a number of his methodologies and routines have been borrowed in this thesis. Steve Burr, my fellow colleague and undergraduate student, shares a great deal of credit for this project. He takes credit for the data reduction procedures and has also collaborated extensively for other modules. I would especially like to thank him for his ever willingness to help and commitment towards this research work. I thank Dr. Todd K. Moon for his crucial ideas and Henry Coakley for his contribution during the initial stages of this project. I also thank Dr. Todd K. Moon and Dr. Wei Ren for their valuable time and effort as faculty members on my thesis committee.

I acknowledge the GUVI team, especially Dr. Andy Christensen, Dr. Larry Paxton and Dr. Robert Meier, for their ideas and comments during the review meetings, which have been pivotal in taking the study forward. I would also like to thank Geoff Crowley, Don Thompson, and Ludger Scherliess for providing me with data from TIMEGCM and USUGAIM models and for patiently answering my queries on the model data as well as the physical processes involved. I thank everyone here in my student office and friends at Utah State University, who have lent me their precious time and support from time to time. Lastly, I am grateful to my dear friends and family whose love and support have kept me going all through my master's study.

Jayaprabha Shankar

Contents

Page

Abstract . . . **iii**

Acknowledgments . . . **vi**

List of Tables . . . **ix**

List of Figures . . . **x**

Acronyms . . . **xv**

1 Introduction . . . **1**
1.1 The Equatorial Ionization Anomaly (EIA) . . . 1
1.1.1 E-region Dynamo . . . 4
1.1.2 F-region Dynamo . . . 6
1.2 Factors Affecting the EIA . . . 7
1.2.1 Magnetic Equator . . . 7
1.2.2 F-region Neutral Winds . . . 8
1.2.3 Solar Flux . . . 9
1.2.4 Quiet and Disturbed Magnetic Periods . . . 9
1.3 Ionospheric Processes . . . 10
1.3.1 Ionospheric Photo Emissions . . . 10
1.3.2 Photoelectron Impact Ionization . . . 11
1.4 Ionospheric Models . . . 12
1.5 Instrument and Data . . . 13
1.5.1 GUVI Instrument . . . 13
1.5.2 GUVI Data . . . 14
1.6 Thesis Objective . . . 17

2 Processing GUVI Limb Files . . . **20**
2.1 GUVI Limb File . . . 20
2.2 Features in a Limb File . . . 21
2.3 Data Reduction . . . 23
2.3.1 Emissions Due to Stars and Glints . . . 23
2.3.2 Emissions Due to Photoelectron Impact Ionization . . . 24
2.4 Discussion . . . 29
2.5 Day-to-day Variability of the EIA . . . 35

3 Comparison of GUVI 1356 Å Radiance with Ionospheric Models 42
3.1 Introduction 42
3.2 Radiometric Analysis 42
3.3 Construction of 1356 Å Radiance Profiles from Model Data 46
3.4 Discussion of Comparison Results 49
3.5 Development of EIA in GAIM with Local Time and Longitude 51

4 Observations with GUVI Limb Data 58
4.1 EIA Parameters 58
4.2 GUVI Limb Data Classification 59
4.3 EIA Variability with Local Time 61
4.4 EIA Variability with Longitude 63
4.5 EIA Variability with Season 65
4.6 EIA Variability with Solar Activity 69

5 Summary and Future Work 71
5.1 Summary 71
5.2 Future Work 71
5.2.1 Binning GUVI Limb Files 72
5.2.2 Dayglow Subtraction Using Neutral Density Profiles 73
5.2.3 Longitudinal Variation in Day Time EIA Morphology 76

References 78

Appendices 80
Appendix A EIA Morphology for Years 2003 and 2005 81
A.1 Longitudinal Variation in 2003 81
A.2 Seasonal Variation in 2003 83
A.3 Longitudinal Variation in 2005 85
A.4 Seasonal Variation in 2005 87
Appendix B Movies with GUVI Limb Files 89

List of Tables

Table Page

2.1 Factors for comparing EIA signatures in GUVI limb files. 31

4.1 Parameters extracted from the EIA structure. 59

List of Figures

Figure		Page
1.1	Daytime and nighttime electron density profiles.	2
1.2	E-region dynamo.	5
1.3	Plasma drift along magnetic field lines during fountain effect.	5
1.4	Day time F-region meridional current system over the DIP equator.	6
1.5	F-region meridional winds.	8
1.6	Ionosphere formation.	10
1.7	1356 Å emission due to photoelectron impact ionization at SZA=40°.	12
1.8	GUVI limb and disk scans.	14
1.9	Arrangement of limb scans in GUVI orbit.	15
1.10	Availability of GUVI limb files in year 2005 for different local times at tangent point ascending node equator.	17
2.1	1356 Å band image and features created from a GUVI limb file by averaging 14 along track pixels.	21
2.2	1356 Å band image created from a GUVI limb file similar to fig. 2.1 but the ascending node of the orbit is on the day side.	22
2.3	(top) Source GUVI 1356 Å radiance and (bottom) GUVI 1356 Å radiance with stars removed using LBH1 spectral band radiance data.	25
2.4	(top) Source GUVI 1356 Å radiance and (bottom) GUVI 1356 Å radiance with stars removed using filtering method.	25
2.5	Day glow exponential fit (dashed line) for 1356 Å radiance profiles (solid line) at different SZA.	26
2.6	Day glow fit for SZA at different altitudes.	28

2.7 GUVI 1356 Å radiance, day glow fit and subtracted radiance at dayside LT 0900 and 1400 hours, respectively. 29

2.8 GUVI 1356 Å radiance, day glow fit and subtracted radiance at dayside LT 1430 and 1830 hours, respectively. 29

2.9 GUVI 1356 Å data and subtracted radiance at an altitude range of 230 to 520 km for successive orbits at dayside LT 1345 hours. 30

2.10 EIA variability with local time: Subtracted 1356 Å radiances 355° longitude, March equinox at 0945 hours. 32

2.11 EIA variability with local time: Subtracted 1356 Å radiances 356° longitude, December solstice at 1345 hours. 33

2.12 EIA variability with local time: Subtracted 1356 Å radiances 354° longitude, December solstice at 1730 hours. 34

2.13 EIA variability with longitude: Subtracted 1356 Å radiances at 1346 hours, December solstice at 46° longitude. 36

2.14 EIA variability with longitude: Subtracted 1356 Å radiances at 1341 hours, December solstice at 356° longitude. 37

2.15 EIA variability with season: Subtracted 1356 Å radiances 1630 hours LT, 302° longitude, equinox. 38

2.16 EIA variability with season: Subtracted 1356 Å radiances 1630 hours LT, 303° longitude, June solstice. 39

2.17 EIA variability with geomagnetic activity: Subtracted 1356 Å radiances 1524 hours LT, 153° longitude, geomagnetic quiet. 40

2.18 EIA variability with geomagnetic activity: Subtracted 1356 Å radiances 1513 hours LT, 147° longitude, geomagnetic disturbed. 41

3.1 Projected solid angle and projected area. 44

3.2 Radiance values are computed by summing electron density values along GUVI limb FOV. 45

3.3 Line of sight range for pixels at different altitudes for a spherical Earth. . . 47

3.4 Algorithm for constructing 1356 Å radiance profiles using electron densities from ionospheric models. 48

3.5 Radiance profiles from GUVI and models GAIM, TIMEGCM for March equinox. The longitude and local time at the descending node equator is 215° (Western-American sector) and 1530 hours, respectively. 49

3.6 Radiance-altitude profiles from GUVI (top) and GAIM (bottom) for March equinox. The longitude and local time at the descending node equator is 215° (Western-American sector) and 1530 hours, respectively. 50

3.7 Radiance profiles from GUVI and GAIM for March equinox. The longitude and local time at the descending node equator is 200° (Pacific sector) and 1600 hours, respectively. 51

3.8 Radiance profiles from GUVI and GAIM for March equinox. The longitude and local time at the descending node equator is 8° (African-Indian) and 1550 hours, respectively. 52

3.9 Radiance profiles from GUVI and GAIM for March equinox. The longitude and local time at the descending node equator is 320° (Brazilian sector) and 1550 hours, respectively. 52

3.10 Development of EIA with local time in GAIM at the African-Indian sector (geographic longitude 0° to 150°) during March equinox, 2003. 54

3.11 Development of EIA with local time in GAIM at the Pacific sector (geographic longitude 150° to 210°) during March equinox, 2003. 55

3.12 Development of EIA with local time in GAIM at the Western-American sector (geographic longitude 210° to 300°) during March equinox, 2003. 56

3.13 Development of EIA with local time in GAIM at the Brazilian sector (geographic longitudes 300° to 360°) during March equinox, 2003. 57

4.1 Metrics drawn from a typical structure for (left) a well formed EIA (right) a single-peaked EIA. 60

4.2 Magnetic latitude and radiance for crests and troughs of symmetric EIA structures, year 2004. 62

4.3 Magnetic latitude and radiance for crests of asymmetric EIA structures and the percentage of occurrence of symmetric and asymmetric EIA structures, year 2004. 63

4.4 Magnetic latitude and radiance for the EIA crests and troughs in the African-Indian sector, 2004 ($\leq 150°$). 64

4.5 Magnetic latitude and radiance for the EIA crests and troughs in the Pacific sector, 2004 ($> 150°$ and $\leq 210°$). 65

4.6 Magnetic latitude and radiance for the EIA crests and troughs in the Western-American sector, 2004 ($> 210°$ and $\leq 300°$). 66

4.7 Magnetic latitude and radiance for the EIA crests and troughs in the Brazilian sector, 2004 ($> 300°$ and $\leq 360°$). 66

4.8 Magnetic latitude and radiance for the EIA crests and troughs during the spring and vernal equinoxes, 2004. 67

4.9 Magnetic latitude and radiance for the EIA crests and troughs during June solstice, 2004. 68

4.10 Magnetic latitude and radiance for the EIA crests and troughs during December solstice, 2004. 68

4.11 Magnetic latitude and radiance for the EIA crests and troughs for year 2003. 69

4.12 Magnetic latitude and radiance for the EIA crests and troughs for year 2004. 70

4.13 Magnetic latitude and radiance for the EIA crests and troughs for year 2005. 70

5.1 Overlap in successive limb scans at tangent point altitude of 152 km. 72

5.2 Overlapping pixels at corresponding across track angles in successive limb scans are averaged. 73

5.3 Rebinned 1356 Å radiance (left) and along track averaged 1356 Å radiance (right) for a GUVI limb file. 74

5.4 Subtraction of dayglow emissions from 1356 Å radiance data using neutral density profiles. 75

5.5 Longitudinal variation in 1356 Å radiance from GUVI limb scans integrated over an altitude range 350 to 500 km at 15:00 hours LT, equinox 2003. . . . 76

A.1 Magnetic latitude and radiance for the EIA crests and troughs in the African-Indian sector, 2003 ($\leq 150°$). 81

A.2 Magnetic latitude and radiance for the EIA crests and troughs in the Pacific sector, 2003 ($> 150°$ and $\leq 210°$). 82

A.3 Magnetic latitude and radiance for the EIA crests and troughs in the Western-American sector, 2003 ($> 210°$ and $\leq 300°$). 82

A.4 Magnetic latitude and radiance for the EIA crests and troughs in the Brazilian sector, 2003 ($> 300°$ and $\leq 360°$). 83

A.5 Magnetic latitude and radiance for the EIA crests and troughs during the spring and vernal equinoxes, 2003. 83

A.6 Magnetic latitude and radiance for the EIA crests and troughs during June solstice, 2003. 84

A.7 Magnetic latitude and radiance for the EIA crests and troughs during December solstice, 2003. 84

A.8 Magnetic latitude and radiance for the EIA crests and troughs in the African-Indian sector, 2005 ($\leq 150^\circ$). 85

A.9 Magnetic latitude and radiance for the EIA crests and troughs in the Pacific sector, 2005 ($> 150^\circ$ and $\leq 210^\circ$). 85

A.10 Magnetic latitude and radiance for the EIA crests and troughs in the Western-American sector, 2005 ($> 210^\circ$ and $\leq 300^\circ$). 86

A.11 Magnetic latitude and radiance for the EIA crests and troughs in the Brazilian sector, 2005 ($> 300^\circ$ and $\leq 360^\circ$). 86

A.12 Magnetic latitude and radiance for the EIA crests and troughs during the spring and vernal equinoxes, 2005. 87

A.13 Magnetic latitude and radiance for the EIA crests and troughs during June solstice, 2005. 87

A.14 Magnetic latitude and radiance for the EIA crests and troughs during December solstice, 2005. 88

B.1 Sample frame from GUVI limb data movie for year 2004. 89

Acronyms

EIA	Equatorial Ionization Anomaly
GUVI	Global Ultra Violet Imager
TIMED	Thermosphere Ionosphere Mesosphere Energetics and Dynamics
DST	Disturbance Storm Time
SZA	Solar Zenith Angle
FUV	Far Ultra-Violet
USUGAIM	Utah State University Global Assimilation of Ionospheric Measurements
TIMEGCM	Thermosphere Ionosphere Mesosphere Electrodynamics General Circulation Model
FOV	Field Of View
LT	Local Time
UT	Universal Time

Chapter 1

Introduction

The Earth's ionosphere is a component of the upper atmosphere and consists of plasma. Plasma is produced by photoionization of the thin upper atmospheric gases by ultra-violet and shorter wavelength photons from the sun. Electron and ion pairs are produced in this process that mix with the gas of neutral atoms creating a plasma. An understanding of the upper atmosphere must include an understanding of the distribution and dynamics of this ionospheric plasma both of which are dependent upon a complex coupling between the neutral atmospheric winds, solar heating, photo ionization, electrical conductivity, all interacting with the magnetic field of the Earth.

The Equatorial Ionization Anomaly (EIA) is an important phenomenon occurring at low latitudes that results in the highest plasma densities in the ionosphere. Plasma is moved from the region of the magnetic equator to either sides in a range of latitudes of $\pm$ 10° to 20° north and south of the magnetic equator. The general process by which this occurs is known [1] but the understanding of its global behavior is lacking. This is because a detailed observation of this phenomenon over the large scales on which it occurs is difficult. In 2002 NASA launched the Global Ultra Violet Imager (GUVI) which can observe the EIA at various times, longitudes, and seasons by the glow of the recombining electrons and ions in the plasma. This thesis is a report on the GUVI observations of the EIA and its global behavior.

1.1 The Equatorial Ionization Anomaly (EIA)

The ionosphere is generally horizontally stratified into layers with various ion composition and structure as shown in fig. 1.1 [1]. These ionospheric layers have been given the designations of D-, E-, F1-, and F2-regions from the earliest ground-based probing using

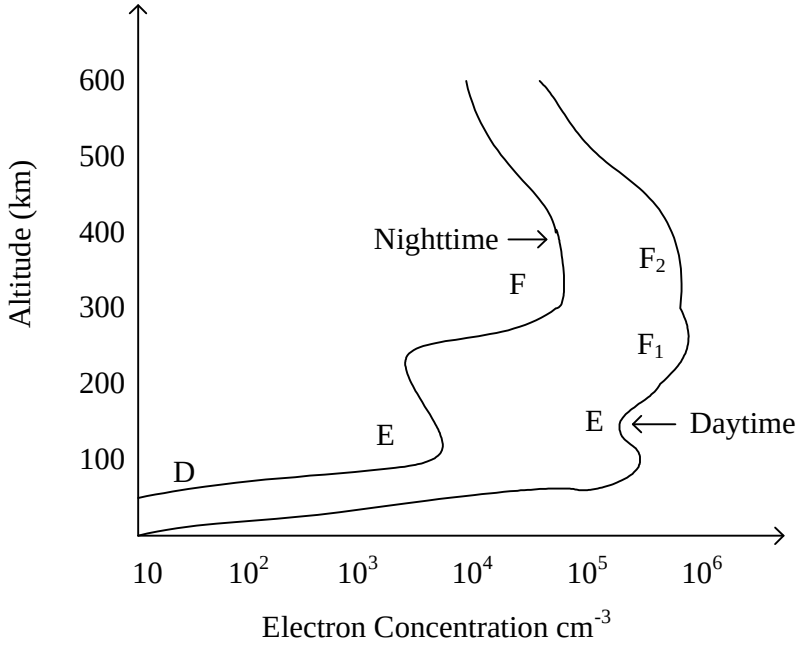

Fig. 1.1: Daytime and nighttime electron density profiles.

radio wave reflections. The production of ionospheric plasma is dependent upon both the intensity of incident solar photon and the density of the thin neutral atmosphere. The peak production of plasma occurs in the F-region between 400 to 600 km. At altitudes above the peak, the ionosphere decays monotonically with increasing altitude through a diffusive process. Below this peak the structure largely depends on the balance between plasma production and loss through recombination of ions and electrons. Therefore, the lower portion of the ionosphere varies greatly from day to night when the D- and E-regions of the ionosphere essentially disappear when production stops at sunset.

The behavior of plasma can be understood in limited conditions by considering single charged particles and the forces on them [2]. Consider the motion of a charged particle with velocity $\vec{v}$ in the presence of external magnetic $\vec{B}$ and electric fields $\vec{E}$. The force acting on this particle is the sum of electric Coulomb and magnetic Lorentz forces with the resulting motion determined by

$$m\frac{d\vec{V}}{dt} = q\vec{E} + q(\vec{v} \times \vec{B}), \tag{1.1}$$

where q and m are the charge and mass of the particle. If one is only concerned with the

steady state motion of these particles then the time derivative of the velocity is small and the resulting relation between velocity and electric and magnetic fields is found to be

$$\vec{E} = -(\vec{v} \times \vec{B}). \tag{1.2}$$

Whenever there is a continuous motion of ionospheric plasma in the presence of the Earth's magnetic field, there must exist an electric field perpendicular to both $\vec{v}$ and $\vec{B}$. Solving for $\vec{v}$ in eq. (1.2) gives the expression,

$$\vec{v} = \frac{\vec{E} \times \vec{B}}{\left|\vec{B}\right|^2}, \tag{1.3}$$

for the steady state drift of plasma in the presence of electric and magnetic fields. This $\vec{E} \times \vec{B}$ drifting is independent of charge and both ions and electrons move in the same direction resulting in no net current. Equation (1.3) can be used to gain an understanding the EIA. When first discovered, the dense bands of plasma near the equator were an anomaly based on the notion that the distribution of plasma in the ionosphere would be determined only by photoionization and recombination rates. The equatorial fountain effect, the transport process that moves plasma into the EIA, was not understood at that time. This fountain driven by an eastward electric field that exists at low latitude cause a steady state $\vec{E} \times \vec{B}$ drift of the plasma upward.

The presence of currents in the ionosphere is interdependent with the local conductivity, which varies with altitude, and the electric fields. A more detailed understanding of the EIA formation requires an understanding of the E- and F-region conductivities and how currents are driven by neutral winds. The conductivity of a charged particle in the presence of a magnetic field is given by Ohm's law [2]

$$\vec{j} = \begin{bmatrix} \sigma_P & \sigma_H & 0 \\ \sigma_H & \sigma_P & 0 \\ 0 & 0 & \sigma_{\parallel} \end{bmatrix} \cdot \vec{E}. \tag{1.4}$$

This conductivity tensor σ is given by three components, the Pederson conductivity,

σ_P, which gives currents parallel to $\vec{E}$, the Hall conductivity, σ_H, which gives currents transverse to the applied electric field direction and the Parallel conductivity $\sigma_\parallel$ which gives currents for electric fields aligned with the magnetic field. The complete dependence of these conductivities upon plasma density, electron-neutral collision frequency, ion-neutral collision frequency and magnetic field strength is given in detail by Wolfgang [2]. The conductivity parallel to the magnetic field is the largest of the three leading to the conceptual idea of the magnetic field acting as equal potential lines or conductive "wires" running through the ionosphere.

The ionospheric conductivities perpendicular to the magnetic field scale with the collision frequency between the plasma and the neutral atmosphere. At E-region altitudes, where the neutral density and hence collision frequencies are high, the Pederson conductivity, σ_P, dominates while in the F-region the Hall conductivity, σ_H, dominates. The regional motions of the neutral atmosphere, winds or tides, in either the E- or F-regions can directly drive currents in the ionosphere by dragging plasma across the magnetic field. Currents are generated because of the different behavior of electrons and ions under the driving force of a neutral wind. The conductivities of the ionosphere then generate internally consistent electric fields for this motion. These fields can then map out of the local region where they are generated along the highly conductive magnetic fields thus coupling ionospheric regions.

1.1.1 E-region Dynamo

The Earth's magnetic field lines run from the geographic south pole to the geographic north pole and are parallel to the Earth's surface at the magnetic equator. They have an upward component in the southern hemisphere and downward component in the northern hemisphere.

Winds in the neutral atmosphere are generated during the day by the Sun's heating and tend to blow away from the sub solar point in the upper atmosphere. These winds drag the local plasma with them. In the daytime E-region the meridional or north/south winds can interact with the vertical component of the magnetic field to produce electric fields in the east or west direction. If one considers the magnetic field geometry at the equator as shown

in fig. 1.2 [3] and meridional winds all blowing away from the equator then the southern E-region will generate an eastward electric field consistent with eq. (1.2). The winds dragging plasma northward in the northern E-region also generate an eastward electric field. The high conductivity along the field lines allows the eastward electric fields generated in the E-region to co-add and map along the magnetic field up to F-region altitudes. In the F-region, above the magnetic equator, these eastward electric fields and the horizontal magnetic fields drive an upward $\vec{E} \times \vec{B}$ drift of plasma as per eq. (1.3) and as shown in fig. 1.2 [3].

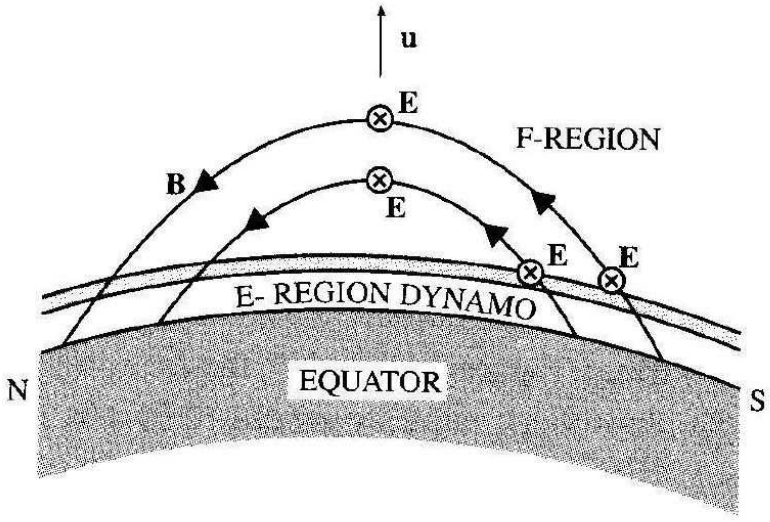

Fig. 1.2: E-region dynamo.

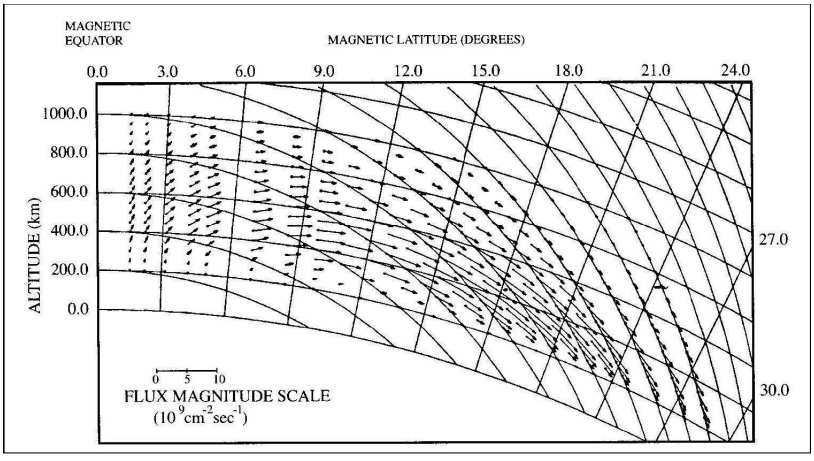

Fig. 1.3: Plasma drift along magnetic field lines during fountain effect.

This same process occurs for plasma just off the magnetic equator but because of the north and south tilting of the magnetic field the upward drift also has an $\vec{E} \times \vec{B}$ drift component away from the equatorial region towards the poles. A second mechanism which also moves plasma poleward from the equatorial region is diffusion aided by gravity. The plasma which has been lifted to higher altitudes, diffuses along the magnetic field falling back and sliding poleward to higher latitudes along the flux tube geometry of the magnetic field. A third mechanism that contributes or retards plasma moving away from the equatorial region along the magnetic fields is the dragging of the plasma by north-south winds at F-region altitudes. All together these processes lead to the motion of plasma away from the equator, as shown in fig. 1.3 [1], and result in the EIA. This entire process is called the fountain effect and is caused by the electric fields generated at the E-region i.e. the E-region dynamo.

1.1.2 F-region Dynamo

The E-region dynamo is controlled by the E-region plasma density and neutral winds. The electric fields generated in this way dominate in the day but subside at night. After sunset the ions in E-region quickly recombine and the E-region dynamo process stops.

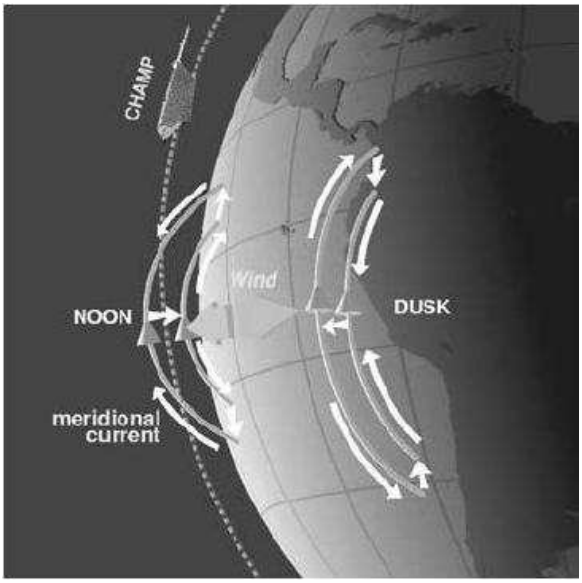

Fig. 1.4: Day time F-region meridional current system over the DIP equator.

At this point the F-region dynamo, where recombination happens much slower, becomes important. Zonal neutral winds or east/west winds in the F-region create a meridional current system and in the process generate a vertical polarization electric field (fig. 1.4 [4]). During the day this polarization field is weak as the E-regions are highly conductive across the field lines and this meridional current loop can close in the E-region. However during the night, the E-region conductivity drops, and the vertical electric field grows in the F-region which creates an $\vec{E} \times \vec{B}$ plasma drift. Therefore F-layer dynamo plays a dominant role in the night time EIA development. A more detailed explanation on the F-region dynamo is given by Rishbeth [5].

1.2 Factors Affecting the EIA

The EIA development depends on a complex coupling of a number of atmospheric processes but foremost it is dependent on winds in the upper atmosphere. Two different processes, the E- and F-region dynamos control the EIA formation during the day and its evolution during the night. The EIA shows considerable variability with local time, longitude and season. A description of a few factors creating variability in the EIA will be presented next.

1.2.1 Magnetic Equator

The direction of the Earth's magnetic field can be given in terms of magnetic inclination and declination. The magnetic or the DIP equator are the latitudes where the inclination or dip is zero. The magnetic equator does not follow the geographic equator. Its alignment from the geographic equator varies considerably with longitude but neutral atmospheric winds are generally aligned with the geographic equator. At longitudes where the magnetic equator lies far off from the geographic equator, an asymmetry in the equatorial arcs is expected due to variations of the neutral winds with latitude. In fig. 1.5 [6], the Sun is aligned with the magnetic equator and the neutral winds are assumed to blow symmetrically on to both sides of the DIP equator. As the Earth rotates, the magnetic dipole shifts with respect to the Sun and the sub solar point lies entirely to the north of the DIP equator even

during equinox conditions [6]. This resulting asymmetry partially explains the longitudinal variability in the structure of the equatorial arcs.

1.2.2 F-region Neutral Winds

The north and south peaks of the EIA have asymmetries during summer or winter solstice due to the nature of the resulting meridional neutral winds in the F-region. The winds blow away from the sub solar point which is generally located north or south of the EIA. During solstice, winds from the sub solar point tend to push the plasma into the winter hemisphere and the anomaly is more developed on to one side of the magnetic equator. Thus, a seasonal shift in the sub solar point accounts for some of the asymmetric seasonal variability in the EIA.

This same process is responsible for a shifting of the latitude at which the peak density in the EIA occurs. At a certain altitude the diffusion of the plasma down and along flux tubes in the equatorial fountain can be balanced against the neutral north or south winds, the plasma tends to lie suspended if the wind is against the downward drift. This piling of plasma will eventually be where we see the peaks of the EIA occur thus moving the arc closer to the geomagnetic equator.

Another complex F-region process called the pre-reversal enhancement is known to be responsible for a sudden increase in the vertical plasma drift in the F-region, and hence an

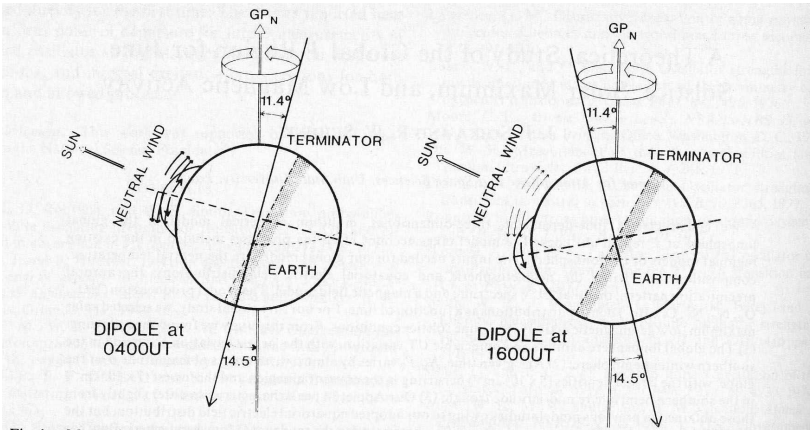

Fig. 1.5: F-region meridional winds.

impulsive enhancement in the EIA is predicted to occur in the evening local time sectors due to this sudden upward motion.

1.2.3 Solar Flux

The solar flux or F10.7 is an index of solar activity measured by the radio power from the Sun at 10.7 cm wavelength. It varies with the 11-year solar cycle and is used almost interchangeably with the sunspot index. The solar activity is directly correlated with the amount of ionizing radiation from the Sun and the amount of production of plasma in the ionosphere. It is also directly related to the amount of heating of the neutral atmosphere which controls both the density profile of the neutral atmosphere and the winds associated with the atmospheric tides. Thus the solar flux has great input on the overall density of plasma in the EIA and its formation through changing neutral winds.

1.2.4 Quiet and Disturbed Magnetic Periods

During magnetic storms there is an enhanced charged particle precipitation at the Earth's poles accompanying an increase of ionospheric currents driven, by the magnetosphere, in the auroral region. These currents result in heating of the upper atmosphere through ohmic or joule heating processes. This has a significant impact on the global neutral wind patterns, the E-region electric fields and hence the formation of the EIA. In most ionospheric studies, data from quiet and disturbed magnetic periods are considered separately. An estimate of geomagnetic activity can be obtained from planetary K (K_p) and Disturbance Storm Time (DST) indices. DST is the horizontal component of the geomagnetic field at the magnetic equator and is usually measured in nanotesla. It is inversely proportional to and indicative of the ring current intensity. During a geomagnetic storm, the DST is found to shoot up for a brief period before falling to drastically low negative values. The DST values drop more and more negative as the intensity of the magnetic storm increases. Planetary K is a 3-hour index measuring the variation in geomagnetic intensity due to solar activity. It is measured on a scale of 1 to 9. A $K_p \leq 3$ is indicative of a magnetically quiet period.

1.3 Ionospheric Processes

The ionosphere is formed when high energy solar photons ionize the atmospheric neutrals creating electron ion pairs [2]. The density of neutral atoms decrease exponentially with altitude, z, while the incoming solar radiation intensity decreases exponentially with decreasing altitude as it is absorbed by the neutrals. The production of electron-ion pairs or photo ionization rate at any altitude is determined by the neutral density and the intensity of ionizing photons. The production rate as a function of altitude is given by the well known Chapman function shown in fig. 1.6 [2]. The peak production value is found to lie in F-region, at an altitude of about 350 km. The peak production altitude and amplitude varies with Solar Zenith Angle (SZA).

1.3.1 Ionospheric Photo Emissions

Radiative recombination, where electrons and neutrals recombine, is the dominating plasma loss process at higher altitudes. The electrons recombine with positive ions to yield

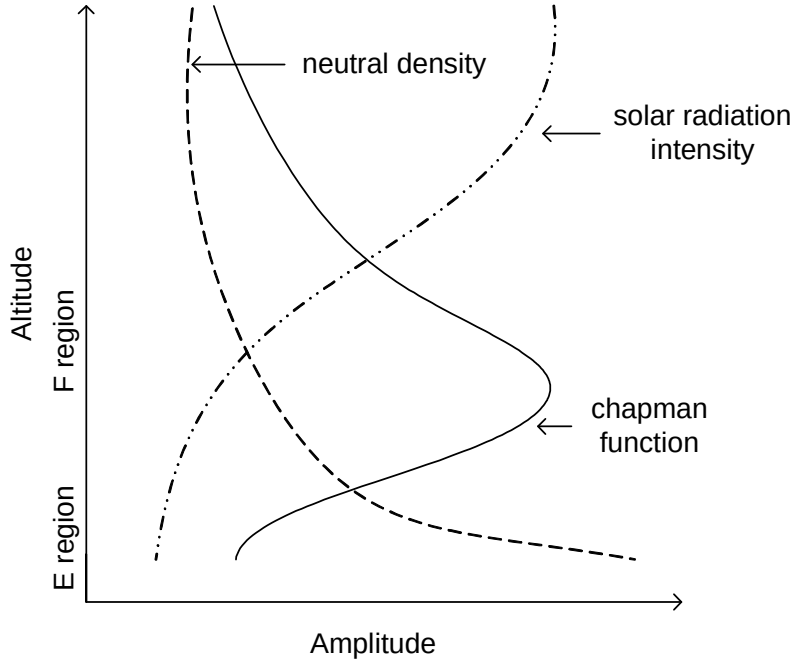

Fig. 1.6: Ionosphere formation.

neutral atoms and high energy photons. For oxygen ions the process can be written as [3]

$$O^+ + e^- = O + h\nu. \tag{1.5}$$

The photons emitted cover the range of oxygen emission lines with some percentage of the photons being emitted at a far ultra-violet wavelength of 1356 Å . The loss rate is proportional to the density of the ions and electrons available to recombine which is given by

$$\frac{d[O^+]}{dt} = k[O^+]N_e. \tag{1.6}$$

Oxygen ions are the dominant species, over 99%, in the F-region plasma and in a quasi neutral plasma, the density of electrons is equal to the density of oxygen ions or

$$[O^+] = N_e. \tag{1.7}$$

From eq. 1.6 we have

$$\frac{d[O^+]}{dt} = kN_e^2, \tag{1.8}$$

where the constant k is called the recombination rate and $k = 7.3 * 10^{-13}$ $\mathrm{cm^3 s^{-1}}$. Other competing plasma loss processes [3] do not play a significant role at F-region altitudes where we have a lower concentration of the neutrals. Any observed 1356 Å emission from these altitudes is attributed to the radiative recombination process, and hence is directly proportional to the electron density at these altitudes. By observing these emissions, as is done with GUVI on the TIMED spacecraft, information on the density of the ionosphere can be obtained.

1.3.2 Photoelectron Impact Ionization

During the day, high energy photoelectrons, just released from atoms, impact on other neutrals and excite them to produce FUV and other emissions in the process. This is a second process by which oxygen atoms emit 1356 Å photons. These emissions are related

to the density of the neutral oxygen atoms. Since neutral densities decrease exponentially with altitude, these emissions peak at around 150 km and decrease exponentially as we approach the F-region as can be seen in fig. 1.7. These emissions are related to the solar zenith angle of the observation point. The photoelectron impact is maximum at low solar zenith angles i.e. at noon time and disappears at night.

Emissions due to this process and resonant scattering of sunlight at 1356 Å [7] contaminate the relatively low intensity 1356 Å recombination emissions during the day that are of interest for studying the density of the ionosphere. At night this is not a problem. To study the EIA in the day side we need to look at the 1356 Å emissions as a function of altitude in order to separate the recombination radiation from the low altitude emissions due to photoelectron impact ionization.

1.4 Ionospheric Models

A comprehensive review of a number of ionospheric models is given by Roble [8]. We are primarily interested in two models, Utah State University Global Assimilation of Ionospheric Measurements (USUGAIM) and the NCAR Thermosphere, Ionosphere, Mesosphere,

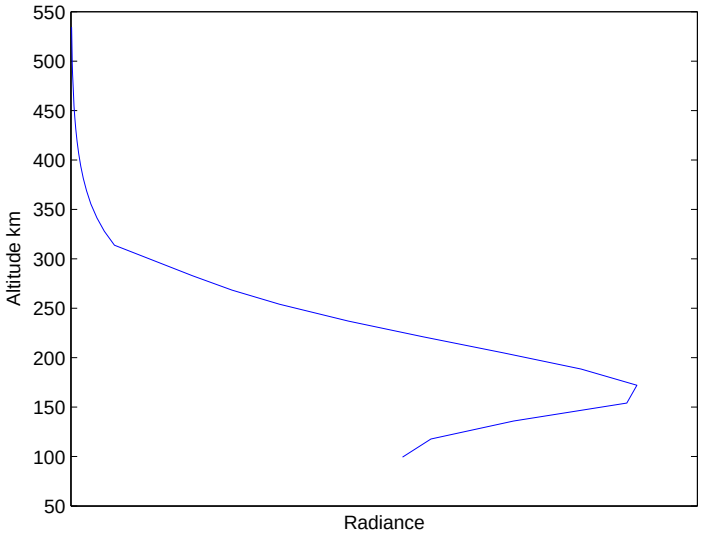

Fig. 1.7: 1356 Å emission due to photoelectron impact ionization at SZA=40°.

Electrodynamics General Circulation Model (TIMEGCM). USUGAIM will be referred to as GAIM henceforth in this thesis.

These models predict the global 3-dimensional electron density distribution for any specified UT. GAIM uses a physics based model(Ionosphere Forecast Model) and a kalman filter based recursive estimation system for assimilating a diverse set of real time measurements taken from ionosondes, satellites and GPS stations. TIMEGCM is a first principles numerical model and it incorporates coupling from a number of atmospheric processes including dynamics and electrodynamics of the lower atmospheres, auroral precipitation, ionospheric convection, tides and solar heating [8]. It also uses inputs from a number of other empirical models and data from a few ground based stations. A detailed description of the global circulation models is given by Washington and Williamson [9].

1.5 Instrument and Data

1.5.1 GUVI Instrument

The Global Ultraviolet Imager (GUVI) is a spectrograph on board NASA's TIMED spacecraft. The TIMED spacecraft flies in a nadir-pointing orientation from its 625-km, circular orbit at an inclination of 74.1°. The instrument is designed to remotely sense the region of the atmosphere up to 500 km to determine energy sources and sinks as well as the atmospheric state variables of pressure, density, temperature, and winds [10]. The spacecraft has been on orbit since year 2002. A detailed description of the GUVI instrument can be found in the GUVI home page [11].

GUVI instrument operates continually throughout each TIMED orbit and registers the radiance of FUV emissions from upper atmospheres. It consists of a scanning imaging spectrograph that collects spectral data, a detector system that converts detector information recorded at detector into wavelength and spatial information, and a data handling and control electronics system [12].

The detector is a Rowland spectrograph capable of observing FUV airglow emissions at five different wavelength channels between 115.0 and 180.0 nm. Major emission features

within those channels include H (121.6 nm), O (130.4 nm), O (135.6 nm) and the N_2 LBH bands. A mirror scans the instantaneous field-of-view of the entrance slit on the GUVI spectrograph across the Earth's limb and disk [12]. Light from this scan mirror is imaged on a slit. The slit width can be set to .24 mm, 0.39 mm or .97 mm for narrow, medium and wide configurations. The widest slit is used to increase the sensitivity of the system to minimize statistical error when low count rates are obtained especially while imaging the night FUV. The narrowest slit is used to increase the spectral resolution of the system. The instrument operates in two modes, imaging and spectrograph. During imaging mode the scan mirror sweeps through cross track angles perpendicular to the spacecraft motion while in spectrograph mode, the scan mirror is held at a fixed viewing angle.

The TIMED spacecraft has a retrograde orbit and an orbital period of 97.8 minutes. It makes about 14 to 15 orbits a day. Each orbit can be considered to begin at the ascending equator and crosses both the day and the night side equator. The TIMED spacecraft orbits precede roughly by 1 to 2 minutes in local time and are separated by 24° in longitude. It takes around 60 days for the spacecraft (i.e. 60*15 orbits) to span a period of 24 hours in local time. Hence it can be said that the TIMED makes six global time passes in a year [3].

1.5.2 GUVI Data

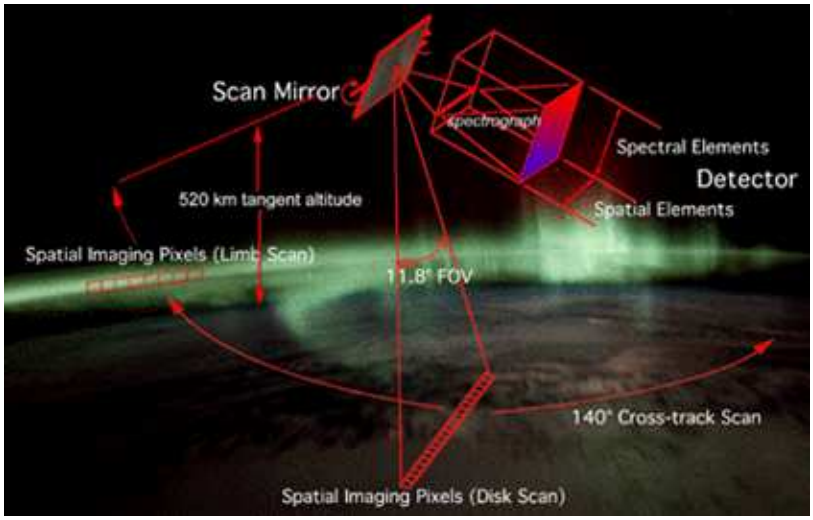

Fig. 1.8: GUVI limb and disk scans.

The geometry of the field of view of the TIMED spacecraft is given in detail by Christensen et al. [12]. The detector array contains 14 spatial pixels. They provide information along the orbit of the spacecraft and so they are known as along track pixels. In imaging mode the scan mirror of the spacecraft sweeps in 15 second scan cycles along an orientation perpendicular to the orbit of the spacecraft thus collecting data in steps of across track angles during disk and limb scans (fig. 1.8 [11]). An orbit comprises of several frames (or scans) each having a set of cross track pixels and 14 along track pixels. In the disk or the Earth viewing scan, the scan mirror steps through 159 cross track angles collecting data at an angle of 67.2° from the nadir (straight down) to −60° on the other side of the nadir.

During the limb scans, the scan mirror observes the higher altitudes of the atmosphere in a direction tangential to the Earth. Limb data is collected from 80° to 67.2° angles at the same side of the nadir. To avoid direct sunlight into the sensor field of view, limb data is always collected from the direction away from the Sun (cold side). The scans are collected over a cross track angle range of 12.8° in 32 steps. Thus each limb scan consists of 14 along track and 32 across track pixels. With a 15 second scan period and an orbital period of 97.8 minutes, the limb files have around 390 scans in an orbit.

A limb pixel is defined by the coordinates of the tangent points, i.e. the minimum

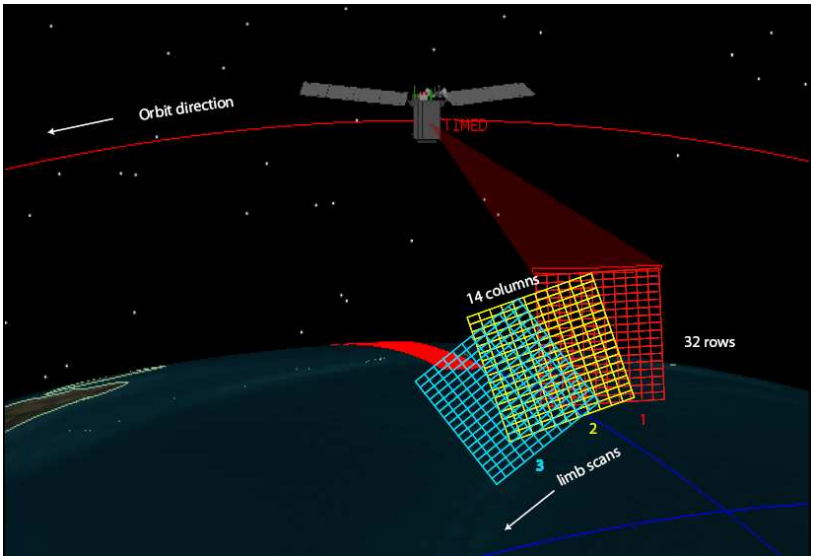

Fig. 1.9: Arrangement of limb scans in GUVI orbit.

altitude point in the field of view with reference to an ellipsoidal Earth [13]. The observed radiance along a limb field of view (FOV) is attributed to the tangent point. The 32 cross track pixels in a limb scan correspond to a tangent point altitude range of 100 to 500 km and the altitude separation between successive cross track pixels vary from 8 km at the high altitudes to 20 km at the low altitudes. In the limb, each cross track pixel has a resolution of 0.4°. The 14 along track pixels correspond to an angle of 11.8° with an along-track resolution of 0.842°/pixel. It can be easily seen that the along track pixels of successive scans overlap significantly, i.e. the same tangent point is observed in successive scans. The amount of overlap also varies with the altitude of the tangent point as can be seen in fig. 1.9. This is because the range to the tangent point increases from the high altitude pixels to the low altitude ones.

We recall that the day side airglow data is heavily contaminated with low altitude excitation emissions. With this discussion, the advantage of using the high altitude GUVI limb scans for observing the day side equatorial should be obvious. As GUVI provides six yearly time passes at all longitude sectors for years 2002 up to 2007, we have sufficient number of observations to make an extensive study of the equatorial ionosphere.

The availability of GUVI limb data files closely corresponds to orbits of the TIMED spacecraft. Each limb file has data for one orbit with observations of both day side and night side equator. While the two equator crossings of the TIMED spacecraft are separated by 12 hours in local time, the day side and night side equator observations in the limb file are separated by about 9 hours in local time. Tangent point observations at the start of successive limb files are separated by around 1 minute in local time. However when the tangent point is at noon local time, any limb emission would be heavily swamped by the overhead Sun. To avoid this and to avoid any direct sunlight from hitting the radiator, the spacecraft performs a yaw maneuver. GUVI field of view turns by 180° to the cold (anti-sunward) side. During these times the local time of the tangent point jumps by 2 hours on both day and night side. Due to this yaw maneuver, GUVI limb files do not have any observations of the noon time EIA. This works to our disadvantage because EIA

observations of the sub-solar point is key in understanding the variability of the equatorial ionosphere with solar heating. Also, due to the yaw maneuver, GUVI data has extra samples of tangent point equators with local times 2400 and 0100. Figure 1.10 shows the distribution of limb files with local time of the tangent point equator. As every local time hour period is sampled once every 60 days, we can easily see that the yaw maneuver also occurs once every 60 days.

1.6 Thesis Objective

This thesis presents a study of the day side equatorial anomaly using 1356 Å emissions in the GUVI limb imaging files. Sid Henderson [3] has done an extensive study on the morphology of the EIA and equatorial plasma bubbles on the night side GUVI disk data. A comparative study of the day side EIA gives us key understanding of the growth of EIA with local time during the day when most of the solar forcing occurs. This thesis presents how GUVI data can be used to understand the morphology of the EIA and its dependence on seasons, longitude and solar flux periods.

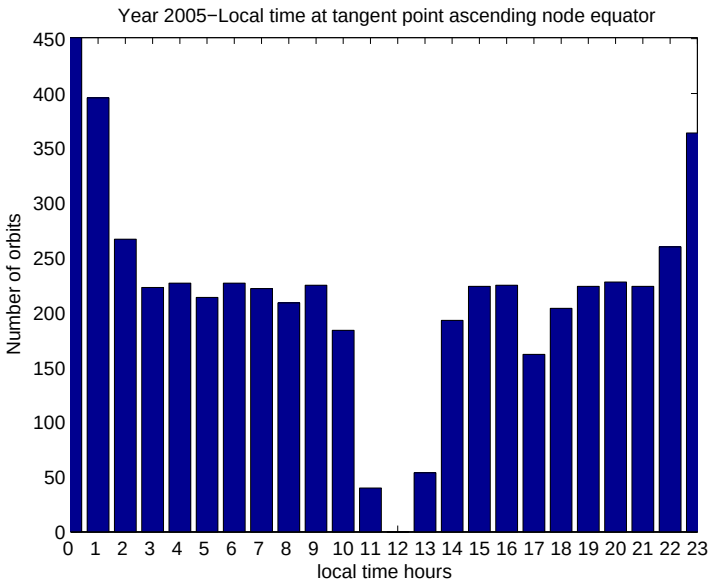

Fig. 1.10: Availability of GUVI limb files in year 2005 for different local times at tangent point ascending node equator.

Chapter 2 outlines the features in a limb data image and the data processing done on it to remove features due to other emission sources. A process to remove the bright emissions at low altitudes due to photoelectron impact excitation is described in this chapter. This process is repeated for many quiet time GUVI data and the variability in the EIA structure at different local times, seasons and longitude is shown.

A comparison of these day side GUVI EIA observations with ionospheric electron density compositions predicted by ionospheric models such as GAIM and TIMEGCM is done. As discussed in sec. 1.4, the models incorporate atmospheric forcing that have been understood to affect the ionospheric composition. Since there is a direct relation between electron density and 1356 Å recombination emissions, the electron density composition predicted from the models can be converted to 1356 Å limb emissions as would be seen by the GUVI limb field of view at every tangent point. A comparison of the two gives us preliminary insights into how closely these models predict the observed day side equatorial ionospheric conditions. Chapter 3 presents in some detail the radiometric calculations and the algorithm used to convert electron densities from the atmospheric models into 1356 Å emissions comparable to GUVI data. Some key results of the comparison and the development of the EIA as predicted by GAIM is discussed.

It is difficult to draw conclusive inferences from individual limb files as there is a lot of day to day variability in the EIA morphology. However, we can study just the important parameters from the EIA structure such as peak radiance and peak latitude [3]. These can be then characterized as a function of local time for various seasons and longitudes. This comparative study with day side data can lead to interesting observations of the trends in the EIA morphology. Chapter 4 discusses this process in some detail.

Chapter 5 discusses avenues for future work in this study. We have currently taken care of the spatial overlap in the 14 along track pixels by averaging radiance data across the along track pixels. However, some improvement in resolution and accuracy can be achieved if we regrid and bin the limb files such that there is a one to one correspondence between a pixel and its tangent point coordinate. A simple attempt to solve this regridding problem is

discussed here. GUVI limb data can also be used to study the effect of atmospheric tides on the EIA. Observations of the F-region ionospheric densities [14] have shown the existence of a longitudinal wave number 4 pattern due to atmospheric tides. This effect has also been observed in a few GUVI data samples. Preliminary data processing that has been done in this thesis can be used to study the longitudinal wave number 4 pattern in GUVI data.

Chapter 2

Processing GUVI Limb Files

The limb scans from the GUVI instrument contain a rich set of information on the state of the upper atmosphere. It was expected that GUVI would provide information about the ionosphere on the night side by observing the faint glow due to electron oxygen ion recombination. It was also expected that this signature would be masked on the day side due to the much brighter air glow signature of the neutral atmosphere being excited directly by the Sun. Initial review of the GUVI limb data revealed that signatures of the 1356 Å airglow due to recombination could be identified at the top of the scans but that at lower altitudes the ionosphere signal was indeed corrupted by the glow from the day time neutral atmosphere. These emissions will be referred to as dayglow emissions henceforth in this thesis. This chapter contains a description of the algorithms developed to study the day side EIA. A simple comparison of the EIA formation at different local times, longitudes and seasons is presented.

2.1 GUVI Limb File

A GUVI limb file consists of all the limb scans for one complete orbit of the TIMED spacecraft starting at the ascending node of the orbit through to the next ascending node i.e. when the spacecraft crosses the equator moving from the south to the north. A limb file comprises approximately 390 complete limb scans over the approximate 90 minute orbit. As described in Chapter 1, each scan consists of 14 along track and 32 cross track pixels. The 32 cross track pixels are from a tangent point altitude spaced over the range of 100-500 km and each pixel in the limb file is geolocated by the latitude and longitude of the tangent point. These scans are stacked horizontally to give a 1356 Å radiance image of the entire orbit as a function of altitude (fig. 2.1). Images created in this manner have two equator

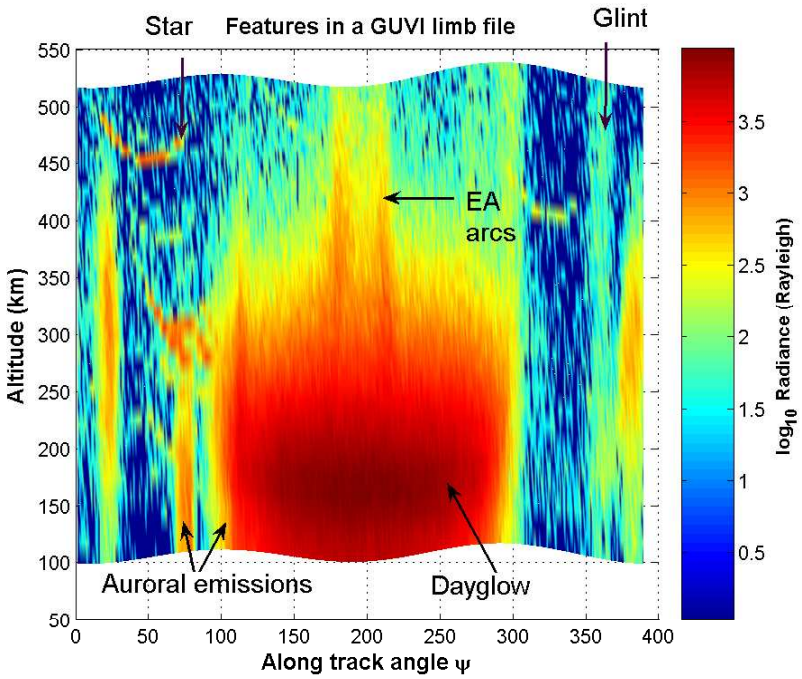

Fig. 2.1: 1356 Å band image and features created from a GUVI limb file by averaging 14 along track pixels.

crossings - the equator at the start of the orbit or the ascending node equator and the mid-orbit or descending node equator crossing. The nodes are separated by approximately nine hours in local time and the two equator crossings switch between day and night time as the TIMED spacecraft orbit drifts with local time. To improve signal statistics, the radiances of the 14 instantaneous along track pixels for every scan have been averaged together for the data in fig. 2.1.

2.2 Features in a Limb File

The typical features found in the 1356 Å radiance source image are labeled in fig. 2.1. The image magnitude is given in the log of radiance in rayleigh. The local time (LT) varies widely with along track angle ψ, the angle of the spacecraft in its orbit as measured from the ascending node, beginning and ending at the night side equator. The local times of interest for this study are on the day side equator. For the orbit given in fig. 2.1, the day side equator occurs at 1337 hours LT.

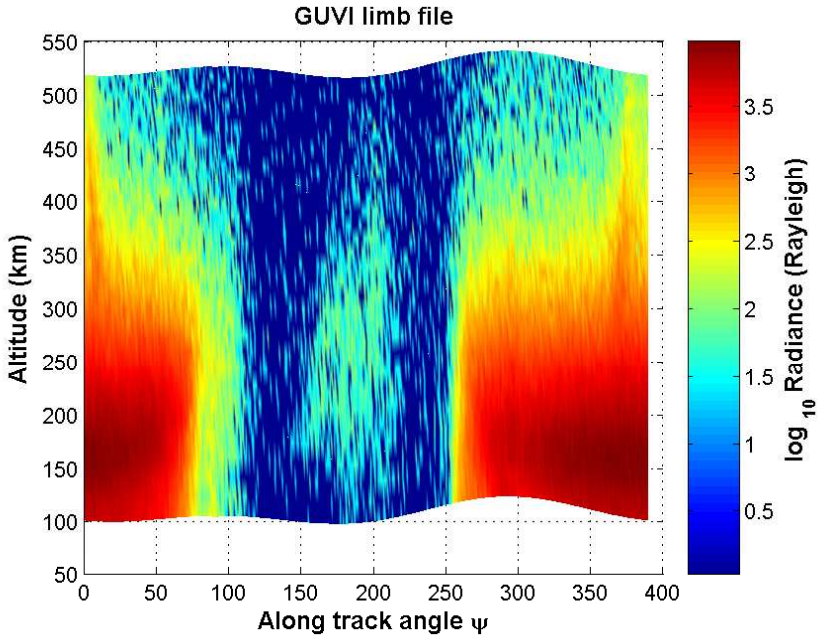

Fig. 2.2: 1356 Å band image created from a GUVI limb file similar to fig. 2.1 but the ascending node of the orbit is on the day side.

The equatorial arcs at an altitude of 350-500 km around the day side equator are clearly seen in the source image. The signatures of the night time EIA are also seen at the start and end of the orbit. These signals are observed at far lower altitudes than the day time EIA because there is no dayglow contamination. The day glow signals or the bright emissions at lower altitudes from 100-250 km are due to photoelectron impact ionization of neutral densities as described in Chapter 1. It is a function of local time and occurs only when the Sun is directly illuminating the atmosphere. Relatively bright emissions at lower altitudes up to 250 km can be observed due to auroral FUV emissions. These occur at high latitudes ($> 60^\circ$ or $< -60^\circ$) both at the day and night side. On the day side, the auroral signatures reach up to higher altitudes. The intensities of these auroral emissions increase significantly with geomagnetic disturbance. During a stormy period, highly intense auroral emissions may occur even at mid-latitudes. Both auroral emissions and emissions due to photoelectron impact have an approximate exponential distribution with altitude as they are strongly dependent on the structure of the neutral atmosphere.

The other sources of emissions marked in fig. 2.1 are the stars and glints. Stars are

point sources of FUV emission and are seen as localized high intensity pixels positioned at any altitude or along track angle. The occurrence and position of these stars vary from day to day depending on the GUVI orbit. These form simple curves when displayed as images such as fig. 2.1. Glints are emissions from the sun or other sources that get reflected off objects or surfaces near the GUVI sensor. Glints due to stray sunlight occur most often in dawn to dusk orbits when the TIMED orbit is at a maximum β angle. β angle is defined as the angle between the orbital plane and the line of sight between the Sun and the spacecraft. These glints occur periodically and their positions in the source image moves as the orbital plane drifts from day to day. At a given along track position, they occur with a constant intensity at all tangent point altitudes. Figure 2.2 shows a sample GUVI limb file similar to fig. 2.1 but here the dayside is at the ascending node. The two equatorial arcs can be seen either sides of the magnetic equator at the start and end of the orbit. Faint night time EIA signatures can be observed at the descending node equator at the center of the image. The local time at the dayside equator at the start of the orbit is 1400 hours and is 2300 hours at the mid-orbit equator.

2.3 Data Reduction

There are three objectives in preparing GUVI limb data for analysis. The first is the removal of glints in the data as far as is possible. The second is the removal of stars from the limb data and third is the removal of the dayglow signatures from the images. These objectives have largely been met at least to the point that the behavior of the EIA can be clearly observed on both the day and night side. The algorithms can be developed to automatically classify the EIA behavior over the entire five-year data set without fear of the contaminating signatures dominating the results. Many of these algorithms were developed by my fellow student, Steven Burr, whom I would like to acknowledge at this point.

2.3.1 Emissions Due to Stars and Glints

The N_2 Lyman-Birge-Hopfield 1400-1500 Å (LBH1 short) spectral emissions observed by GUVI can be used to remove spurious signals due to glints and stars. LBH1 emissions

are primarily due to photoelectron impact ionization of neutral N_2 molecules. The LBH1 spectra has no emissions in F-region altitudes. Any high altitude emission found in the LBH1 spectral band must therefore correspond to spurious intensities from stars and glints. The magnitude of these emissions differ between the LBH1 and 1356 Å spectral regions. The ratio between the intensities in the two spectra was determined by comparing signatures of stars in GUVI 1356 Å and LBH1 radiances and was found to be 0.55. High altitude LBH1 intensities can then be scaled by this ratio and subtracted off the 1356 Å radiances to eliminate the signatures of stars/glints that may interfere with EIA signatures. This technique however fails to detect and remove stars at altitudes below 300 km due to the presence of dayglow as shown in fig. 2.3.

Glints and stars can also be removed by block spatial filtering methods. A top-hat filter mask is applied to the image to locate high intensity localized pixels that correspond to stars/glints. The detected stars are subtracted off the original image and replaced by the local mean. This method is effective in removing stars from the low altitude high intensity dayglow regions in the image as shown in fig. 2.4. The downside of this technique is that the filtering operation tends to smoothen the edges of the high intensity dayglow regions.

2.3.2 Emissions Due to Photoelectron Impact Ionization

Dayglow emissions vary with altitude, Solar Zenith Angle (SZA) and seasons. To extract the recombination signals from a background of these dayglow emissions, a reasonable fit for the dayglow function is determined and subtracted from the radiance image. Dayglow emissions are caused by the impact of solar radiation on neutral densities. As described in Chapter 1, due to the nature of the underlying processes that cause the dayglow, these emissions can be approximately modeled as an exponentially decaying function with altitude and a cosine function with SZA. The dayglow emission peaks in altitude between 100-200 km and decays exponentially thereon as shown in fig. 2.5. The peak dayglow emission in a limb file occurs at an along track angle corresponding to the minimum SZA in the orbit. This translates to the dependence of the dayglow on local time. The altitude of peak dayglow emissions vary with along track angle such that the peak altitude increases with

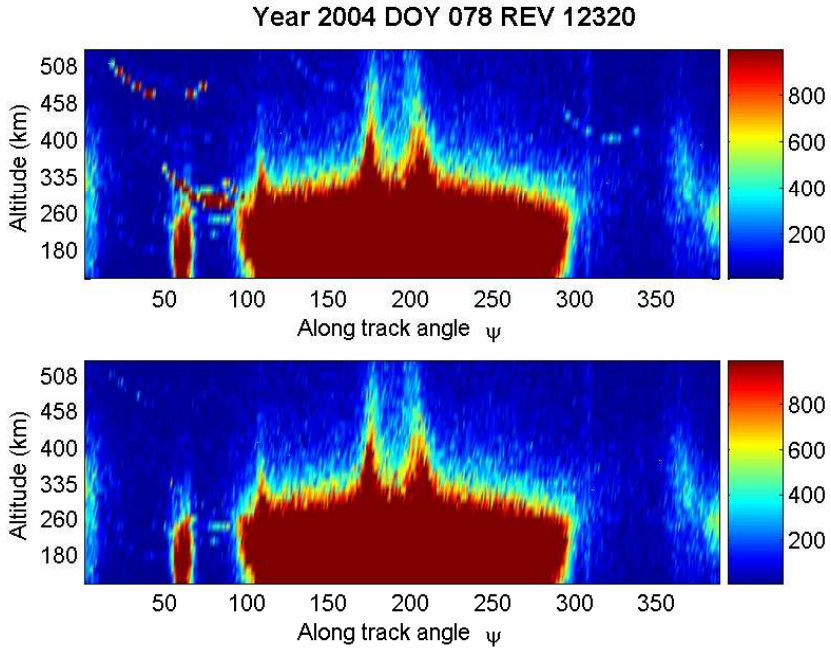

Fig. 2.3: (top) Source GUVI 1356 Å radiance and (bottom) GUVI 1356 Å radiance with stars removed using LBH1 spectral band radiance data.

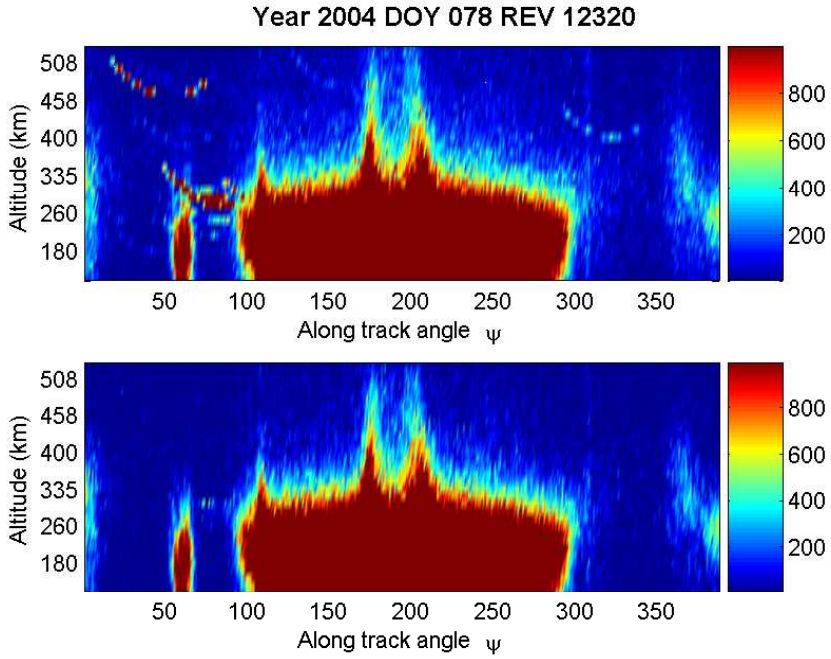

Fig. 2.4: (top) Source GUVI 1356 Å radiance and (bottom) GUVI 1356 Å radiance with stars removed using filtering method.

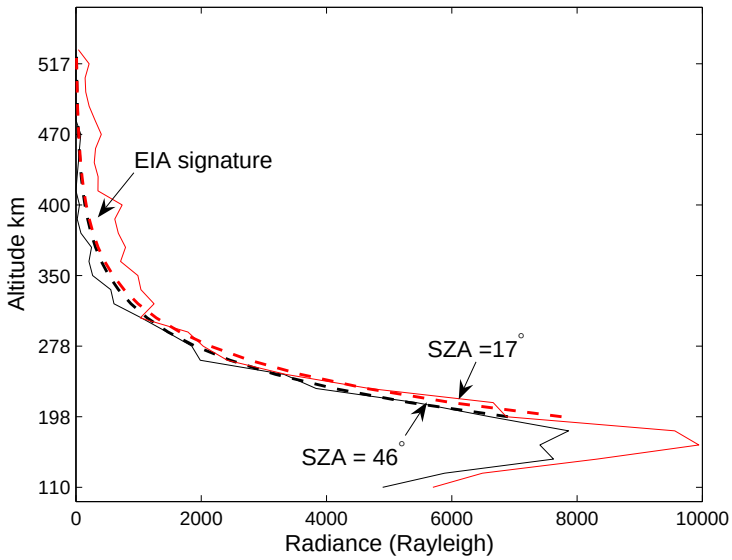

Fig. 2.5: Day glow exponential fit (dashed line) for 1356 Å radiance profiles (solid line) at different SZA.

SZA. The exponential decay of I beyond the peak density (I_0) altitude can be written as

$$I = I_0 e^{-\frac{x}{H}}, \tag{2.1}$$

$$\log I = \log I_0 - \frac{x}{H}, \tag{2.2}$$

$$I = e^{(\log I_0 - \frac{x}{H})}, \tag{2.3}$$

where H is the top side scale height for the dayglow emissions and x is the altitude. From the straight line equation (eq. 5.3), both the intercept $b = \log I_0$ and the slope $m = -\frac{1}{H}$ can be written as a cosine function of SZA using parameters that regulate the magnitude offset α and magnitude scale value β, period of the cosine function γ and phase shift δ. γ regulates the shape of the dayglow region and the phase shift δ represents the shift of the subsolar point with seasons.

$$m = \alpha + \beta \cos(\gamma \theta_{SZA} + \delta). \tag{2.4}$$

The combined dependence of the dayglow surface on x and θ_{SZA} is written as

$$I = e^{(\alpha_1 + \beta_1 \cos(\gamma_1 \theta_{SZA} + \delta)) + x(\alpha_2 + \beta_2 \cos(\gamma_2 \theta_{SZA} + \delta))}. \tag{2.5}$$

These coefficients α_1, α_2, β_1, β_2, γ_1, γ_2 and δ can vary considerably from day to day with local time, season and longitude. A solution for eq. 2.5 can be obtained by fitting GUVI 1356 Å radiance data to the day glow approximation model in a least square sense. Data for fitting the dayglow surface is obtained from GUVI limb file radiance values for a subset of cross track pixels corresponding to an altitude range of 200 to 410 km as shown in fig. 2.5. This range of altitude is selected because the dayglow profile is not an exponential (fig. 2.5) below the peak altitude which lies at about 200 km. At altitudes higher than 400 km, the source surface primarily contains recombination EIA signatures. As there are no photoelectron impact emissions in the night time, the surface is not fit for any night side data. Hence, a selected data window with SZA < 100 is used to find the parameters for the day glow model. Least squares fitting solves for the parameters discussed above while minimizing the square of the error between the data and the surface thus modeled. The resulting dayglow surface modeled using the parameters can be subtracted from source image to leave behind traces of high altitude emissions corresponding to the EIA region. The auroral emissions also have a decaying exponential altitude profile. So this surface fitting subtraction method also eliminates some of the auroral emissions found in 1356 Å radiance data.

This method was found to work reasonably well for all local times and seasons. Figure 2.6 shows the along track radiance fits at different altitudes. It can be observed that at higher altitudes, the dayglow fit excludes most of the recombination radiances due to EIA. Some EIA signals do get introduced in the dayglow fit and result in excess subtraction of the recombination emissions. This can be avoided by employing an iterative scheme such

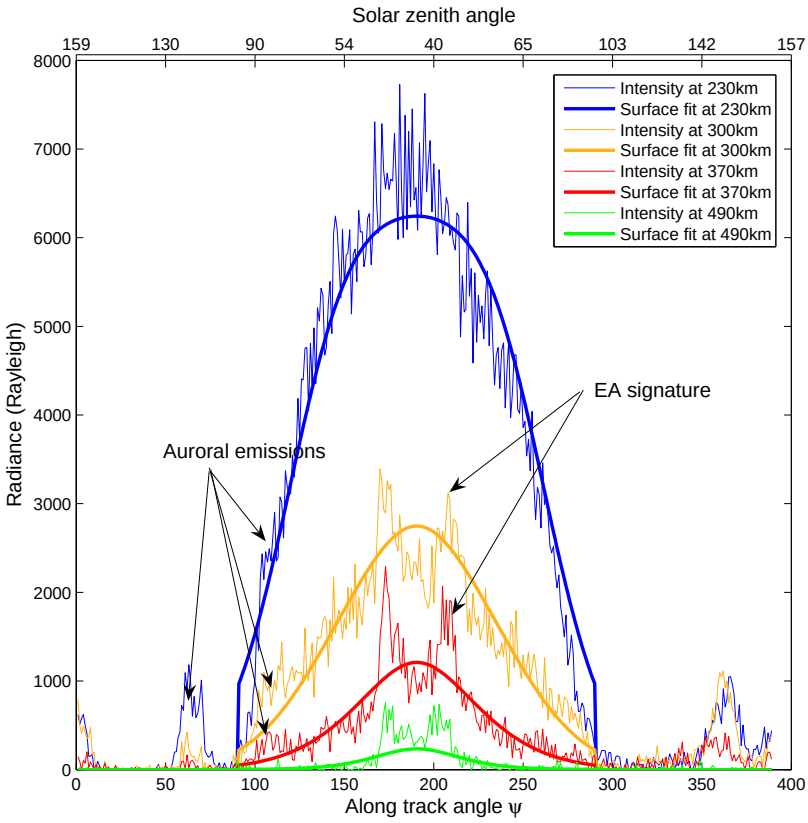

Fig. 2.6: Day glow fit for SZA at different altitudes.

that the subtracted surface obtained in one iteration bounds the data that is fed in to the next iteration in the fitting process. The process is repeated for a number of iterations until a desired error tolerance is achieved for the surface fit. Typically the subtracted data contains some residual dayglow emissions at low altitudes because the surface obtained in this method does not fit for dayglow at altitudes lower than the peak density altitude i.e. around 200 km. Figures 2.7 and 2.8 show subtracted surfaces obtained at dayside local times 0900, 1400, 1430, and 1830 hours LT, respectively. Figure 2.9 shows the original 1356 Å radiances and the subtracted profiles for successive orbits with dayside equator at 1345 hours LT. The successive orbits are separated by around 25° in longitude. These subtracted profiles have signatures of the night and day side equatorial arcs down to 250 km in altitude, auroral emissions at high latitudes and some residual day glow at low altitudes.

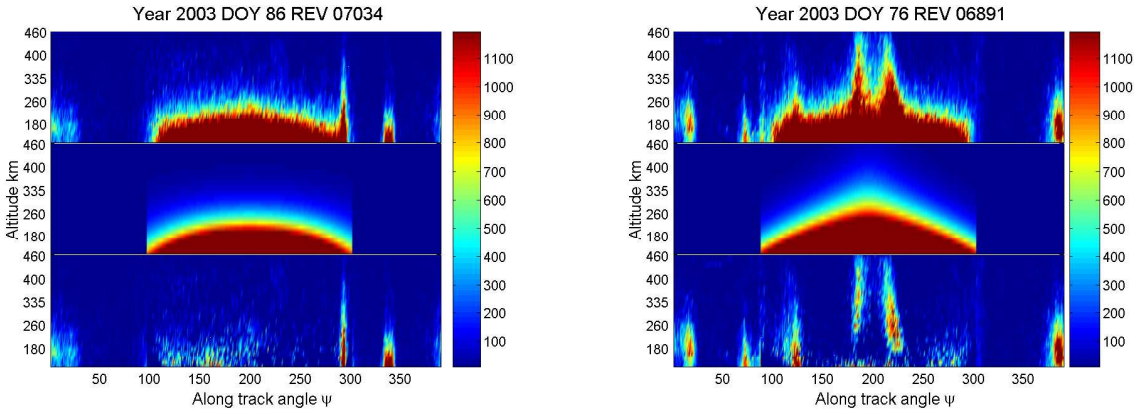

Fig. 2.7: GUVI 1356 Å radiance, day glow fit and subtracted radiance at dayside LT 0900 and 1400 hours, respectively.

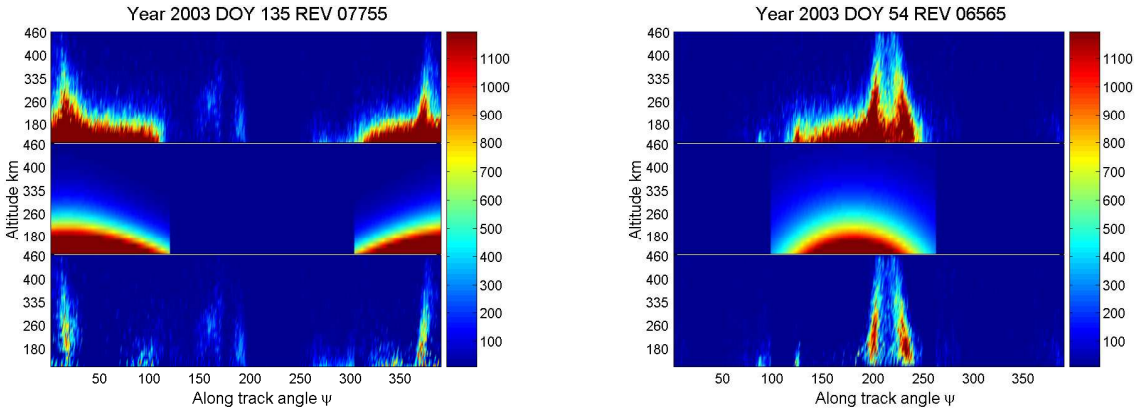

Fig. 2.8: GUVI 1356 Å radiance, day glow fit and subtracted radiance at dayside LT 1430 and 1830 hours, respectively.

2.4 Discussion

With the stars and the dayglow emissions removed, the 1356 Å radiance profiles can be used to study the EIA structure in detail. High altitude pixels corresponding to F-region recombination emissions from an altitude range of 380 to 500 km are averaged and plotted as a function of along track angle. This technique provides clear signatures of the EIA that show its intensity and distribution along the TIMED orbit or essentially with latitude. Figure 2.10 shows both integrated and altitude radiance profile for a GUVI file.

The well developed equatorial arcs located symmetrically about the magnetic equator can be clearly seen. The integrated radiance profile has even lesser contribution from auroral

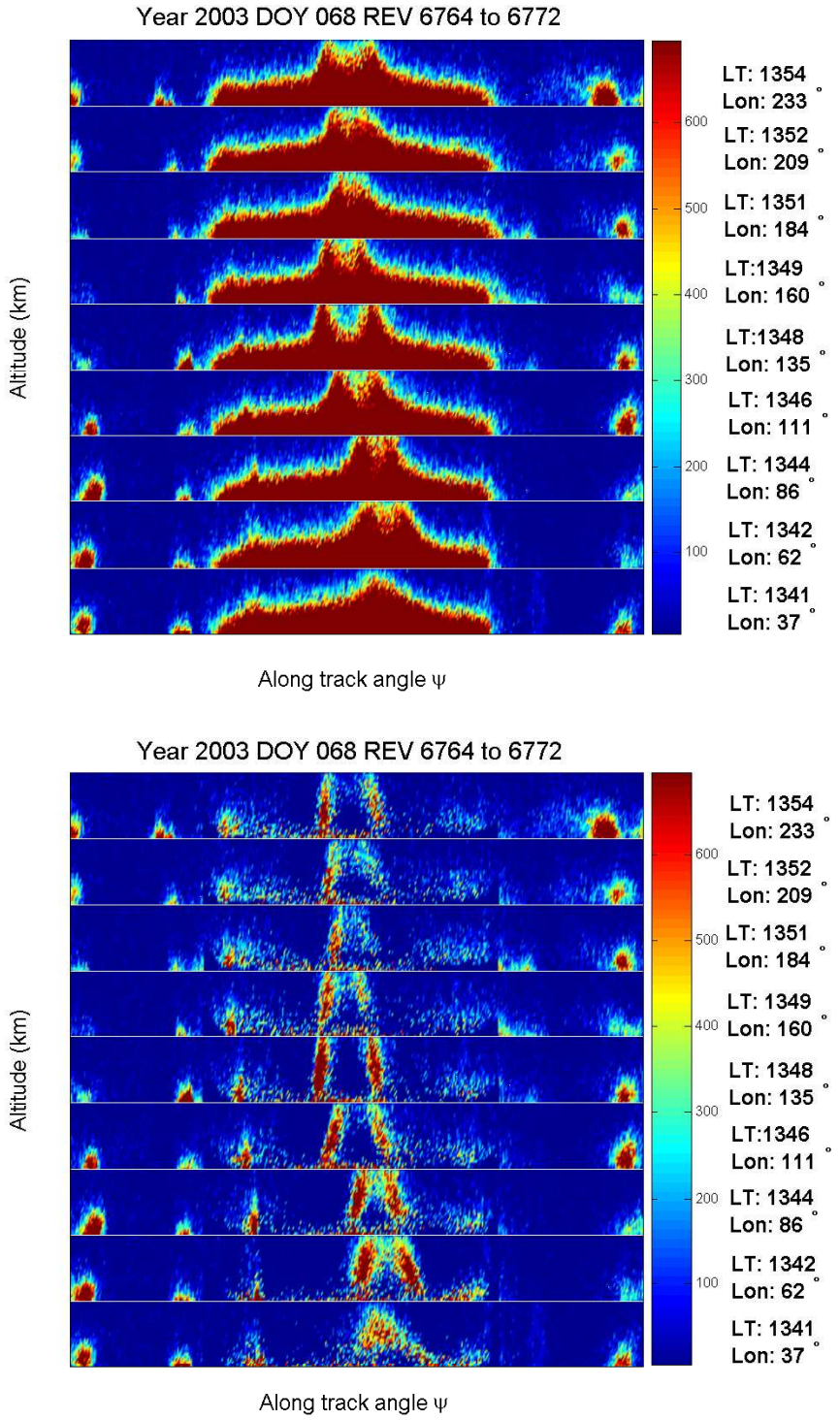

Fig. 2.9: GUVI 1356 Å data and subtracted radiance at an altitude range of 230 to 520 km for successive orbits at dayside LT 1345 hours.

Table 2.1: Factors for comparing EIA signatures in GUVI limb files.

Local time	Longitude	Season	Magnetic activity
EIA variability with local time			
0945 hours	355 °	March equinox	Quiet
1345 hours	356 °	December solstice	Quiet
1730 hours	354 °	December solstice	Quiet
EIA variability with longitude			
1346 hours	46 °	December solstice	Quiet
1341 hours	356 °	December solstice	Quiet
EIA variability with season			
1628 hours	302 °	equinox	Quiet
1632 hours	303 °	June solstice	Quiet
EIA variability with magnetic activity			
1524 hours	153 °	December solstice	Quiet
1533 hours	147 °	equinox	Disturbed

and photoelectron impact emissions than the subtracted radiance image. It is useful to look at these profiles alongside the geomagnetic and solar flux indexes for that period. Figure 2.10 shows 3-hour planetary K (K_p) index for the previous 72 hours from the orbital UT. The daily and 81 day average F10.7 and the DsT in nT is shown for the corresponding day. Also given is the Hemispheric Power in units of GW which is an index of ionospheric heating from the energy flux due to precipitating high energy charged particles in the auroral regions. The potential difference across the polar caps in kV is also given for the current day. This is an index of magnetospheric disturbance and is about 15 to 50 kV during quiet times. During intense magnetospheric storms, the cross cap potential difference may increase up to 200 kV [1]. DsT is an hourly index while Hemispheric Power and Cross-cap Potentials vary in much smaller time scales of 15 minutes and 5 minutes UT, respectively. When the EIA is well formed, the recombination radiances peak to around 600 to 800 Rayleigh. The EIA formation varies considerably with local time, longitude, seasons and geomagnetic activity. Figures 2.10 to 2.18 compare the variability of the observed EIA structure for limb data from year 2004 with each of the factors. The different factors for which the EIA signatures

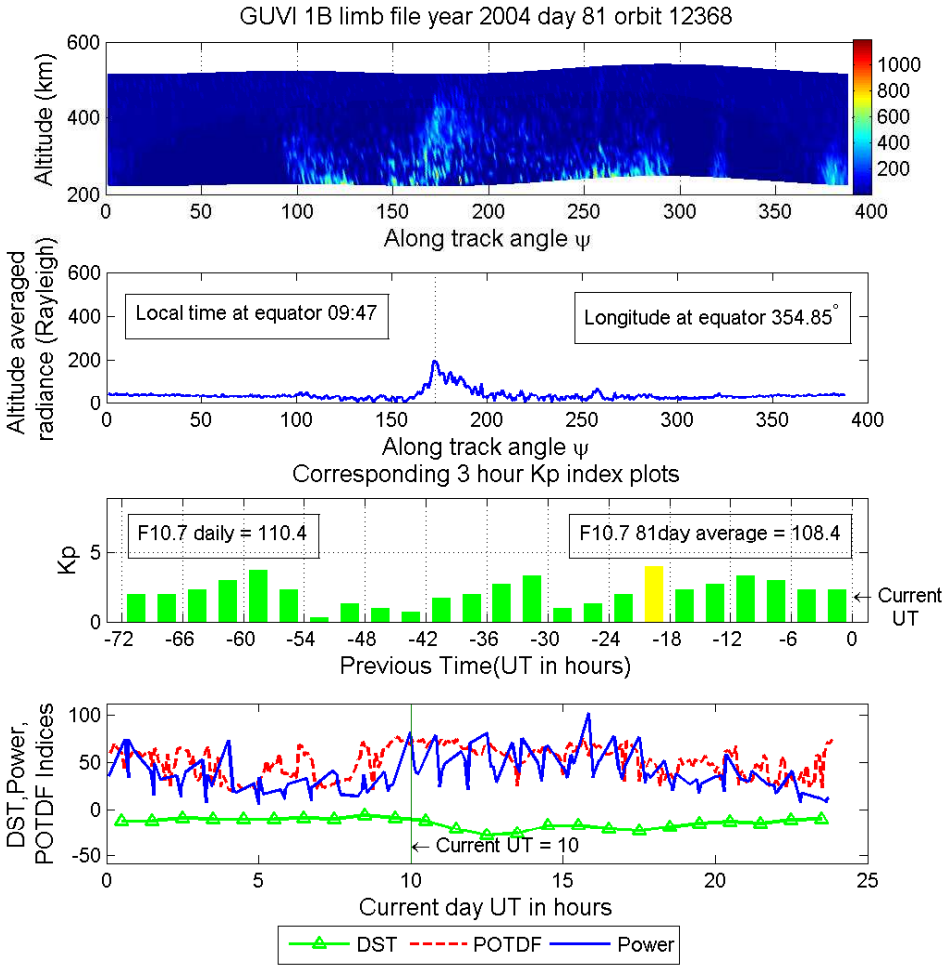

Fig. 2.10: EIA variability with local time: Subtracted 1356 Å radiances 355° longitude, March equinox at 0945 hours.

are compared are summarized in Table 2.1.

Figures 2.10 to 2.12 compare the EIA variability when the dayside equator crossing is at 0945, 1345 and 1730 hours LT, respectively, at different seasons at 350° longitude approximately. It can be observed that the EIA is strongest at 1300-1500 hours LT. It is sparingly formed during morning hours and the magnitude of the EIA peaks drop significantly during evening LT. Further, at a given local time, season and solar flux, the EIA structure is found to vary considerably with longitudes as seen in figs. 2.13 and 2.14. Seasonal variation has a significant impact on EIA formation. Figures 2.15 and 2.16 show that

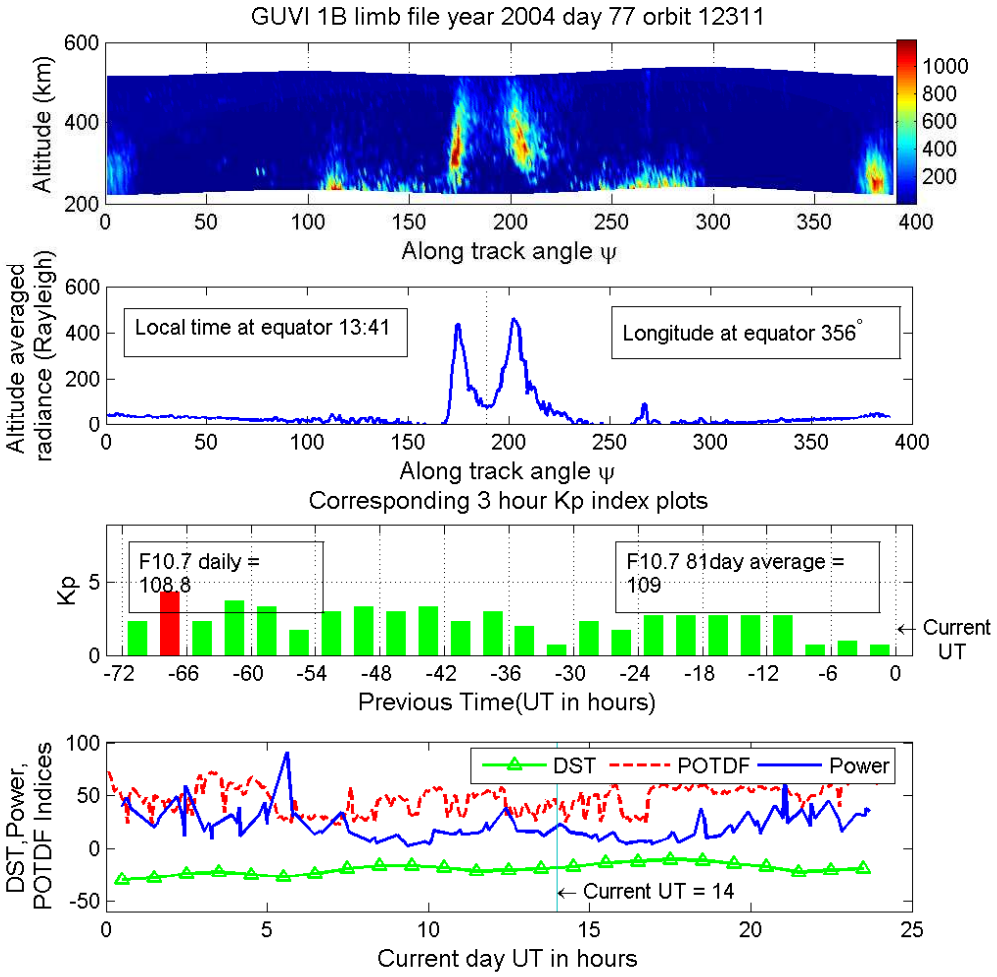

Fig. 2.11: EIA variability with local time: Subtracted 1356 Å radiances 356° longitude, December solstice at 1345 hours.

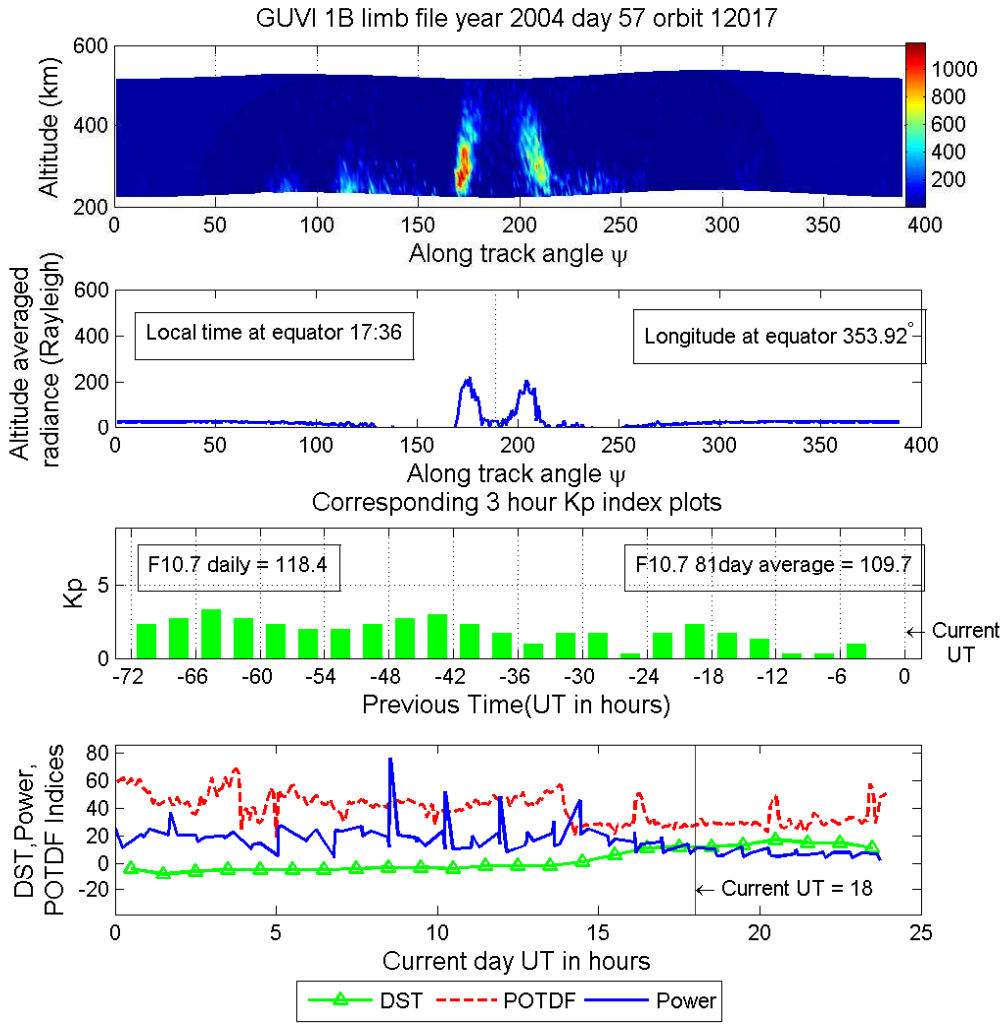

Fig. 2.12: EIA variability with local time: Subtracted 1356 Å radiances 354° longitude, December solstice at 1730 hours.

at a given LT and longitude, the EIA is well-formed during December solstice but there are almost no recombination emissions during June solstice. The considerable difference in the intensities observed during the two periods can also be attributed to the difference in the corresponding daily solar flux values observed. Figures 2.17 and 2.18 compare between observed radiances during quiet and disturbed magnetic times for the same LT, longitude. The disturbed period is marked by significantly high K_p indices and drastically low DsT values at the orbital UT. Intense auroral emissions can be seen down to mid-latitudes during the disturbed magnetic period. Due to anomalously high intensities observed, it is harder to obtain a reasonable surface fit for the dayglow emissions during magnetic disturbed times.

2.5 Day-to-day Variability of the EIA

Apart from the dependence of the day time EIA formation on the factors discussed above, GUVI data shows a considerable day to day variability in the EIA profiles. To collectively analyze all the available GUVI limb files, EIA radiances are graphed for every orbit and shown with progressing UT. GUVI limb radiances with emissions from stars and glints subtracted, are summed over high altitudes from 380 to 500 km and plotted as a function of magnetic latitude. These set of files are grouped into a movie for every year and can be analyzed along with the corresponding K_p indexes to understand the overall progression of EIA with local time, seasons and solar flux. More information on these movies can be found in Appendix B.

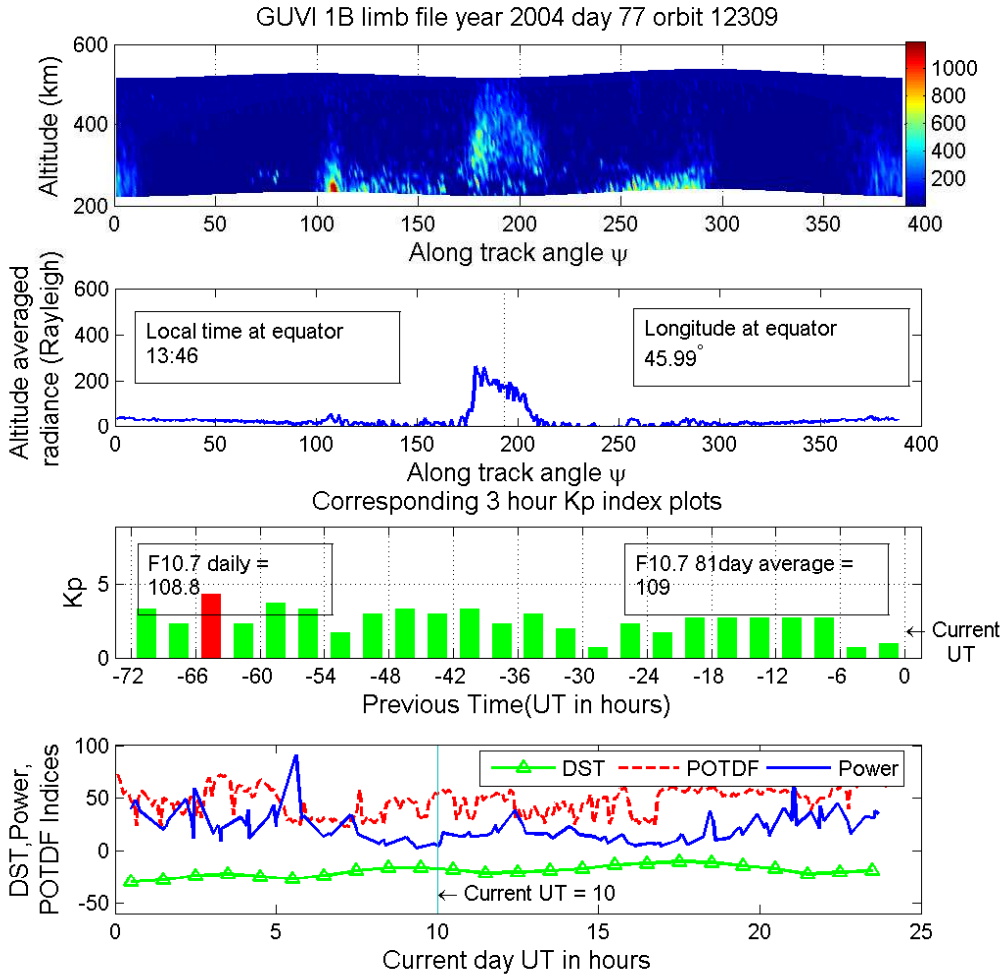

Fig. 2.13: EIA variability with longitude: Subtracted 1356 Å radiances at 1346 hours, December solstice at 46° longitude.

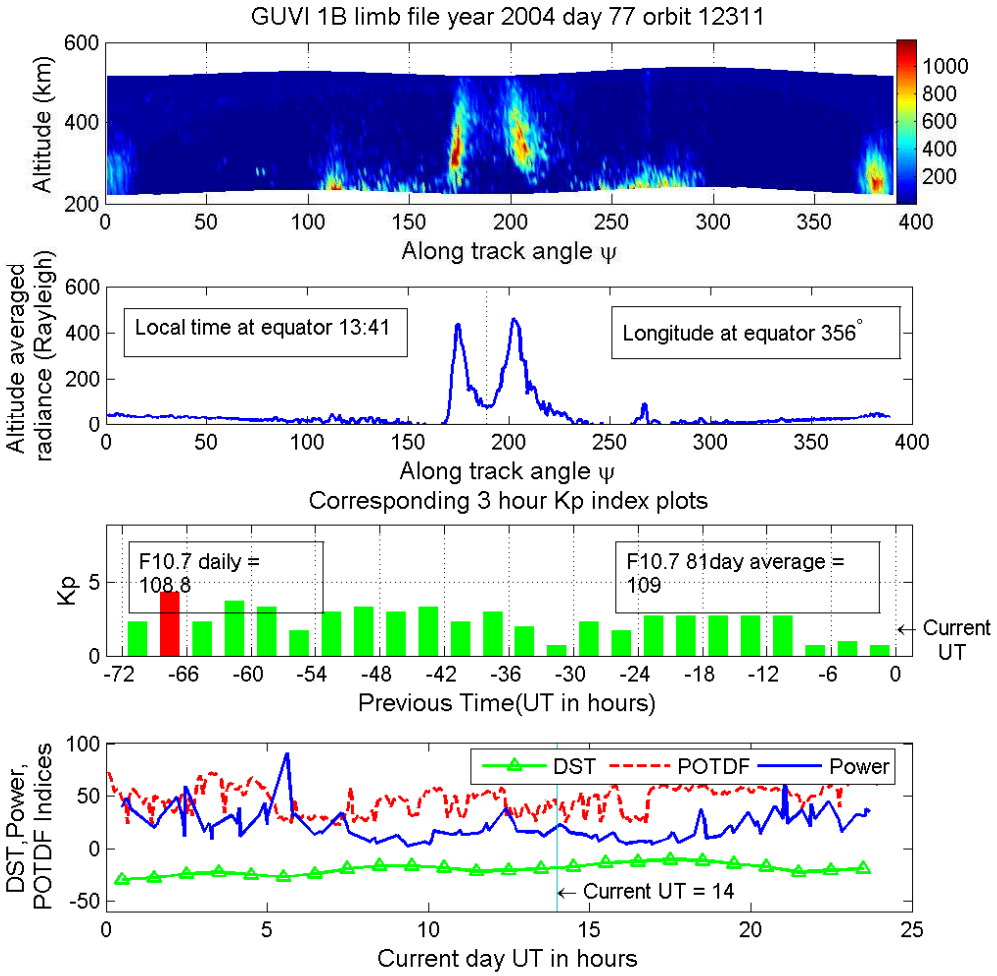

Fig. 2.14: EIA variability with longitude: Subtracted 1356 Å radiances at 1341 hours, December solstice at 356° longitude.

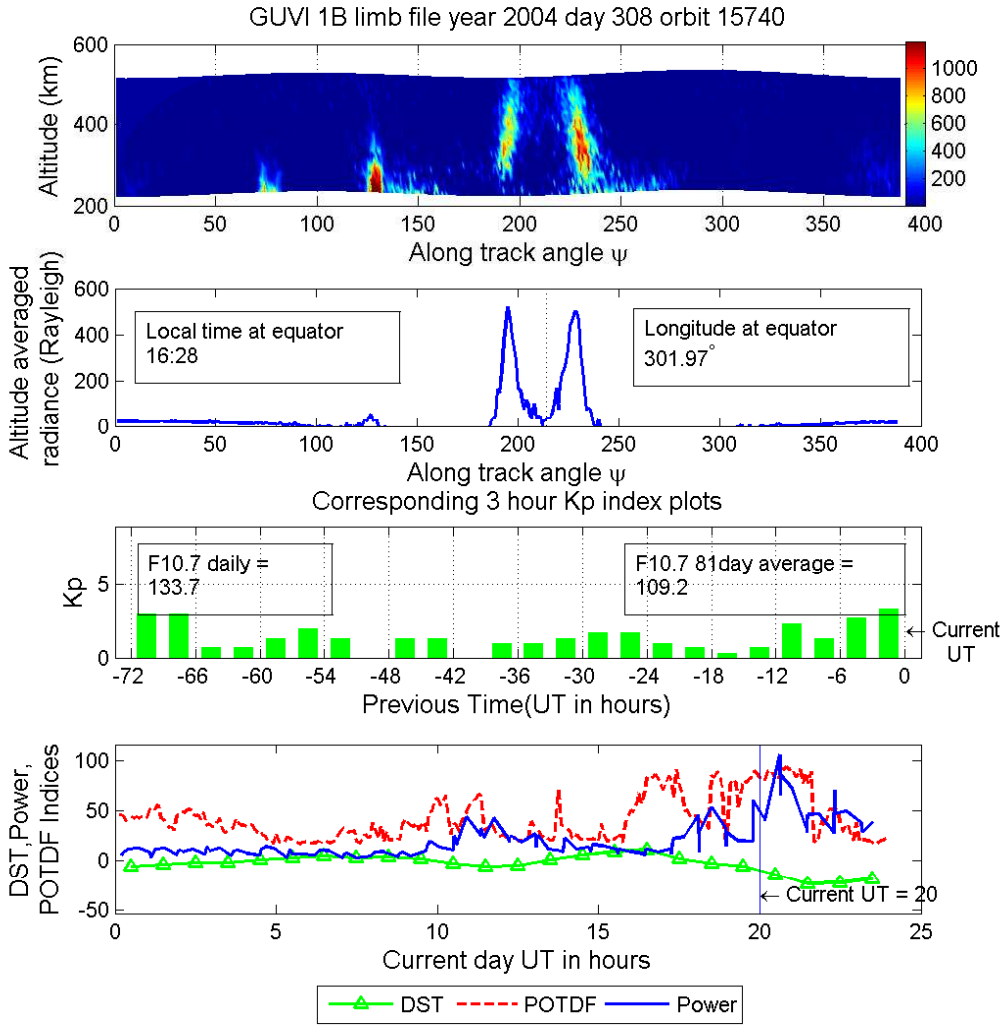

Fig. 2.15: EIA variability with season: Subtracted 1356 Å radiances 1630 hours LT, 302° longitude, equinox.

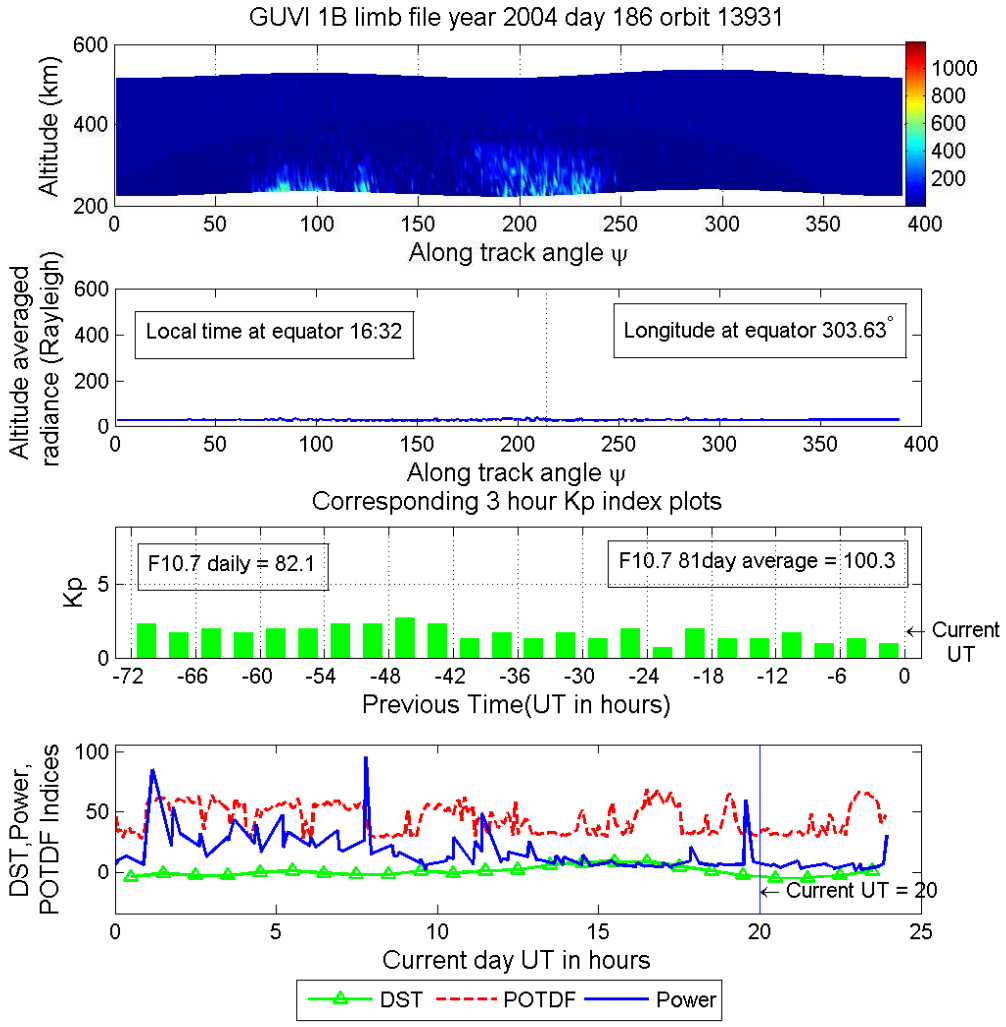

Fig. 2.16: EIA variability with season: Subtracted 1356 Å radiances 1630 hours LT, 303° longitude, June solstice.

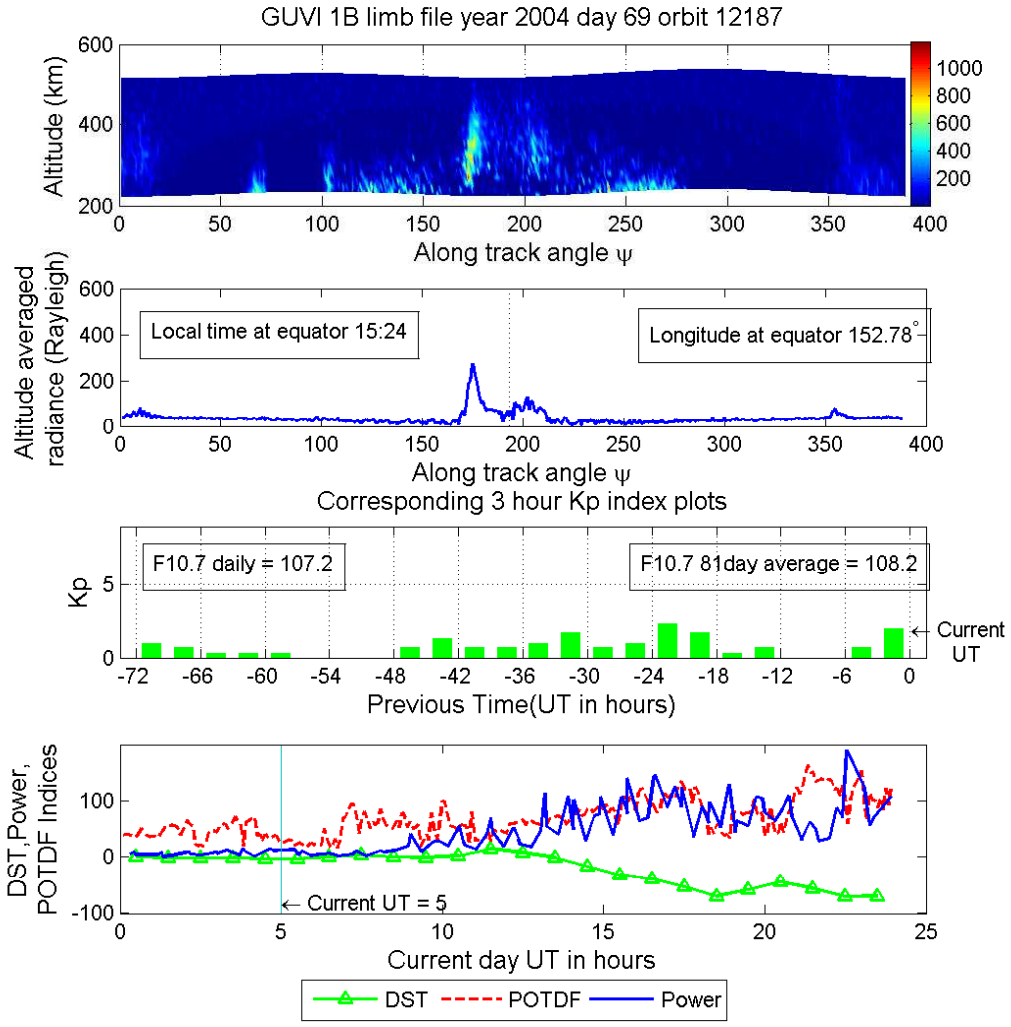

Fig. 2.17: EIA variability with geomagnetic activity: Subtracted 1356 Å radiances 1524 hours LT, 153° longitude, geomagnetic quiet.

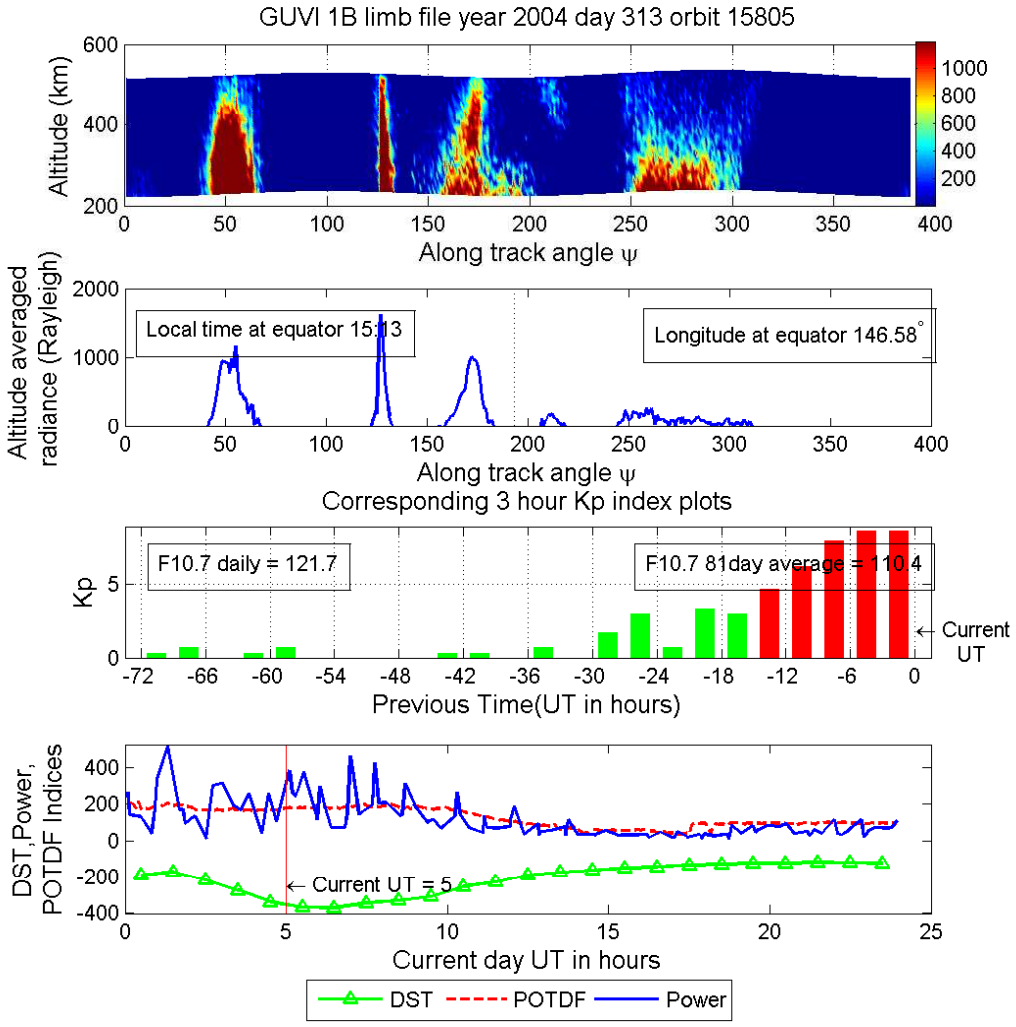

Fig. 2.18: EIA variability with geomagnetic activity: Subtracted 1356 Å radiances 1513 hours LT, 147° longitude, geomagnetic disturbed.

Chapter 3
Comparison of GUVI 1356 Å Radiance with Ionospheric Models

3.1 Introduction

The F-region 1356 Å emissions can be attributed to oxygen ion (O^+) recombination process. As was shown earlier, the F-region O^+ recombination loss rate is directly related to electron densities due to F-region EIA. GUVI limb data shows clear signatures of high altitude O^+ recombination emissions in the equatorial anomaly regions on the dayside. These emissions can be compared with electron density profiles obtained from ionospheric models to understand how well the models predict the dayside equatorial ionosphere.

DeMajistre et al. [15] have shown that 1356 Å limb emissions measured by GUVI on the night side can be inverted to obtain night time electron density profiles. These values were then compared with ground-based electron density measurements and a good agreement between the two was found except for a few post midnight measurements. The disagreement during post midnight sectors were attributed to some secondary unaccounted sources of night time 1356 Å emissions [15].

This chapter discusses a method where in, instead of retrieving electron densities from 1356 Å emissions, global electron density profiles obtained from ionospheric models namely GAIM and TIMEGCM are used to reconstruct pseudo-limb radiances. GUVI limb field of view geometry and the TIMED satellite position are used to reconstruct these pseudo-limb radiance profiles which can be compared with actual GUVI limb observations.

3.2 Radiometric Analysis

This section is a description of the radiometric analysis that leads to the conversion

of electron density values to O^+ 1356 Å radiance. Radiance (or Photon Stearance) at the collector can be defined as the flux per collector unit area per unit solid angle. It is given in units of W cm^{-2} sr^{-1} or photons s^{-1} cm^{-2} sr^{-1} [16]. The solid angle is subtended by the radiating source on to the collector.

Radiant flux Φ is defined as the number of photons per second and is given in units of W or quanta per second. If the flux source is a differential volume element ΔV cm^3, the flux emitted from the source is given in terms of volume emission rate ρ or photons per unit volume per second given in units of q cm^{-3} s^{-1}.

$$\phi = \tau(s)\rho\Delta V \text{ qs}^{-1}, \tag{3.1}$$

where $\tau(s)$ is the transmissivity which indicates the optical depth of the atmosphere for any spectral line. Since the 1356 Å line does not get significantly absorbed or scattered through the ionosphere, it is said to be optically thin and has a transmissivity $\tau(s) = 1$ everywhere. The volume emission rate for 1356 Å emissions due to O^+ recombination is proportional to the electron density $[e]$ and is given by

$$\rho = \alpha[e]^2 \text{ qcm}^{-3}\text{s}^{-1}, \tag{3.2}$$

where α is the O^+ recombination coefficient. It is given by [17]

$\alpha = 7.3 * 10^{-13}\sqrt{\frac{1160}{T_e}}$ cm^3s^{-1}.

T_e is the electron temperature in kelvin. If T_e is taken to be a constant at 1160 K then

$\alpha = 7.3 * 10^{-13}$ cm^3s^{-1}.

Combining 3.1 and 3.2, the differential flux from a volume element ΔV is

$$\Delta\Phi = \alpha[e]^2\Delta V \text{ qs}^{-1}. \tag{3.3}$$

To find the flux at any point on the surface of a sphere of radius s around V we write flux (due to ΔV) per unit area at distance s is

$$\Delta\Phi = \frac{\alpha[e]^2\Delta V}{4\pi s^2}\ \mathrm{qs}^{-1}\mathrm{cm}^{-2}. \tag{3.4}$$

The flux on a collector area A_c is given by

$$\Delta\Phi = \frac{\alpha[e]^2\Delta V A_c\cos\theta}{4\pi s^2}\ \mathrm{qs}^{-1}, \tag{3.5}$$

where $A_c\cos\theta$ is the projection of the area A_c on to the plane normal to the line of sight between the collector and the radiant source. The total flux is got by summing up $\Delta\Phi$ due to all volume elements in the field of view (FOV) of the collector.

$$\Phi = \sum_{i\subset points\ in\ FOV} \frac{\alpha[e_i]^2\Delta V_i A_c\cos\theta_i}{4\pi s_i^2}\ \mathrm{qs}^{-1}. \tag{3.6}$$

Radiance is defined as the flux per unit area per unit solid angle, so we have

$$L = \frac{\Phi}{A_c\Omega_c}. \tag{3.7}$$

$$L = \frac{\alpha}{4\pi\Omega_c}\sum_{i\subset points\ in\ FOV} \frac{[e_i]^2\Delta V_i\cos\theta_i}{s_i^2}\ \mathrm{qs}^{-1}\mathrm{sr}^{-1}\mathrm{cm}^{-2}, \tag{3.8}$$

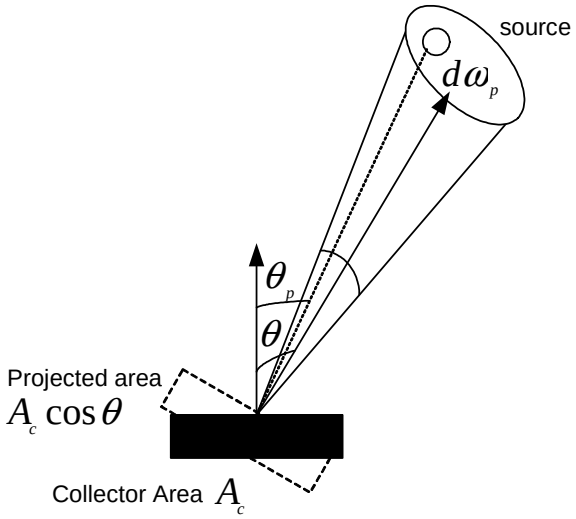

Fig. 3.1: Projected solid angle and projected area.

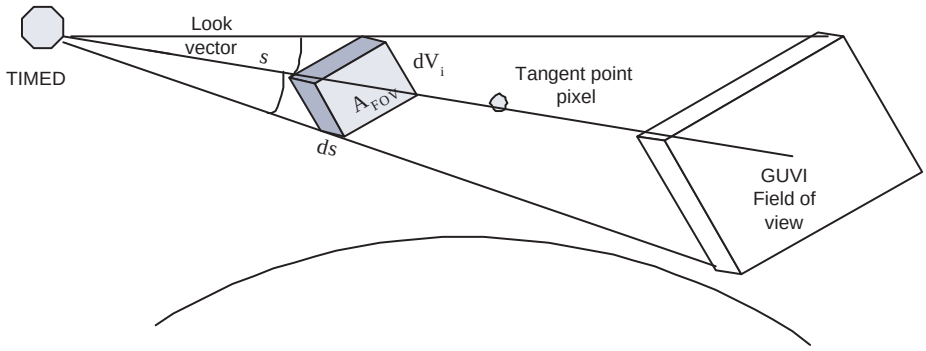

Fig. 3.2: Radiance values are computed by summing electron density values along GUVI limb FOV.

where Ω_c is the projected solid angle subtended by the radiating source on the collector. The projected solid angle [18] is given by $\Omega_c = \int_\omega \cos\theta_p \delta\omega_p$ sr.

As given in fig. 3.1, $\delta\Omega_c$ is the projection of each differential element $\delta\omega_p$ each of which is at an angle θ_p from the normal to the collector plane [18]. For small solid angles ω, $\theta_p \forall p$ is taken to be a constant θ.

So we can write,

$$\Omega_c = \cos\theta \int_\omega \delta\omega_p \text{ sr}, \tag{3.9}$$

$$\Omega_c = \omega \cos\theta \text{ sr}. \tag{3.10}$$

For the construction of limb radiance from electron density distribution, GUVI limb field of view is broken down into multiple differential volume elements ΔV at increasing distances s along the FOV as shown in fig. 3.2.

The solid angle ω subtended by any source element ΔV can be given by

$$\omega = \frac{A_{FOV}}{s^2} \text{ sr}, \tag{3.11}$$

where A_{FOV} can be given as

$$A_{FOV} = 2s \tan\frac{\sigma}{2} * 2s \tan\frac{\beta}{2} \text{ cm}^2, \tag{3.12}$$

where σ and β are the angles subtended at the two faces. From GUVI field of view we know $\sigma = .85°$ and $\beta = .4°$. For small angles, $\tan\frac{\sigma}{2} \approx \frac{\sigma}{2}$ and $\tan\frac{\beta}{2} \approx \frac{\beta}{2}$ and

$$A_{FOV} = s^2\sigma\beta. \tag{3.13}$$

From eq. 3.11 $\omega = \sigma\beta = .34°$. For such small solid angles, Ω_c can be approximated as per eq. 3.10. Radiance L can be written as

$$L = \frac{\alpha}{4\pi\omega} \sum_{i \subset points\ in\ FOV} \frac{[e_i]^2 \Delta V_i}{s_i^2}\ \mathrm{qs}^{-1}\mathrm{sr}^{-1}\mathrm{cm}^{-2}. \tag{3.14}$$

To get radiance in units of Rayleigh, where 1 Rayleigh $= \frac{1}{4\pi}10^6\ \mathrm{qs}^{-1}\mathrm{cm}^{-2}\mathrm{sr}^{-1}$,

$$I = \frac{4\pi L}{10^6}\ \text{Rayleigh}, \tag{3.15}$$

Substituting for L from eq. 3.14 we get Radiance in Rayleigh,

$$I = \frac{\alpha}{\omega 10^6} \sum_{i \subset points\ in\ FOV} [e_i]^2 \frac{\Delta V_i}{s_i^2}\ \text{Rayleigh}. \tag{3.16}$$

From fig. 3.2 each volume ΔV_i of length Δs_i can be written as $A_{FOV}\Delta s_i$. From eq. 3.13 we get

$$\Delta V_i = s^2 \Delta s_i \omega\ \mathrm{cm}^3. \tag{3.17}$$

3.3 Construction of 1356 Å Radiance Profiles from Model Data

Ionospheric models GAIM and TIMEGCM provide global 3-dimensional electron distribution for all UT. Both the models cover an altitude region that correspond to the altitude range of GUVI limb measurements, i.e. 100 to 500 km. GAIM has a resolution of around 20 km in altitude, 3° to 5° in latitude and 15° in longitude in geocentric coordinates. Electron densities per cm^3 are available in time steps of 15 UT minutes.

TIMEGCM has a 5° resolution in both geocentric longitude and latitude. The altitude

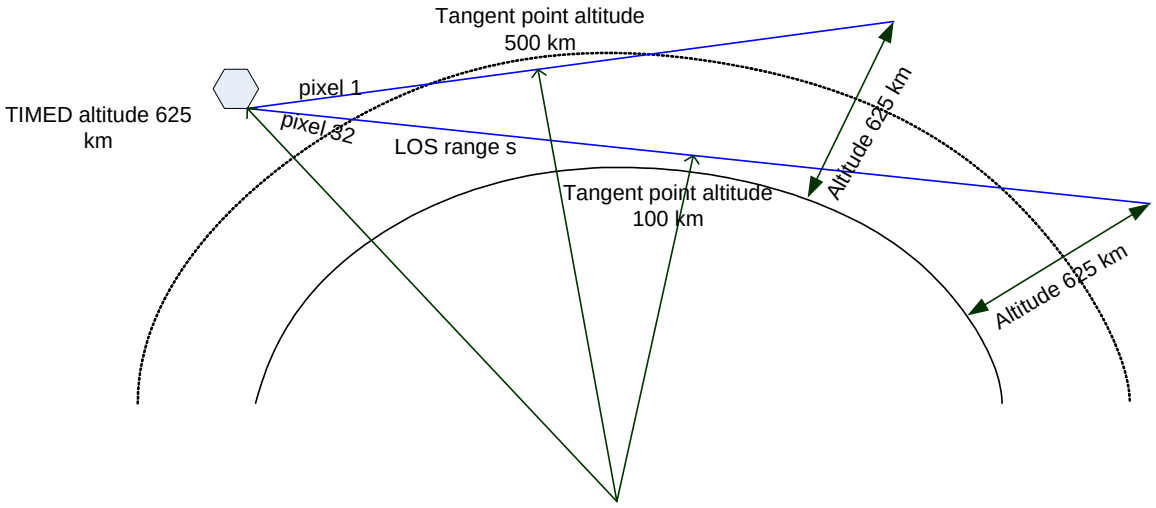

Fig. 3.3: Line of sight range for pixels at different altitudes for a spherical Earth.

is given by geopotential height. It depends upon varying pressure levels and has a resolution that varies with latitude and longitude. Electron densities per m^3 are available in 1-hour time steps.

To improve signal statistics in GUVI limb data and to reduce processing time, radiance in 14 along track pixels are averaged for every scan as explained in Chapter 2. The geolocation of 14 along track pixels is taken from the center (7th along track) pixel for every scan. For a given GUVI limb file, using its tangent point coordinates and TIMED position coordinates a line-of-sight vector is constructed for every limb altitude. The line of sight FOV is split into differential volume elements ΔV_i of a fixed length Δs and increasing area A_{FOV} as shown in fig. 3.2. All geometry is done in a cartesian coordinate system.

The differential distance Δs is chosen such that successive ΔV_i elements are closer than the resolution provided by the model. This ensures that our computations include electron density variations of the smallest scale provided by the model. A distance $\Delta s = 10$ km works well for both GAIM and TIMEGCM. The line-of-sight range is allowed to extend up to the spacecraft altitude (625 km) beyond the tangent point. The line-of-sight range is longer for low altitude pixels (pixel 32) than the high altitude ones (fig. 3.3).

Electron density at these volume elements are obtained by a nearest neighbor interpolation over the model electron density array. A summation of the square of these electron

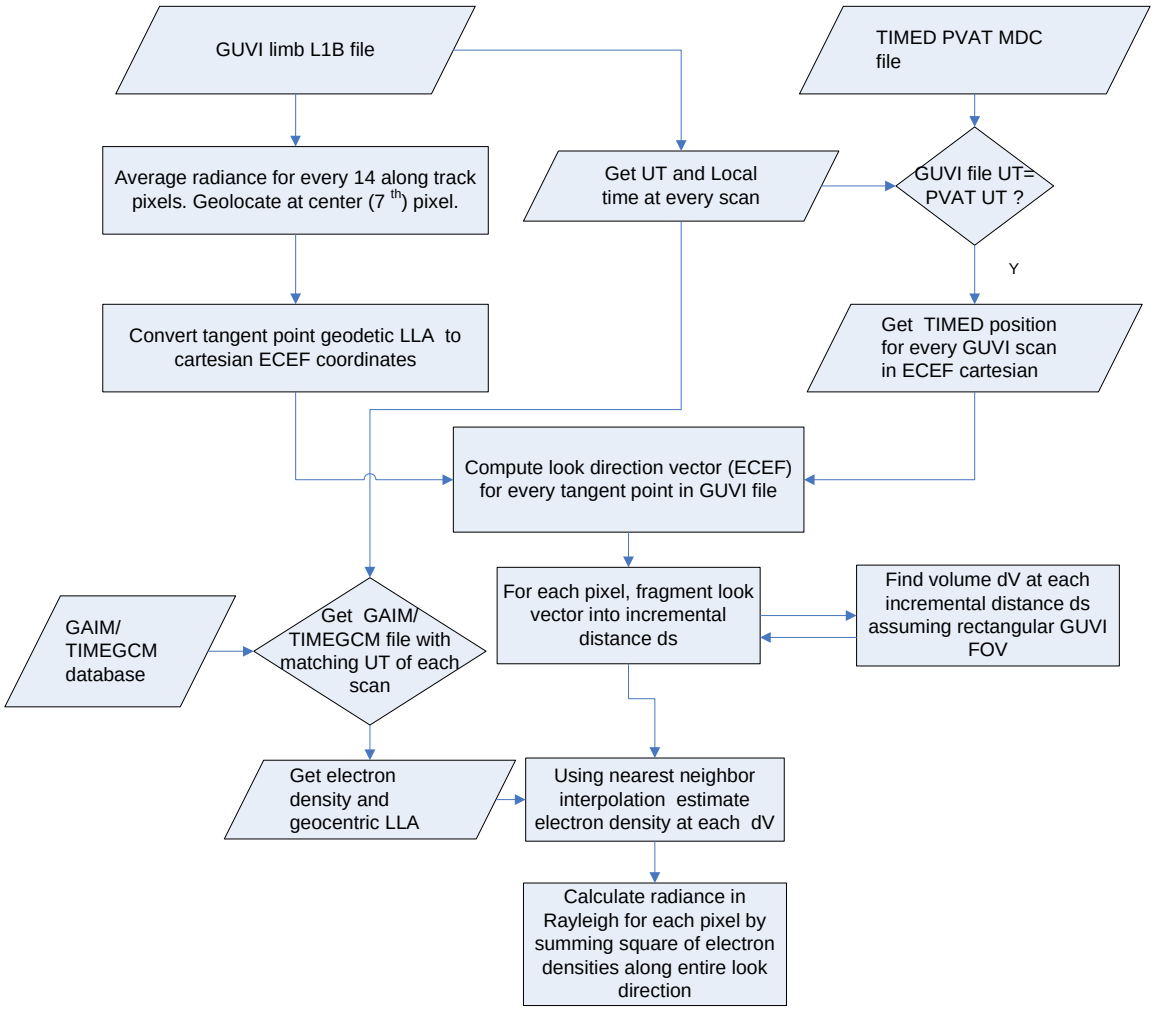

Fig. 3.4: Algorithm for constructing 1356 Å radiance profiles using electron densities from ionospheric models.

density values and subsequent computation as described in sec. 3.2 gives 1356 Å emission profiles that can be directly compared with the corresponding GUVI limb file.

To avoid comparing with the low altitude photoelectron impact emissions present in GUVI limb data, both GUVI limb data and the constructed radiance data from models are averaged over the top 15 pixels that corresponds to an altitude range of 380 to 520 km. This ensures that the comparison is done only for recombination emissions due to EIA in the F-region. A flowchart describing this process is shown in fig. 3.4.

3.4 Discussion of Comparison Results

Figure 3.5 compares the radiance profiles obtained from the model electron densities with GUVI limb emissions for a sample orbit taken for March equinox period. It can be seen that high altitude radiances from GAIM and TIMEGCM are in fairly good agreement with GUVI observations. However the integrated radiance observed by GUVI as shown in fig. 3.5 has some contribution from the high intensity, low altitude photoelectron impact ionization emissions. These emissions are not included in the radiance obtained from models and so it can be seen that the models over-estimate the high altitude recombination emissions observed by GUVI, by a small amount.

Figure 3.6 compares between GUVI and GAIM radiance profiles as a function of altitude. Figures 3.7 to 3.9 compare GAIM and GUVI radiance profiles for successive orbits, i.e. for different longitudes at the same day and local time. It can be observed that radiance modeled by GAIM follows the general profile of GUVI-observed 1356 Å emissions. It also shows clear features of the day time equatorial anomaly. However, the actual amplitudes from GAIM predicted radiance are higher than those of GUVI. Also the symmetry in the

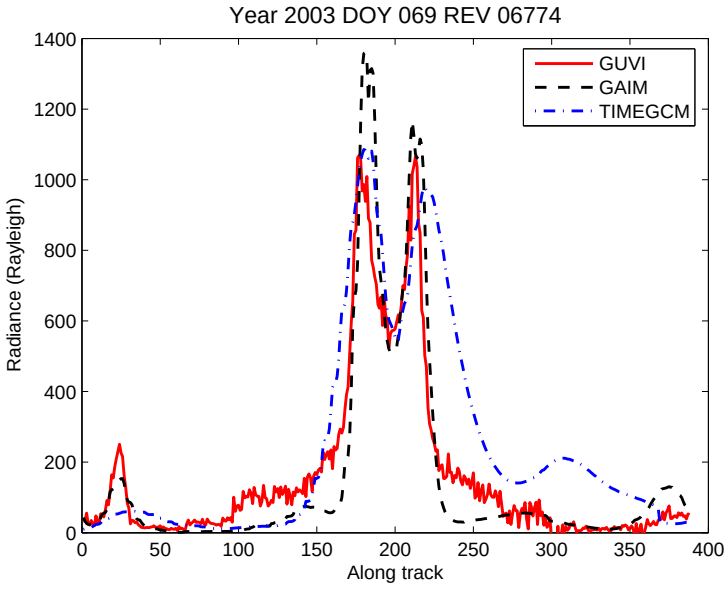

Fig. 3.5: Radiance profiles from GUVI and models GAIM, TIMEGCM for March equinox. The longitude and local time at the descending node equator is 215° (Western-American sector) and 1530 hours, respectively.

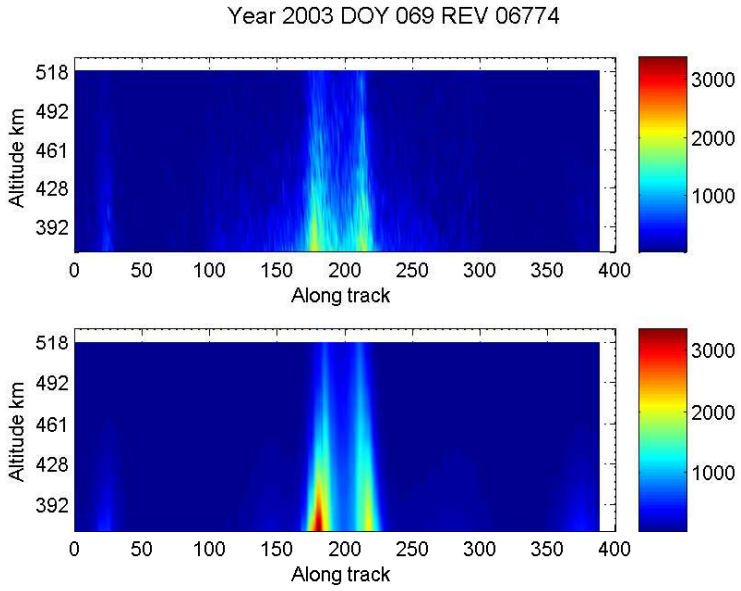

Fig. 3.6: Radiance-altitude profiles from GUVI (top) and GAIM (bottom) for March equinox. The longitude and local time at the descending node equator is 215° (Western-American sector) and 1530 hours, respectively.

equatorial arcs seen in GUVI may not always repeat with GAIM profiles.

Some of the differences in peak amplitudes between radiances from GAIM and GUVI can be attributed to the following approximations. As defined earlier in sec. 3.2 the recombination coefficient α is given by $\alpha = 7.3 * 10^{-13}\sqrt{\frac{1160}{T_e}}$ cm^{3}s^{-1} where T_e is the electron temperature in Kelvin. T_e varies with altitude, local time and seasons. In this algorithm, T_e has been assumed to be a constant at 1160 K and α is taken to be a constant 7.3*10^{-13} cm^{3}s^{-1}. Since radiance varies inversely with $\sqrt{T_e}$, the actual contribution to the total radiance due to each volume element ΔV is $\frac{1}{\sqrt{n}}\alpha[e]^2$ where n is the ratio $\frac{T_e}{1160}$. Since the analysis here pertains to the day side EIA, the actual T_e values over the local times of interest are higher, and hence radiance profile calculated from GAIM should be slightly lower than the values obtained. This approximation may not be too significant to account for the difference between the two radiance profiles. There is also a minor amount of approximation in the calculation of volume emission rate ρ. It is given by DeMajistre et al. [15] as

$$\rho = \alpha[e]^2(1 - \frac{[O_2^+] + [NO^+] + [H^+]}{[O^+]})\ \text{qcm}^{-3}\text{s}^{-1}. \tag{3.18}$$

In writing eq. 3.2, the density of the molecular ions $[O_2^+]$, $[NO^+]$, $[H^+]$ have been assumed to be much lower than the dominant $[O^+]$ concentration in F-region altitudes to make any significant contribution towards the volume emission rate. However, any increase in the concentration of these molecular ions in day time F-region will result in a slightly lower value for ρ than computed. It should also be noted that ρ is proportional to the square of electron density, hence any errors of small magnitude in electron density values obtained from the model get squared in the computation of radiance profiles.

3.5 Development of EIA in GAIM with Local Time and Longitude

Since GAIM results are in relatively good agreement with GUVI observations, it is fair to study EIA morphology as predicted by GAIM. Radiance profiles at the same longitudes for all local times of a day can be obtained from GAIM, which cannot be done with GUVI observations because GUVI takes close to 60 days to sample the same longitude at the next local time hour. In this section EIA development with respect to local time and longitude in GAIM is discussed.

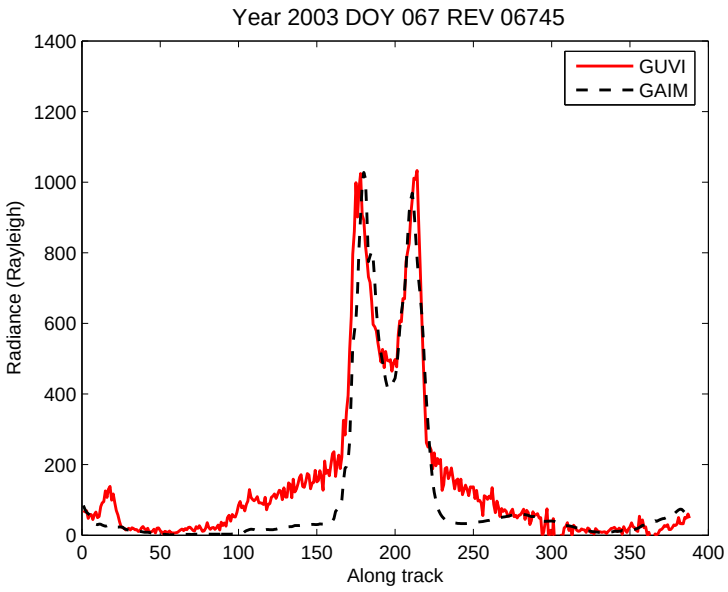

Fig. 3.7: Radiance profiles from GUVI and GAIM for March equinox. The longitude and local time at the descending node equator is 200° (Pacific sector) and 1600 hours, respectively.

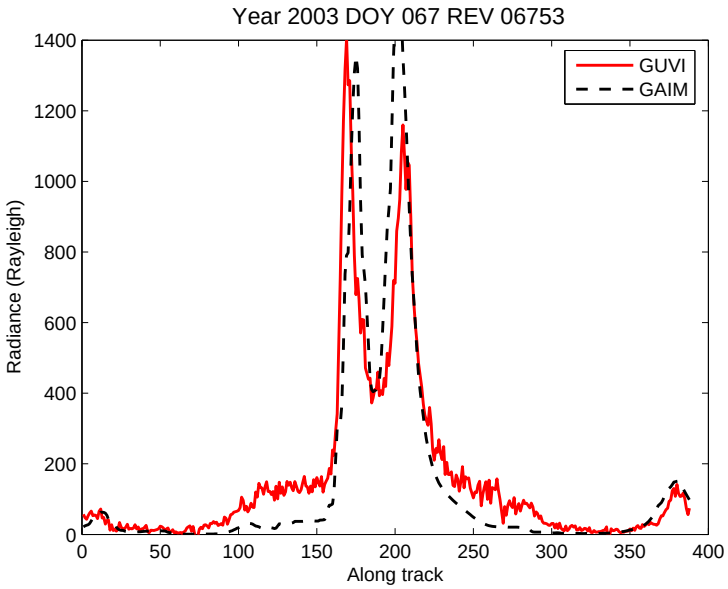

Fig. 3.8: Radiance profiles from GUVI and GAIM for March equinox. The longitude and local time at the descending node equator is 8° (African-Indian) and 1550 hours, respectively.

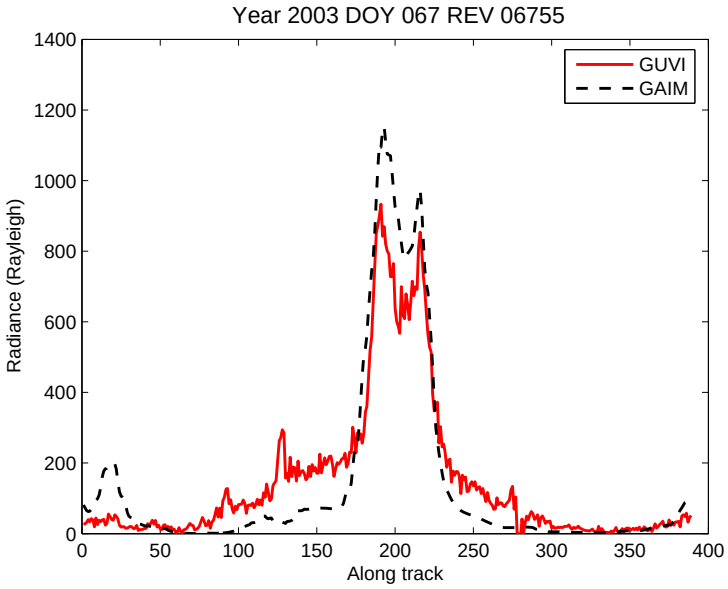

Fig. 3.9: Radiance profiles from GUVI and GAIM for March equinox. The longitude and local time at the descending node equator is 320° (Brazilian sector) and 1550 hours, respectively.

EIA profile predicted by GAIM for a given GUVI orbit can be observed over all local times of day. GUVI field of view geometry is selected for a particular orbit and electron densities corresponding to all UT for that day is extracted from the model. Thus a time-dependent radiance profile is obtained for a given GUVI orbit. Figures 3.10 to 3.13 show development of EIA with local time at each longitude sector. Radiances are averaged over an altitude range of 350 to 500 km. The local time in hours at the magnetic equator is given alongside each plot. All the four orbits shown here correspond to the same day.

It can be seen at all longitude sectors that the equatorial plasma density starts to peak at around 0800 hours but the typical double crested EIA does not begin to form until sometime between 1100 to 1300 hours. It should be recalled that we do not have any GUVI observations at this local time due to the yaw maneuver of the TIMED spacecraft. The peak radiances start decreasing from 1800 hours onwards. As with the GUVI orbit, the latitudes at the edges of the plots correspond to the ascending node equator which is about nine hours apart in local time from the descending node equator located at the center of the plots. This explains the increased radiances at the ascending node equator when the descending node equator is at a local time of 0400 or 0500 hours. The plots also clearly show differences between the four longitudinal sectors. There is a slight shift in the along track position of the EIA at any given local time for different longitudinal sectors. This is because the magnetic equator lies at different geographic latitudes in different longitudinal sectors. It can also be seen that the Brazilian sector does not have clearly formed EIA even at 1200 noon. This is because in the Brazilian sector (longitudes 300° to 360°), the magnetic equator does not align favorably with the geographic equator to create a strong fountain effect. This comparison makes it possible to look at EIA variability purely as a function of local time and longitude without any variations due to seasons or solar fluxes.

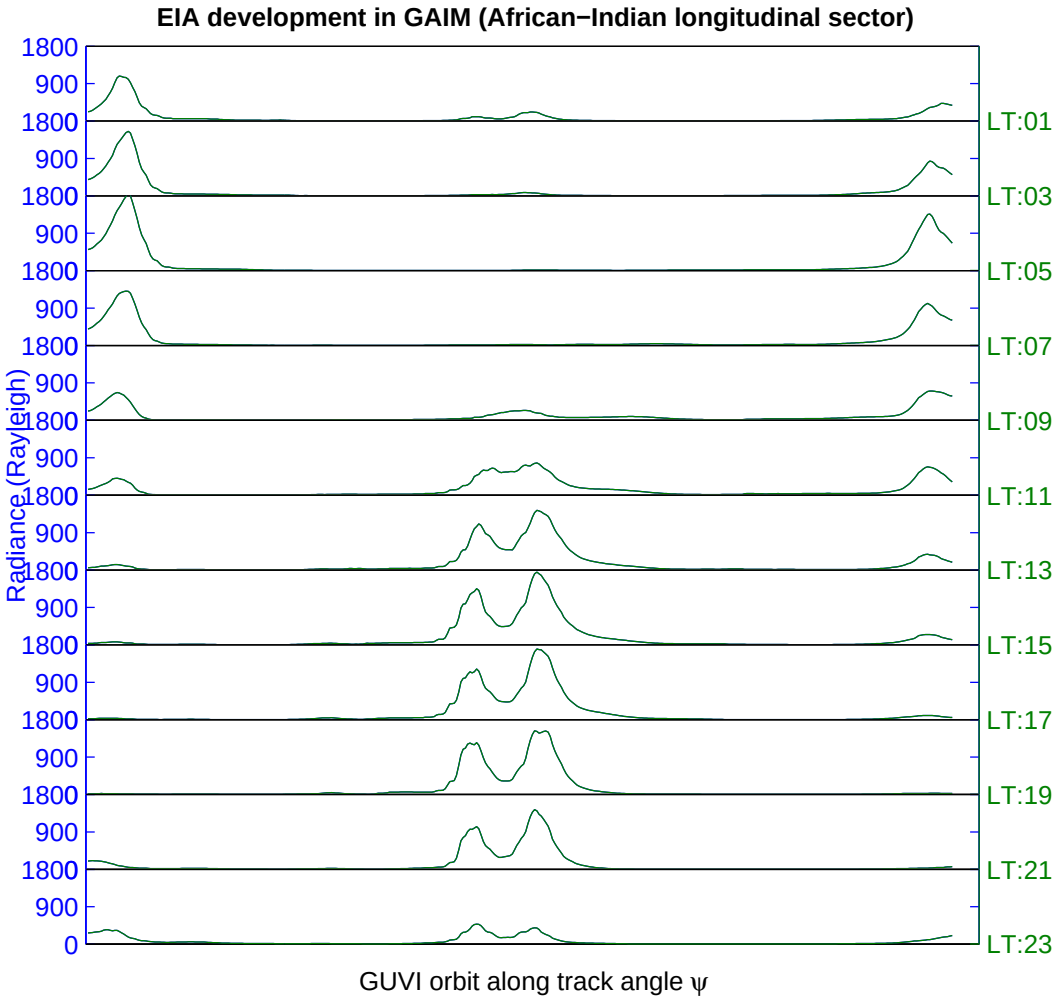

Fig. 3.10: Development of EIA with local time in GAIM at the African-Indian sector (geographic longitude 0° to 150°) during March equinox, 2003.

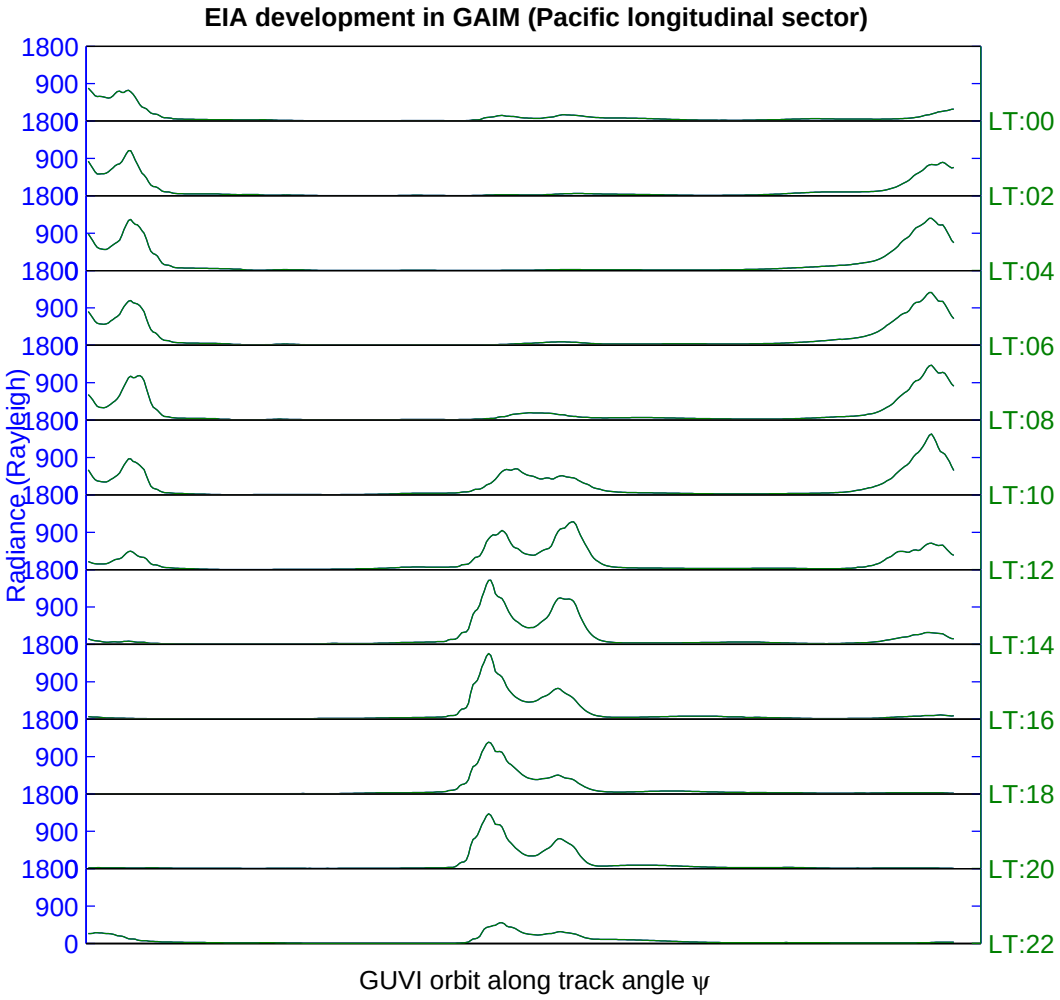

Fig. 3.11: Development of EIA with local time in GAIM at the Pacific sector (geographic longitude 150° to 210°) during March equinox, 2003.

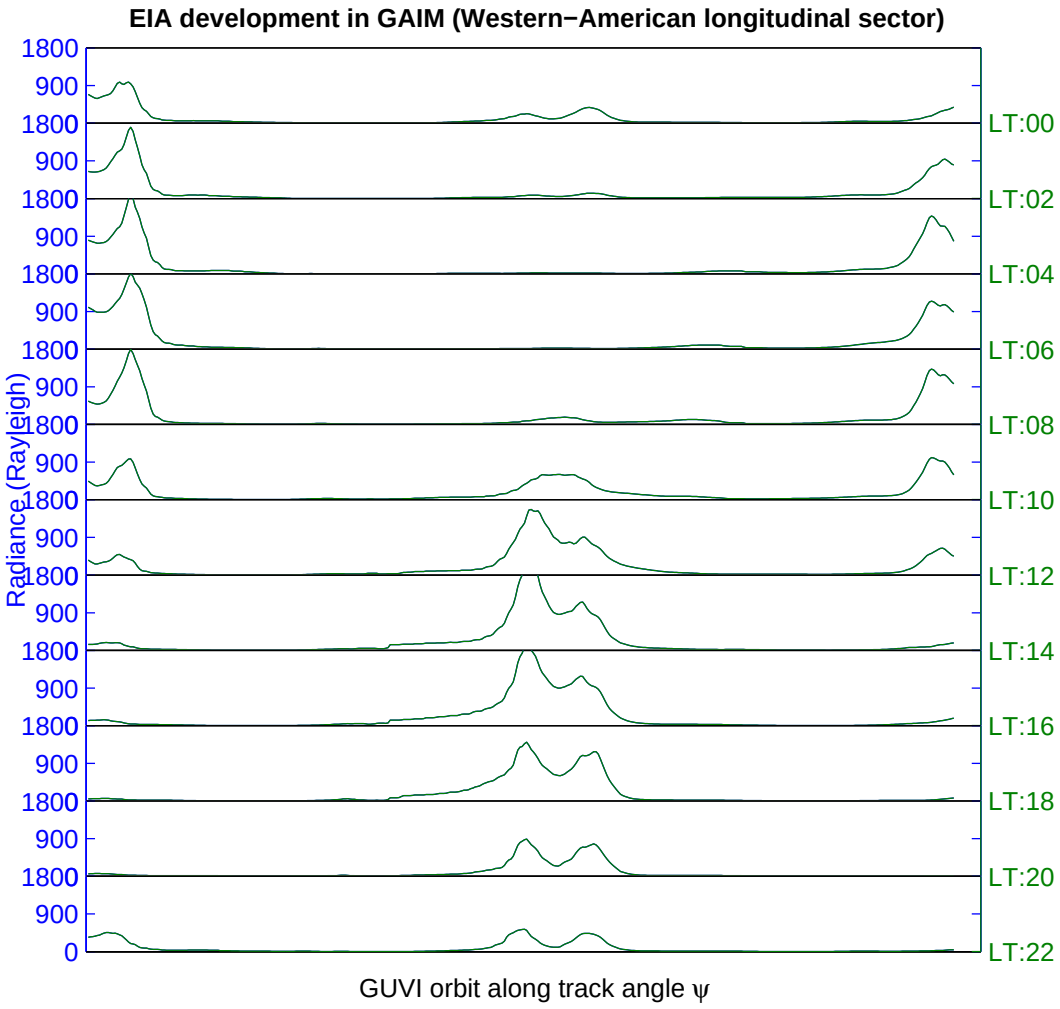

Fig. 3.12: Development of EIA with local time in GAIM at the Western-American sector (geographic longitude 210° to 300°) during March equinox, 2003.

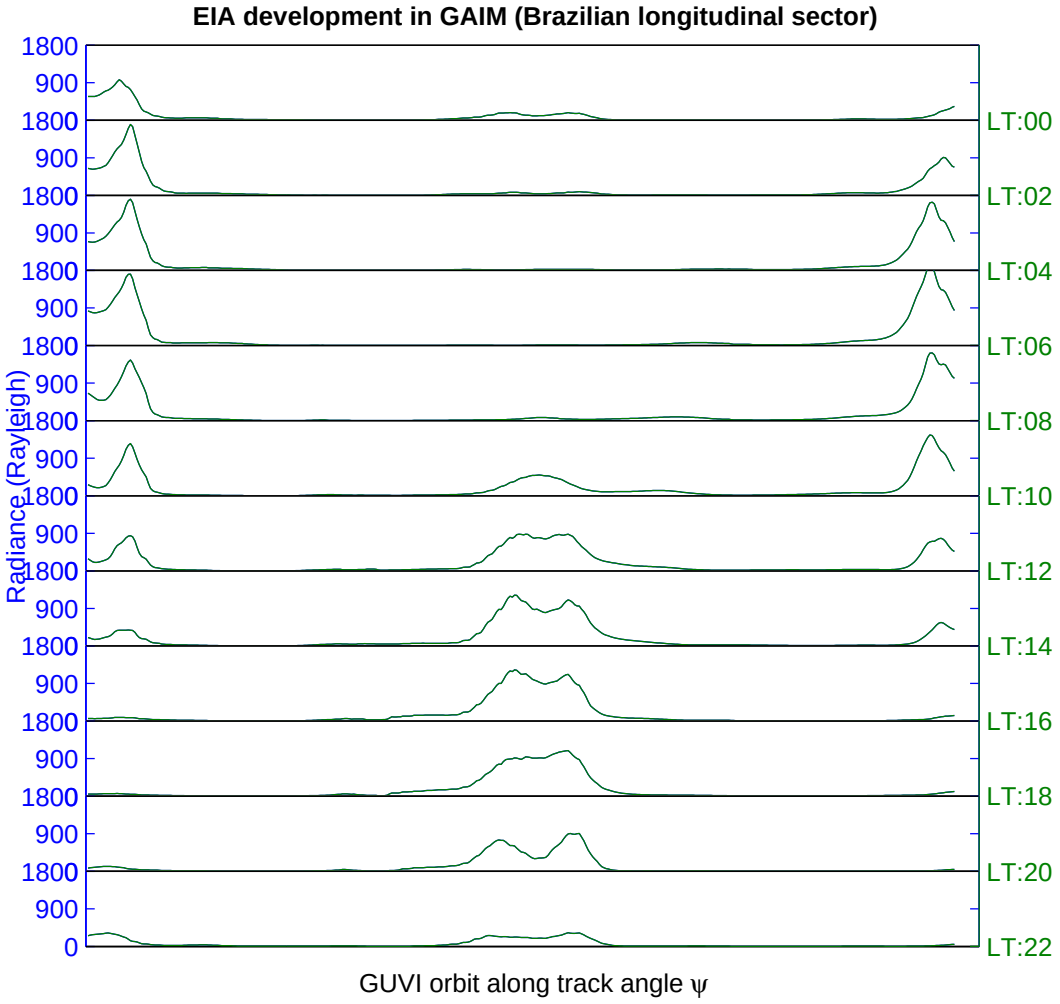

Fig. 3.13: Development of EIA with local time in GAIM at the Brazilian sector (geographic longitudes 300° to 360°) during March equinox, 2003.

Chapter 4

Observations with GUVI Limb Data

The EIA structure shows some predictable characteristics with local time and seasons. However, there is a lot of day-to-day variability between the structures even with little variation in seasons or solar fluxes. To characterize all the available GUVI data and to draw any meaningful inferences from them, it is necessary to study the overall EIA morphology using statistical methods. Many of the methods employed and presented in this chapter have been inspired from the work of Sid Henderson [3] who did a morphological study of the night side quiet time EIA using GUVI disk data. This chapter describes the study of a few characteristic features from GUVI limb 1356 Å radiance profiles to understand the EIA development at all local times of the day under quiet geomagnetic conditions. Observations of the EIA morphology at different longitudinal sectors, seasons and solar activity periods are discussed.

4.1 EIA Parameters

This section identifies the metrics that are characteristic of the EIA structure and are used in this study. In order to reduce the uncertainty in the measurements and increase the signal to noise ratio, radiance values over 14 along track pixels are averaged for every scan. The geolocation coordinates for every scan is taken from the center, (7th), of the 14 along track pixels. Signatures from stars and glints have been subtracted from the limb files used in this study as explained in Chapter 2. However, dayglow emissions have not been subtracted from this data. Hence, to avoid the low altitude dayglow emissions, radiances for the higher altitude pixels, pixel 1 to 15, are averaged for this study. This corresponds to an altitude range of 380 to 500 km.

The typical structure of a well formed EIA is shown as a function of magnetic latitude

Table 4.1: Parameters extracted from the EIA structure.

EIA structure	Magnitude	Magnetic latitude	Percentage of occurrence
Symmetric	C_M^N, C_M^S, C_M^C	C_L^N, C_L^S, C_L^C	both C^N and C^S
Asymmetric	C_M^A	C_L^A	C^A North C^A South

in fig. 4.1 (left). It consists of two well developed radiance peaks either side of the magnetic equator and a trough at the magnetic equator. For the purpose of this study, this structure is termed as a symmetric EIA structure. The magnitude and the magnetic latitude of the north crest (C_M^N and C_L^N) and south crest (C_M^S and C_L^S) and the trough (C_M^C and C_L^C) are extracted. To account for the cases when the EIA structure is not symmetric and displays only a single distinct peak, its peak radiance (C_M^A) and magnetic latitude (C_L^A) are noted. EIA formations of this kind are termed as asymmetric EIA structures and their morphology is studied separately. The percentage of occurrence of symmetric EIA (when both C^N and C^S are found) and asymmetric structures (when only one crest, i.e. C^A is found) has been tabulated. Table 4.1 summarizes the different parameters extracted for symmetric and asymmetric EIA structures.

4.2 GUVI Limb Data Classification

An index of all the available GUVI limb data was created based on longitude, local time (LT), year and seasons. The data is categorized into three seasons, June solstice, December solstice and the equinoxes. Based on the alignment of the magnetic equator with the geographic equator, four geographic longitudinal sectors were chosen. They are the African-Indian sector ($\leq 150°$), Pacific sector ($> 150°$ and $\leq 210°$), Western-American sector ($> 210°$ and $\leq 300°$), and Brazilian sector ($> 300°$ and $\leq 360°$). This longitudinal classification was selected to make the observations in this study comparable with the analysis of night time EIA done by Henderson [3].

Data is indexed along with hourly DsT, daily and 81 day average of solar flux given by

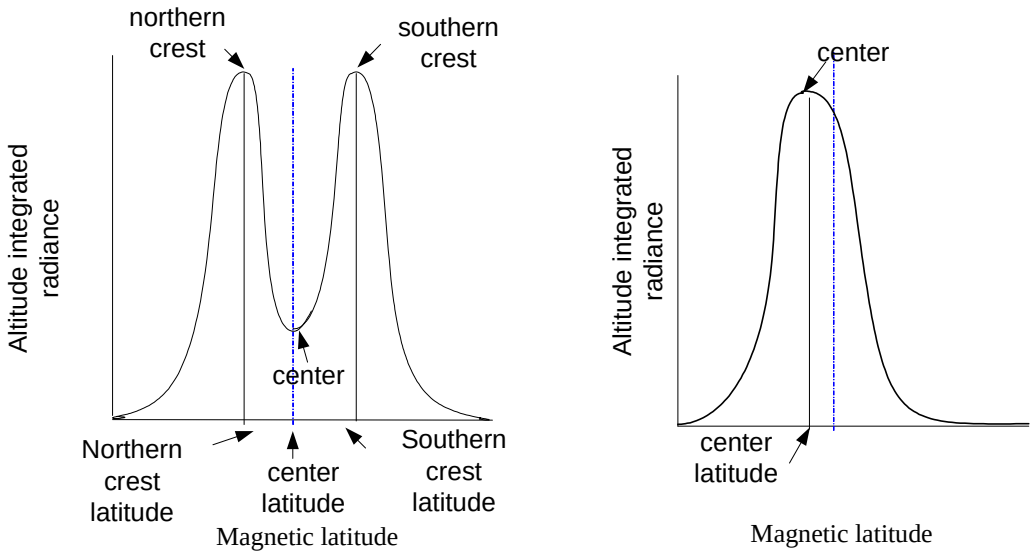

Fig. 4.1: Metrics drawn from a typical structure for (left) a well formed EIA (right) a single-peaked EIA.

F10.7. The current solar cycle was at its peak in year 2002, and hence data from year 2002 and 2003 correspond to a high solar flux period and the succeeding years correspond to the descending phase of the solar cycle. However, the daily F10.7 values vary considerably for the data files selected in a given year. This analysis is done only for geomagnetic quiet time data. Since DsT index shows variation of the geomagnetic activity over an hour which is comparable to the time period of one GUVI orbit, it can be used to filter out data into quiet and disturbed times. To select geomagnetic quiet time data, limb files corresponding to an hourly DsT index $> -50\ nT$ are chosen. Data is classified into a certain longitudinal sector and local time bin based on the geographic longitude and local time at the descending node magnetic equator of the orbit.

Symmetric and asymmetric EIA structures are identified from data files thus selected for any given combination of conditions. Parameters extracted from these files are then averaged over each group. The averaged metric is computed for a given LT only if a minimum of 1% of the total number of data samples are obtained for a given classification. This ensures that the averaged metric is a good enough representation of the entire population. Error bars are computed for each averaged metric using standard error of the mean σ_M.

$$\sigma_M = \frac{\sigma}{\sqrt{n}}, \tag{4.1}$$

where σ is the standard deviation for n samples. Since GUVI makes six global time passes over a year, we have sufficient data samples at all local times except between 1100 to 1200 hours LT when sufficient data samples are not obtained due to yaw maneuver of the TIMED spacecraft. The averaged metrics are not computed for these local times.

4.3 EIA Variability with Local Time

GUVI data from year 2003-2007 has been used to study the EIA morphology. Years 2002 and 2003 correspond to high solar activity periods but are very geomagnetically disturbed. Data from year 2004 provides more data samples because it was geomagnetically quieter, and hence gives a better opportunity to study the dependence of EIA morphology on seasons and longitudes. Figures 4.2 and 4.3 show the features of the quiet time symmetric and asymmetric EIA found at all local times for year 2004. In these observations any variation due to longitude, daily solar flux changes or seasons become averaged out.

Symmetric EIA structures are found in less than 1% of the available data samples at local times between 0100 to 0400 hours, and hence the averaged metrics are not shown for these LT bins. Figure 4.2 shows that the trough occurs at the magnetic equator and the north and south crests occur at around $\pm 15^\circ$ magnetic latitudes approximately. The separation between C_L^N and C_L^S in a symmetric EIA has small variation with local time. There is some correlation between the EIA strength and the latitudinal separation between the crests. The largest crest latitude separations of 30° in magnetic latitudes are found at 1300 and 1400 hours LT which corresponds to local times of maximum EIA strength. From 1500 to 2000 hours LT the peaks move closer to around 20° apart before they separate again in the poleward direction.

The radiance profiles (fig. 4.2) of the crests and troughs show a steady variation with local time. The crest radiances gradually increase from very low values in the 0500 to 1000 hours LT to about 200 Rayleigh at 1000 hours. The crest radiance is at its peak at 1300

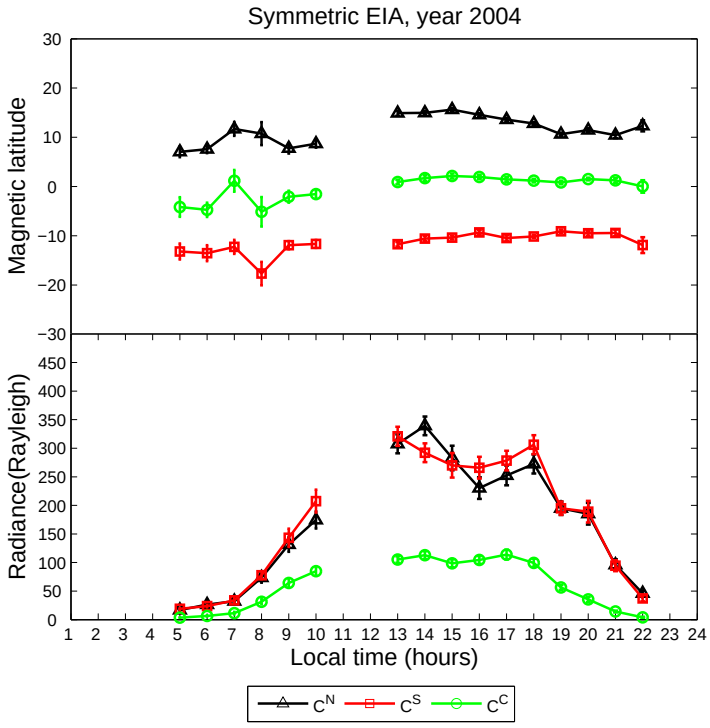

Fig. 4.2: Magnetic latitude and radiance for crests and troughs of symmetric EIA structures, year 2004.

and 1400 hours after which it starts decreasing. A relative increase in the crest magnitude occurs in the late afternoon from 1600 and 1800 hours. It can be noted that a strong signature of the prereversal drift enhancement in F-region vertical drifts that occurs at sunset does not appear in limb data from year 2004. The smooth fall of the crest radiance in the night LT can be observed. The north and south crests have equal magnitude and latitudinal separation from the magnetic equator at all times. It can be inferred that, in general, whenever a double crested EIA structure occurs, the north and south crests are symmetric about the magnetic equator. The trough magnitude also follows the morphology of the crests, although the crest to trough ratio varies considerably with local time.

Figure 4.3 shows the drift in magnetic latitude (top) and magnitude (middle) of the single crest with local time when asymmetric EIA structures are found. It can be observed that the latitude of the crest is bound between 5° and -8° magnetic latitudes. Its radiance profile with local time is similar to the profile of the crests in a symmetric EIA structure

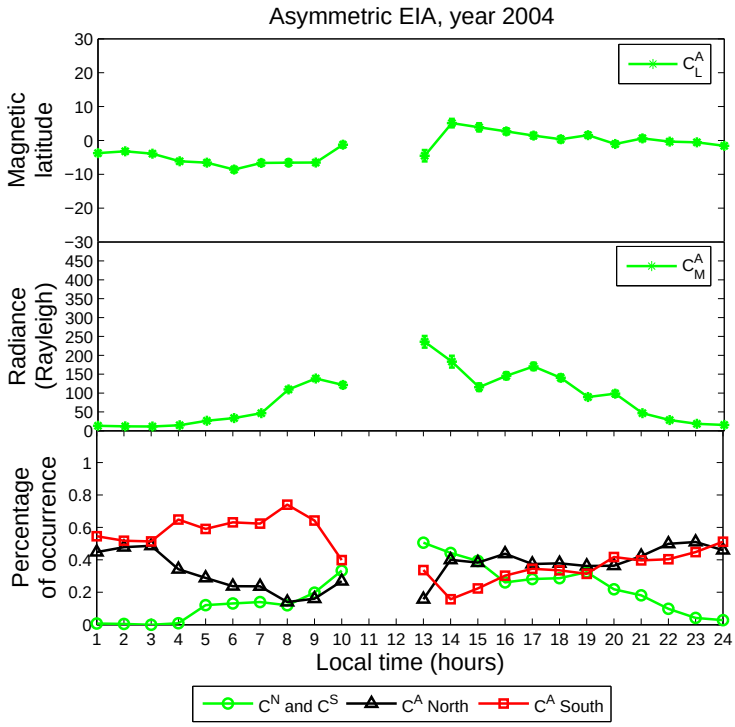

Fig. 4.3: Magnetic latitude and radiance for crests of asymmetric EIA structures and the percentage of occurrence of symmetric and asymmetric EIA structures, year 2004.

and reaches peak value at 1300 hours. It should be noted though, that a single crested EIA structure always has a far lower crest magnitude (C_M^A) than the crest radiance of a double peaked EIA structure. Figure 4.3 (bottom) shows the percentage of occurrence of symmetric and asymmetric EIA structures among the available data samples at a given LT. It can be observed that at almost all LT, the percentage of occurrence of symmetric EIA structures (both C^N and C^S occur) is much lower than the occurrence of asymmetric EIA except between LT 1300 to 1400 hours. For asymmetric EIA structures, C_L^A has been found to occur predominantly south of the magnetic equator in the morning sectors and to the north of the magnetic equator in the late evening sectors.

4.4 EIA Variability with Longitude

As described in Chapter 1, the alignment of the magnetic equator with the geographic equator plays an important role in EIA formation. As this alignment varies with longitude, it

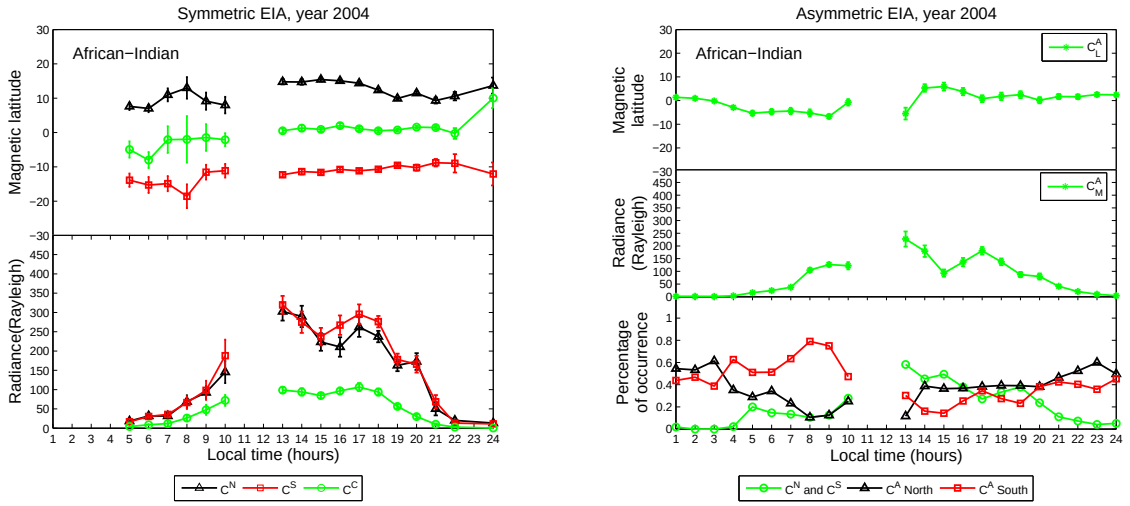

Fig. 4.4: Magnetic latitude and radiance for the EIA crests and troughs in the African-Indian sector, 2004 ($\leq 150°$).

is important to study the EIA morphology as a function of local time where each geographic longitudinal sector is observed separately. Quiet time data from all GUVI passes for year 2004 are classified into four different longitudinal bins. The metrics computed over a specific local time and longitude are averaged and studied as a function of local time. As GUVI makes 15 longitudinal passes in a single day, any seasonal difference or differences due to varying solar fluxes are implicitly averaged out in these longitudinal comparisons.

Some salient observations can be made regarding the crest magnitude (C_M) in symmetric EIA structures (figs. 4.4 to 4.7) found at different longitudinal sectors. In all the longitudinal sectors, C_M^N and C_M^S are nearly equal at all LT indicating a symmetry in the north and south crests. The crest to trough ratio varies considerably with both local time and longitudinal sector. C_M values peak at approximately 400 rayleigh at an LT of 1300 to 1500 hours and vary significantly between the longitudinal sectors for a given LT. The highest C_M values are found in the Western-American and Pacific sector and the lowest C_M values are observed in African-Indian and Brazilian sector. The number of data samples available for computing the averaged metrics vary between the different longitudinal sectors. Hence, the relatively smooth C_M profiles in the African-Indian sector is partly because there are more data samples available for the African-Indian sector owing to its

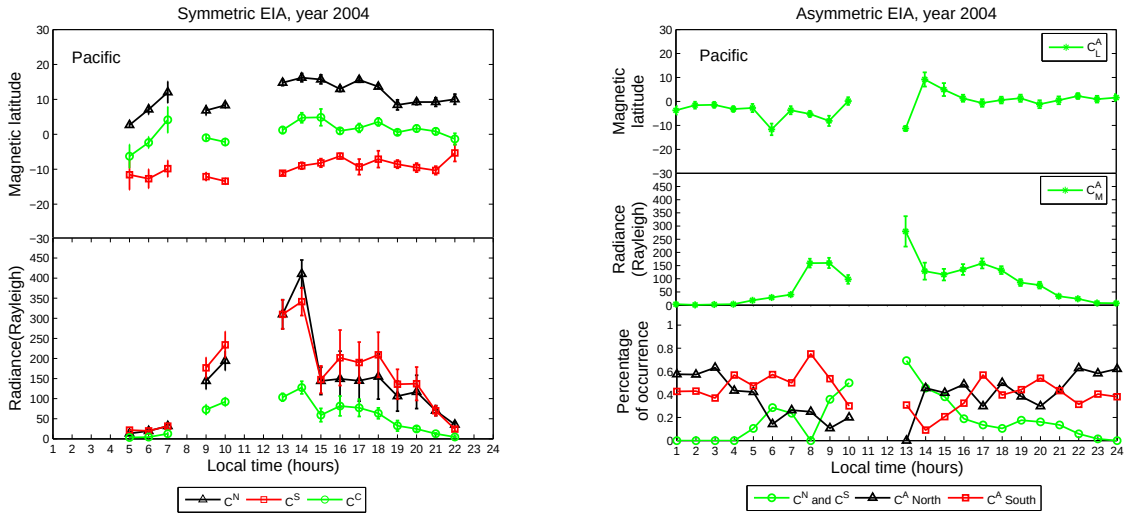

Fig. 4.5: Magnetic latitude and radiance for the EIA crests and troughs in the Pacific sector, 2004 ($> 150°$ and $\leq 210°$).

large longitudinal range (0° to 150°). The Pacific and Brazilian sectors have the lowest number of data samples available at each LT. This explains the relatively large error bars found in the C_M profiles in these two sectors.

The African-Indian and the Western-American sectors exhibit a typical EIA morphology with a peak in C_M between 1400 to 1500 hours. C_M starts to dip at around 1600 and increases again at 1800 hours. The Brazilian sector (fig. 4.7) shows the most anomalous EIA morphology and has no characteristic peak that is observed in other sectors. This can be attributed to the large difference between magnetic and geographical equator in this sector. The latitudinal separation between the crests (C_L^N and C_L^S) does not vary significantly between the different sectors. The percentage of occurrence of symmetric EIA structures is always low except in the Pacific sector where it is relatively high between 1000 to 1400 hours LT. The Western-American and Brazilian sectors have the lowest percentage of occurrence of symmetric EIA structure, although, there is an increase in symmetric EIA formation at evening LT in the Brazilian sector (fig. 4.7).

4.5 EIA Variability with Season

Quiet time data from year 2004 is used to compare the EIA morphology for three

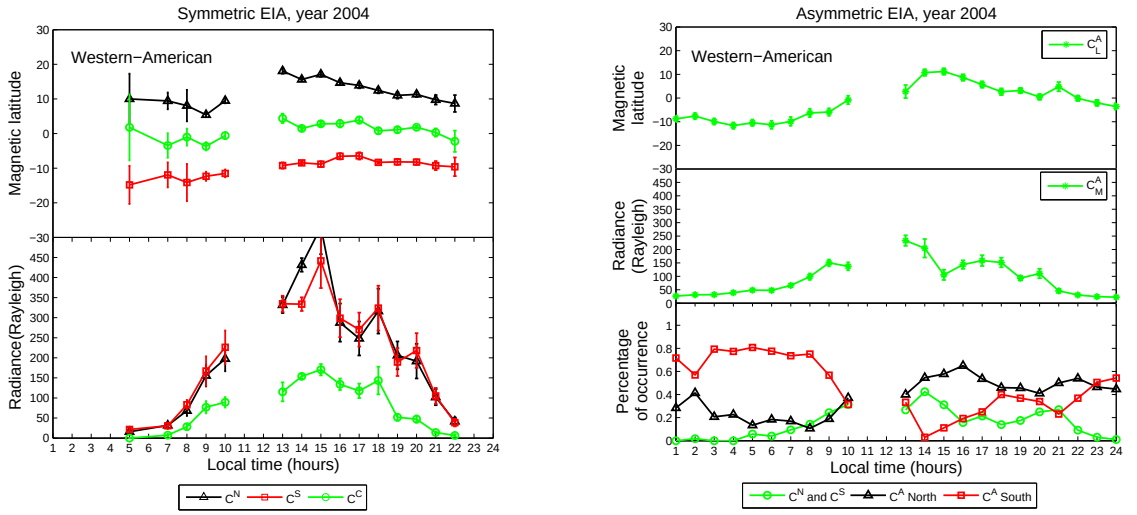

Fig. 4.6: Magnetic latitude and radiance for the EIA crests and troughs in the Western-American sector, 2004 ($> 210°$ and $\leq 300°$).

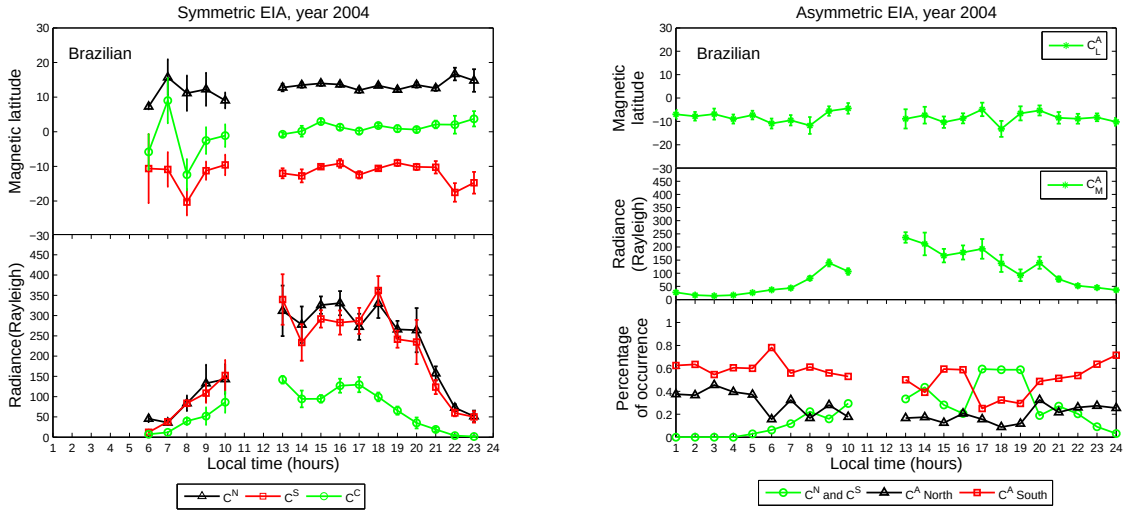

Fig. 4.7: Magnetic latitude and radiance for the EIA crests and troughs in the Brazilian sector, 2004 ($> 300°$ and $\leq 360°$).

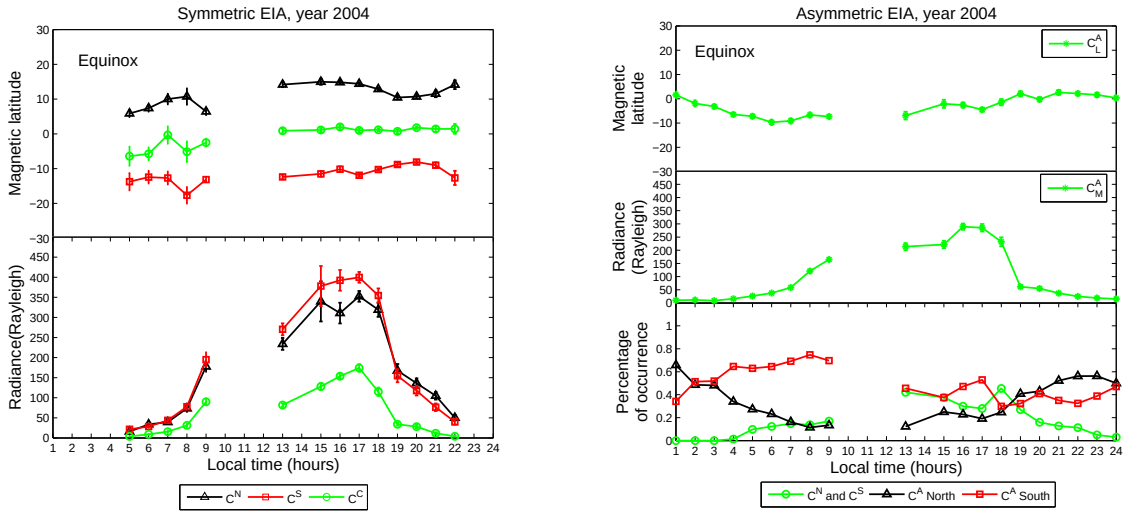

Fig. 4.8: Magnetic latitude and radiance for the EIA crests and troughs during the spring and vernal equinoxes, 2004.

seasons—equinox (March-June and September-December), June solstice (June-September) and December solstice (December-March) when the subsolar point is at the equator, northern and southern hemisphere, respectively. There is some variation in the average solar flux between the seasons. The 81-day average F10.7 is 102, 113, and 108 during equinox, June solstice and December solstice, respectively. The number of available quiet time data samples at different local times vary significantly with each season. Particularly, twice the number of data samples are available to study the equinox morphology compared to the June and December solstice. This explains the smooth C_M profiles observed during the equinox season. During December solstice there are no observations sampled until 1000 hours LT during year 2004 as can be seen from fig. 4.10.

It can be observed from figs. 4.8 to 4.10 that C_M is found to be highest during the equinox and lowest during June solstice. Equinox period shows a good correspondence between peak C_L and C_M with the maximum occurring a little later in the day between 1600-1700 hours LT. During December solstice, C_M peaks at 1400 LT and rises again in the night time between 1700 to 2000 hours LT. C_M values for asymmetric EIA structures follow a similar morphology as in the symmetric EIA structures and the lowest C_M occurs during June solstice. The percentage of occurrence of symmetric EIA is found to be lowest

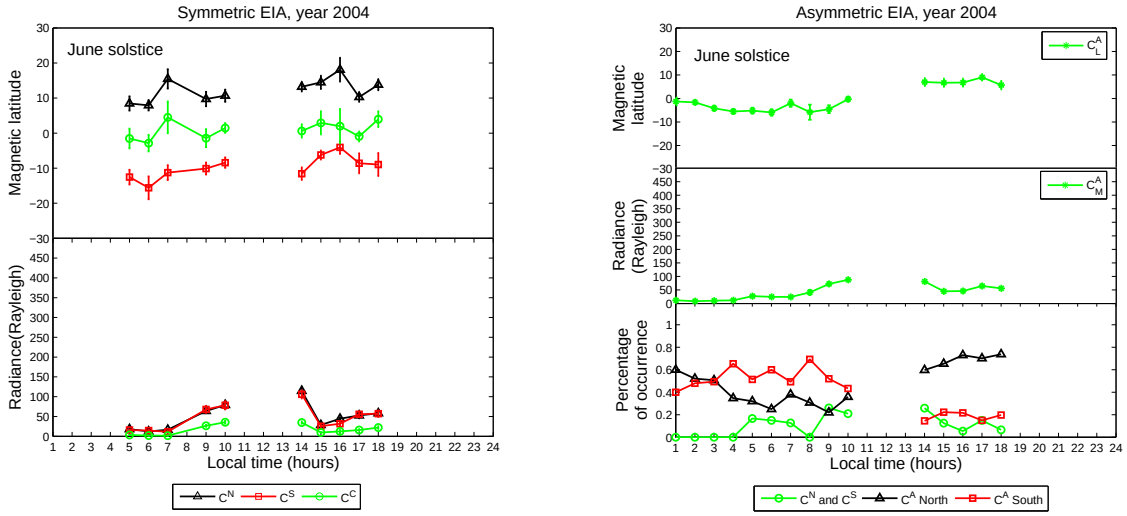

Fig. 4.9: Magnetic latitude and radiance for the EIA crests and troughs during June solstice, 2004.

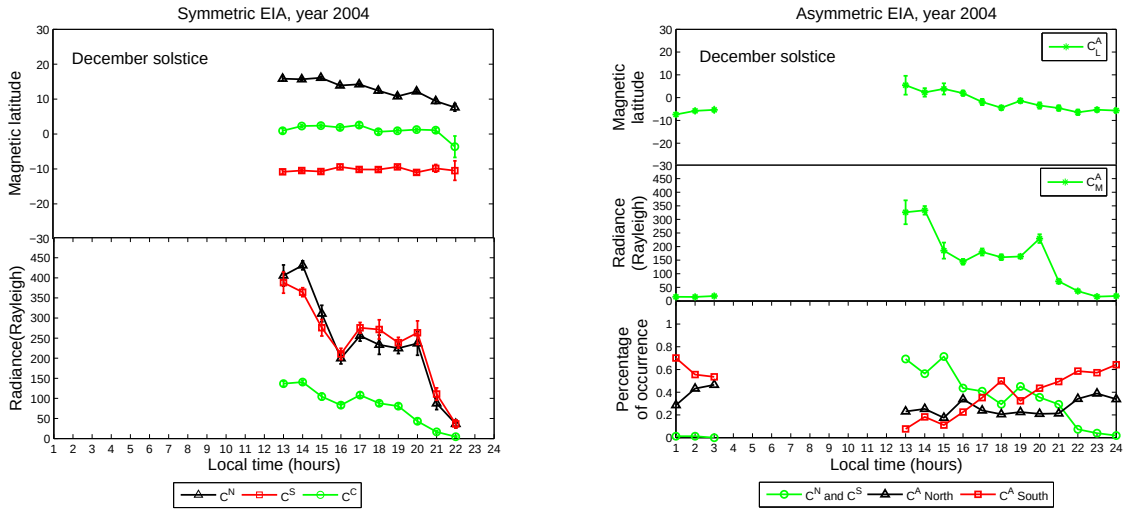

Fig. 4.10: Magnetic latitude and radiance for the EIA crests and troughs during December solstice, 2004.

during June solstice and highest during December solstice. A suppressed EIA formation during June solstice has been previously observed in night time data by Henderson [3].

4.6 EIA Variability with Solar Activity

To study the EIA variability as a function of solar flux alone, data from a decreasing solar cycle period, i.e. from year 2003 to 2005, is studied as shown in figs. 4.11 to 4.13. The average F10.7 values during year 2003, 2004, 2005 were found to be 128, 107, and 93, respectively. The corresponding peak C_M values in the symmetric EIA structures drop from 800, 400 to 200 and the peak C_M occurs at 1600, 1400 and 1300 hours LT, respectively. There is a close correlation between C_M and C_L at all local times for all the three years. A similar trend occurs in the peak C_M values found for asymmetric EIA structures. The radiance and latitude profiles as a function of local time do not vary significantly with solar activity. The percentage of occurrence of symmetric EIA is seen to be fairly constant with solar activity.

The EIA morphology as a function of longitudinal sectors and seasons is studied for years 2003 and 2005 as shown in Appendix A.

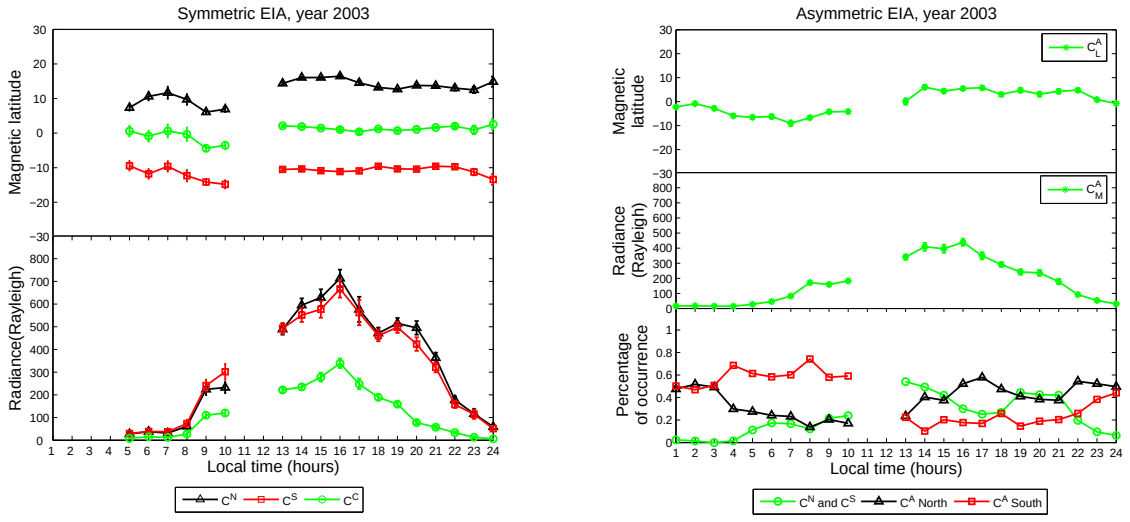

Fig. 4.11: Magnetic latitude and radiance for the EIA crests and troughs for year 2003.

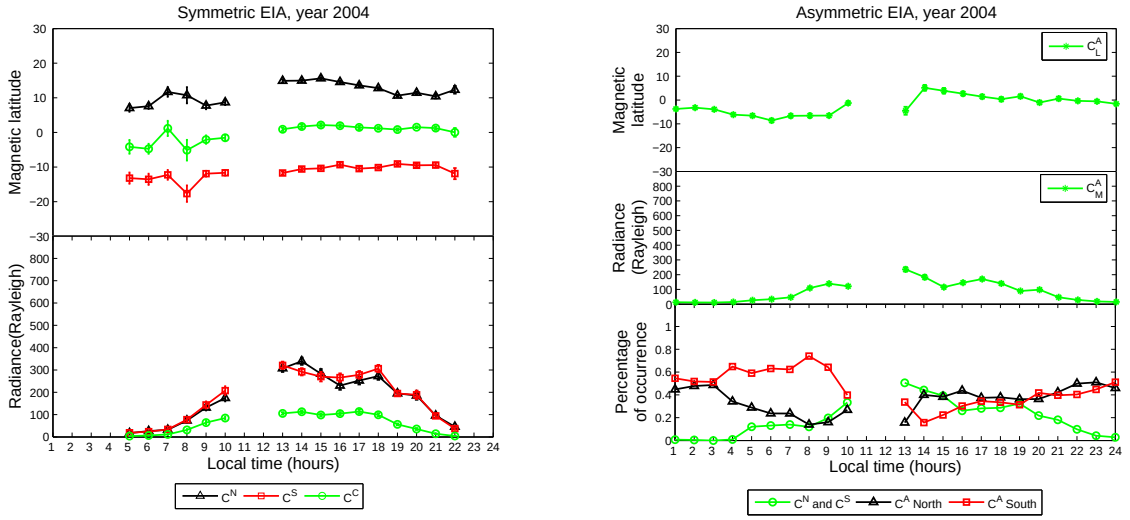

Fig. 4.12: Magnetic latitude and radiance for the EIA crests and troughs for year 2004.

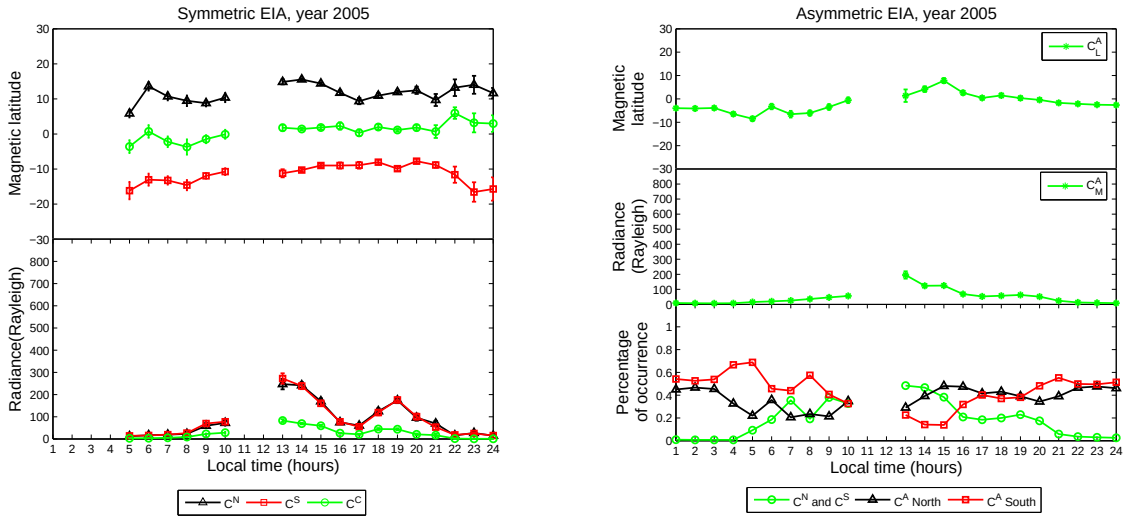

Fig. 4.13: Magnetic latitude and radiance for the EIA crests and troughs for year 2005.

Chapter 5

Summary and Future Work

5.1 Summary

This thesis presents GUVI limb observations of the EIA from the TIMED spacecraft and its global behavior. The study is valuable because very few observations of the EIA on the day side are currently available from other satellites. GUVI data is available from year 2002 to 2007 and will continue to be recorded for atleast the next four years. Hence, it should be possible to trace the EIA morphology through an entire solar cycle using GUVI data. Data reduction techniques in Chapter 2 show how EIA observations can be extracted from GUVI limb scans. With the analysis developed in Chapters 2 and 4, it is clear that the EIA shows huge variability with local time, seasons, longitude and solar activity. While most of the EIA behavior is directly related to variations in solar heating and neutral winds, the EIA morphology shows significant amount of day to day variability that is yet to be understood. A valuable contribution from this thesis work is the study of how well ionospheric models namely TIMEGCM and GAIM predict the electron densities in the EIA regions as shown in Chapter 3. A comparison of 1356 Å radiance observed from GUVI with those calculated from the models show that the 1356 Å radiance predicted from the models is higher in magnitude. However, the structure of the EIA formation and development as shown by GUVI is well represented in the models.

5.2 Future Work

Future work with GUVI limb data analysis can take multiple directions. A few possibilities that seem most useful are described in this section.

5.2.1 Binning GUVI Limb Files

In processing GUVI limb data, along track pixels in successive scans are stacked alongside and viewed as a function of altitude. As explained in Chapter 2, the 14 along track pixels are averaged for every scan to improve the effective signal count rate. However, there is a significant amount of overlap in pixels of successive scans. For instance, at a tangent point observation 152 km in altitude (30^{th} across track pixel) at a range of 2530 km, the GUVI FOV footprint covers a distance of 530 km. But with a spacecraft speed of 7 km/s and with a 15 second scan duration, the spacecraft moves at a distance of 105 km between one limb scan to next. This would mean that each 30^{th} across track pixel gets resampled in five consecutive limb scans or four-fifth of every limb scan overlaps with the adjacent scan (fig. 5.1). FOV range decreases at higher tangent point altitudes and so the overlap between scans decreases at higher altitudes due to a smaller FOV footprint.

Higher accuracy is achieved if the corresponding overlapping pixels in successive scans are averaged (fig. 5.2) instead of averaging all along track pixels in a scan. The overlap is determined for every across track angle and radiances are averaged across the overlapping pixels. The re-gridded limb file has different number of pixels of varying resolution at each tangent point altitude. The higher resolution pixels at higher altitudes are co-added to get uniform pixel resolution at all across track angles. Figure 5.3 compares between

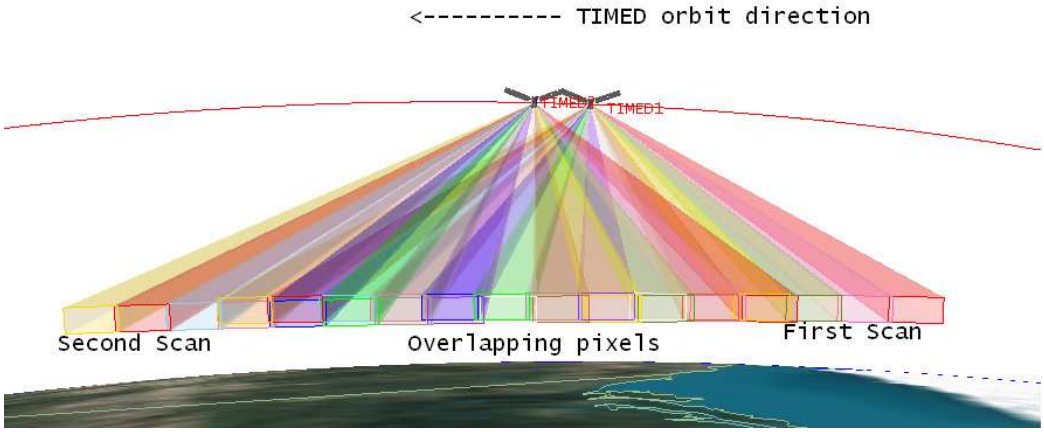

Fig. 5.1: Overlap in successive limb scans at tangent point altitude of 152 km.

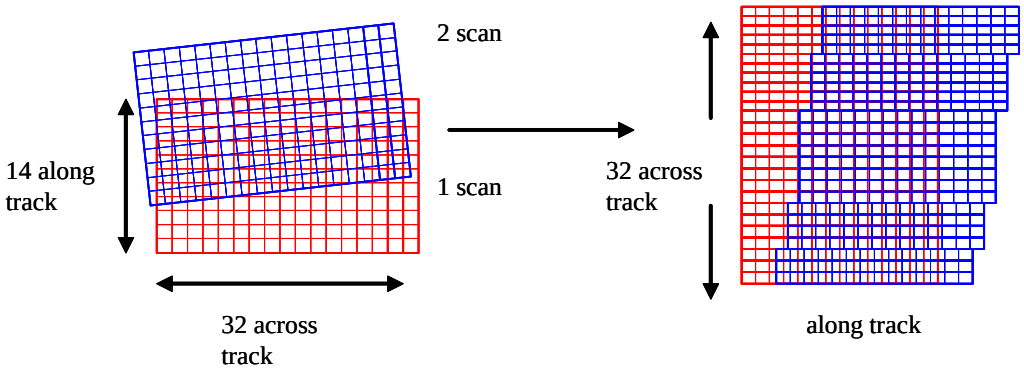

Fig. 5.2: Overlapping pixels at corresponding across track angles in successive limb scans are averaged.

radiance profiles obtained from re-gridding and along-track averaging. The signal-to-noise ratio achieved with both techniques is almost same. It can be observed that re-gridding may not provide any extra information, particularly in the spatial scales that we are interested in for this study.

Further, because the limb scans are arranged circularly in one GUVI orbit, pixels at corresponding across track angles in successive scans do not align perfectly with altitude. For more accurate spatial observation, the limb file must be binned into a uniform spatial resolution in spherical coordinates and radiances at each of the coordinates must be determined by co-adding overlapping pixels. This approach has not been explored here, as this study does not require such detailed spatial scales. However, similar data processing methods may be required if a highly detailed spatial observation is desired with GUVI limb data.

5.2.2 Dayglow Subtraction Using Neutral Density Profiles

As explained in Chapter 1, low altitude day glow emissions is due to photo-electron impact ionization of the neutrals and so the radiance is a function of neutral densities. Using an inversion method, the neutral density profiles has been obtained from GUVI observed radiances by Robert Meier [19]. The day glow emissions are predicted from these neutral density profiles for individual orbits. This data is available for download as a set of GUVI

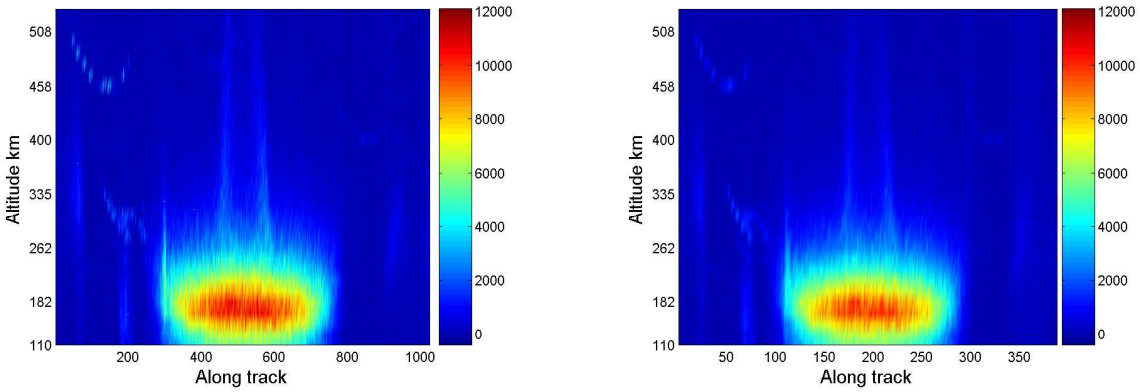

Fig. 5.3: Rebinned 1356 Å radiance (left) and along track averaged 1356 Å radiance (right) for a GUVI limb file.

L2B files in the GUVI home page [11]. The emissions are computed only for the lower altitudes in a range of 100 to 350 km and for a few low solar zenith angles (SZA). By extrapolating data to higher altitudes and other solar zenith angles, a day glow surface is obtained which can be subtracted from GUVI 1356 Å radiances to extract EIA signatures. This method is similar to subtraction technique explained in Chapter 2, the difference being that the surface to subtract is obtained from computed neutral densities instead of using GUVI 1356 Å low altitude radiance fits. The dayglow profiles are available down to low altitudes, hence a cleaner EIA subtraction is obtained at the low altitudes compared to the subtraction results shown in Chapter 2. As in Chapter 2, dayglow radiances are projected to higher altitudes, from 350 to 500 km, using an exponential fit in a least square sense.

$$I = I_0 e^{-\frac{x}{H}}, \tag{5.1}$$

$$\log I = \log I_0 - \frac{x}{H}, \tag{5.2}$$

where x is altitude. The top side scale height of the exponential, H and the peak radiance, I_0 are obtained using method of pseudo-inverses. These exponentials are fit along track assuming a cosine dependence on SZA given by

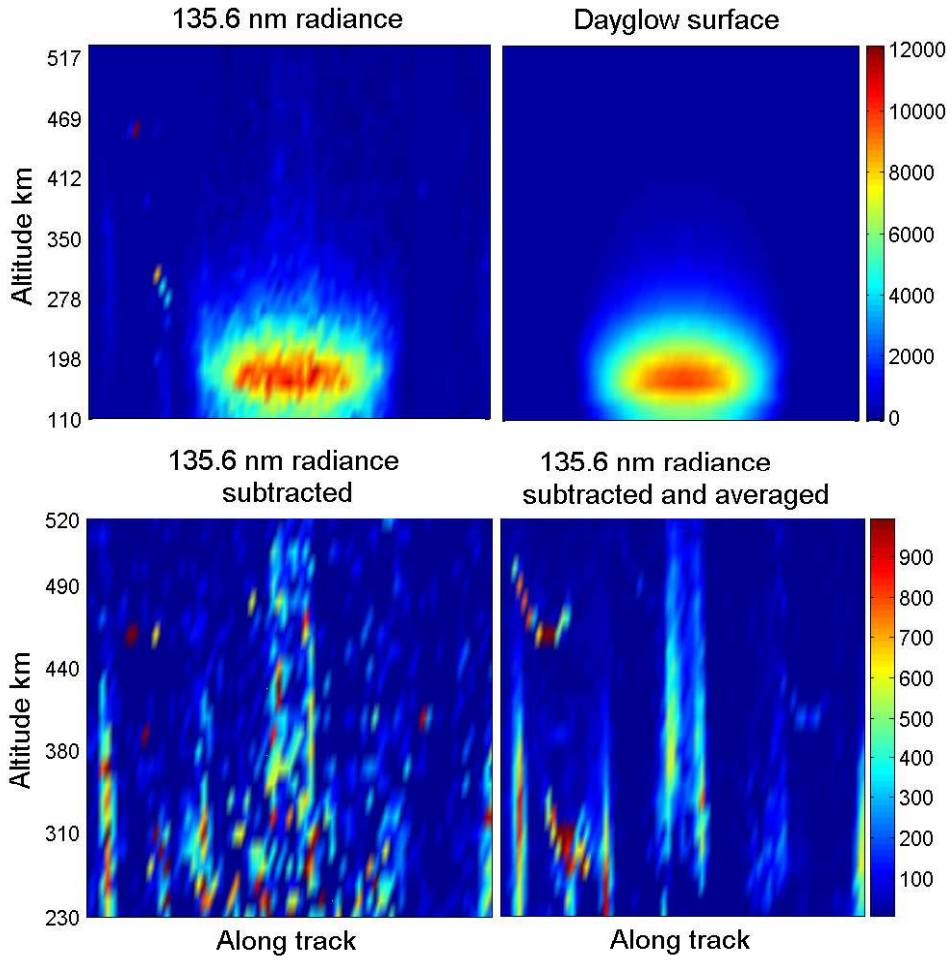

Fig. 5.4: Subtraction of dayglow emissions from 1356 Å radiance data using neutral density profiles.

$$\log I_{dayglow} = \alpha_1 \cos(\alpha_2(SZA_{lat} - SZA_{SSP} - \alpha_3)), \tag{5.3}$$

where SZA_{lat} is the SZA at each along track angle and SZA_{SSP} is the minimum SZA in the orbit. The coefficients α_1, α_2 and α_3 are determined using least squares curve fitting. Some results of this subtraction are shown in fig. 5.4.

The subtracted surface has a poor signal-to-noise ratio due to the nature of averaging performed on original GUVI radiance and the day glow fit. So the subtracted data is spatially smoothed using a gaussian filter. The disadvantage with this subtraction process

is that the day glow emissions are not available for all orbits - particularly the dawn to dusk orbits that have high solar zenith angles throughout. Also, for orbits with large SZA, dayglow radiance cannot be well approximated by a cosine function of SZA. A suggested alternative approach is to consider the day glow emission as a function of SZA to behave as a reciprocal of Chapman function [20].

5.2.3 Longitudinal Variation in Day Time EIA Morphology

Immel et al. [14] have shown the existence of a longitudinal wave number 4 pattern in Equatorial Electro Jet (EEJ) currents which can be attributed to a longitudinal variation in the fountain strength and E-region electric fields. This is believed to be caused by non-migrating diurnal atmospheric tides in the E-region. FUV observations of the post-sunset EIA from GUVI and IMAGE show [21] a similar longitudinal modulation due to E-region atmospheric tides in the F-region peak ion densities. This was observed during 20:30 to 21:30 LT at solar maximum equinoctial periods. Such a pattern in the day side is yet to be established. Exploring day time GUVI limb data as a function of longitude using statistical methods as done in Chapter 4 may help us observe if such a longitudinal wave pattern fixed in local time exists in the day time EIA morphology (fig. 5.5).

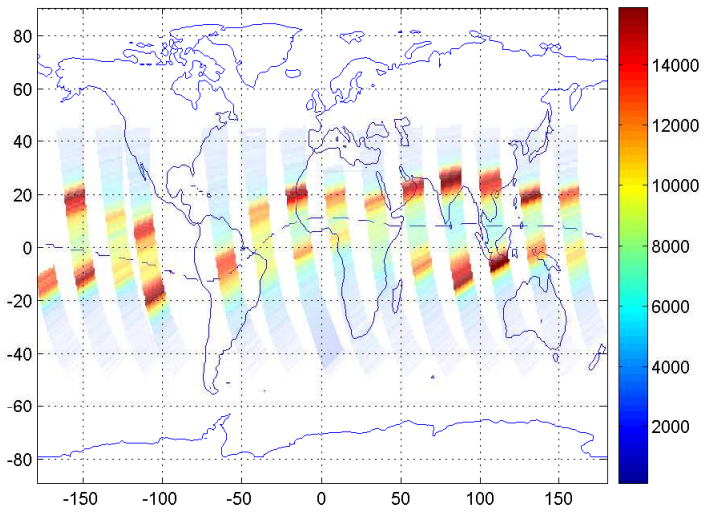

Fig. 5.5: Longitudinal variation in 1356 Å radiance from GUVI limb scans integrated over an altitude range 350 to 500 km at 15:00 hours LT, equinox 2003.

In many ways, this thesis work is a bare start to different kinds of data analysis that can be done with GUVI limb files. It is clear that the data is consistent and very valuable for studying the day time EIA morphology. This analysis has opened up many avenues for future work and we encourage someone to follow on with this study.

References

[1] T. F. Tascoine, *Introduction to the Space Environment.* Malabar, FL: Kreiger Publishing Company, 1971.

[2] W. Baumjohann and R. A. Treumann, *Basic Space Plasma Physics.* London, UK: Imperial College Press, 2004.

[3] S. B. Henderson, *Global characterization of the equatorial anomaly with GUVI data.* Ph.D. dissertation, Utah State University, Logan, 2005.

[4] H. Luhr and S. Maus, "Direct Observation of the F-region dynamo currents and the spatial structure of the EEJ by CHAMP," *Geophysical Research Letters*, vol. 33, pp. 1–6, 2006.

[5] R. H, "The F-layer Dynamo," *planspcsci*, vol. 19, pp. 263–267, 1971.

[6] J. J. Sojka and R. W. Schunk, "A theoretical study of the global F-region for June Solstice, Solar Maximum and Low Magnetic Activity," *Journal of Geophysical Research*, vol. 90(A6), p. 5286, 1985.

[7] R. R. Meier, "Ultraviolet spectroscopy and remote sensing of the upper atmosphere," *Space Science Reviews*, vol. 58, pp. 1–185, 1991.

[8] R. G. Roble, "The NCAR Thermosphere-Ionosphere-Mesosphere-Electrodynamics General Circulation Model (TIMEGCM)," in *Methods in Computational Physics*, ser. Solar-terrestrial Energy Program:Handbook of Ionospheric Models, R. W. Schunk, Ed., 1996, pp. 281–288.

[9] W. M. Washington and D. L. Williamson, "A description of the NCAR global circulation models," in *Methods in Computational Physics*, ser. General Circulation Models of the Atmosphere, J.Chang, Ed. Academic Press, 1977, vol. 17, pp. 111–172.

[10] D. Y. Kusnierkiewicz, "Overview of the TIMED spacecraft," *The Johns Hopkins University APL Technical Digest*, vol. 24, pp. 150–155, 2003.

[11] The Johns Hopkins University Applied Physics Laboratory, "GUVI Global Ultraviolet Imager, Introduction," [http://guvi.jhuapl.edu].

[12] A. B. Christensen, L. J. Paxton, S. Avery, J. Craven, G. Crowley, D. C. Humm, H. Kil, R. R. Meier, C. I. Meng, D. Morrison, D. Morrison, B. S. Ogorzalek, P. Straus, D. J. Strickland, R. M. Swenson, R. L. Walterscheid, B. Wolven, and Y. Zhang, "Initial observations with the Global Ultraviolet Imager (GUVI) in the NASA TIMED satellite mission," *Journal of Geophysical Research*, vol. 108, no. A12, pp. 1451–1467, 2003.

[13] A. L. Newman, A. B. Christensen, and D. E. J. Anderson, "Calculated and observed limb profiles of OI 1356 Å dayglow," *Journal of Geophysical Research*, vol. 88, pp. 9265–9270, 1983.

[14] S. L. England, T. J. Immel, E. Sagawa, S. B. Henderson, M. E. Hagan, S. B. Mende, H. U. Frey, C. M. Swenson, and L. J. Paxton, "Effect of atmospheric tides on the morphology of the quiet time, postsunset equatorial ionospheric anomaly," *Journal of Geophysical Research*, vol. 111, no. A10S19, 2006.

[15] R. DeMajistre, L. J. Paxton, D. Morrison, J. H. Yee, L. P. Gonchorenko, and A. B. Christensen, "Retrievals of nighttime electron density from Thermosphere Ionosphere Mesosphere Energetics and Dynamics (TIMED) mission Global Ultraviolet Imager (GUVI) measurements," *Journal of Geophysical Research*, vol. 109, no. A05305, 2004.

[16] C. L. Wyatt, *Radiometric System Design.* New York: Macmillan Publishing Company, 1987.

[17] D. J. Melendez, R. R. Meier, and J. M. Picone, "Analysis of the oxygen nightglow measured by Hopkins Ultraviolet Telescope: Implications for ionospheric partial radiative recombination rate coefficients," *Journal of Geophysical Research*, vol. 104, no. A7, pp. 14 901–14 903, 1999.

[18] F. O. Bartell, "Projected solid angle and blackbody simulators," *Applied Optics*, vol. 28, no. 6, pp. 1055–1057, 1989.

[19] R. R. Meier and J. M. Picone, "Retrieval of absolute thermospheric concentrations from the far UV dayglow: An application of discrete inverse theory," *Journal of Geophysical Research*, vol. 99, no. A4, pp. 6307–6320, 1994.

[20] D. K. Prinz and R. R. Meier, "Ogo-4 Observations of the Lyman-Birge-Hopfield Emission in the Day Airglow," *Journal of Geophysical Research*, vol. 76, no. 25, pp. 6147–6157, 1971.

[21] S. L. England, S. Maus, T. J. Immel, and S. B. Mende, "Longitudinal variation of the E-region electric fields caused by atmospheric tides," *Geophysical Research Letters*, vol. 33, no. L21105, 2006.

Appendices

Appendix A

EIA Morphology for Years 2003 and 2005

In Chapter 4, EIA morphology with seasons with longitude is presented for quiet time data from year 2004 alone. In this section, morphology of quiet time EIA for year 2003 (high solar flux period) and 2005 (low solar flux period) are shown.

A.1 Longitudinal Variation in 2003

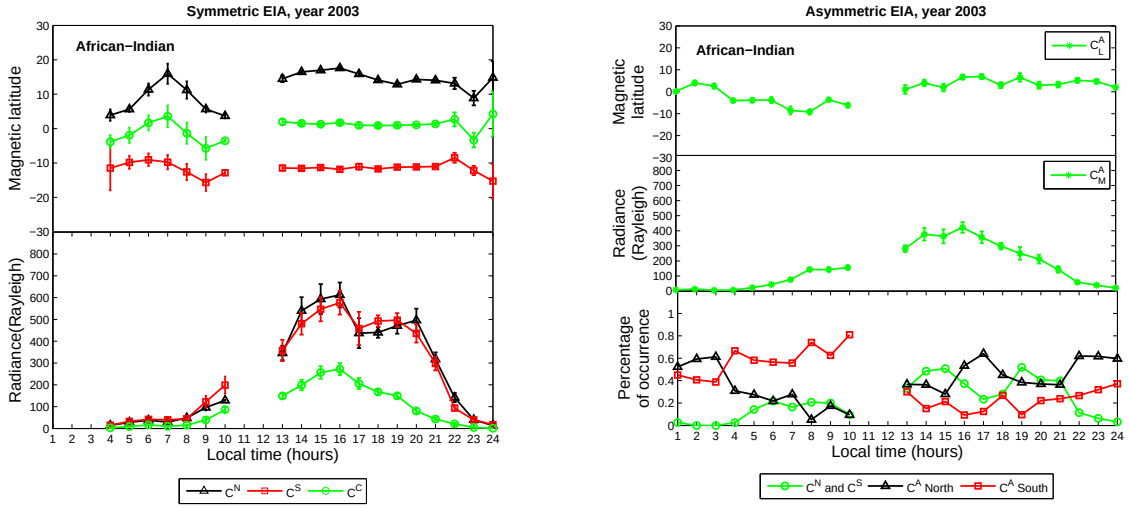

Fig. A.1: Magnetic latitude and radiance for the EIA crests and troughs in the African-Indian sector, 2003 ($\leq 150°$).

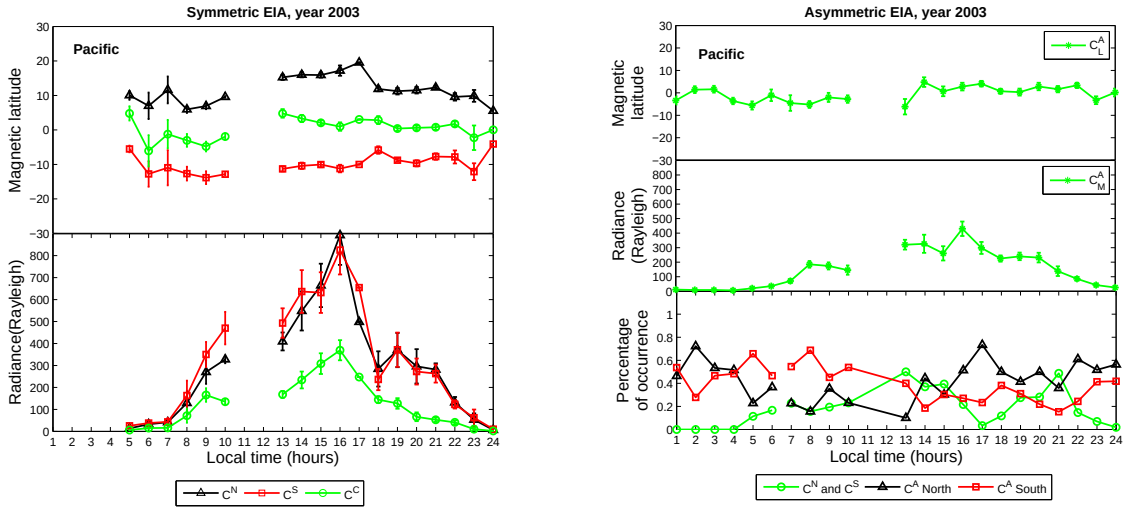

Fig. A.2: Magnetic latitude and radiance for the EIA crests and troughs in the Pacific sector, 2003 ($> 150°$ and $\leq 210°$).

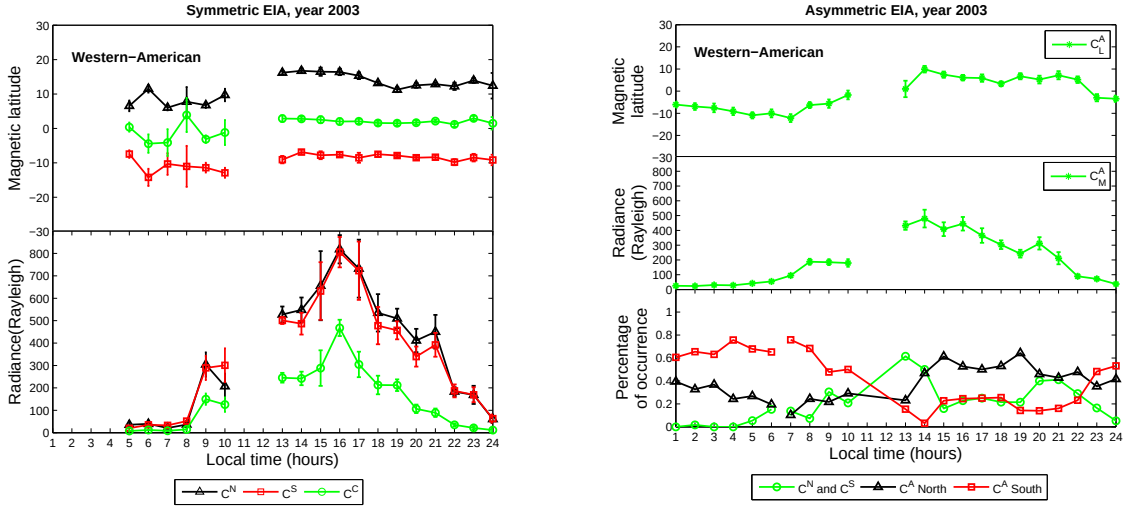

Fig. A.3: Magnetic latitude and radiance for the EIA crests and troughs in the Western-American sector, 2003 ($> 210°$ and $\leq 300°$).

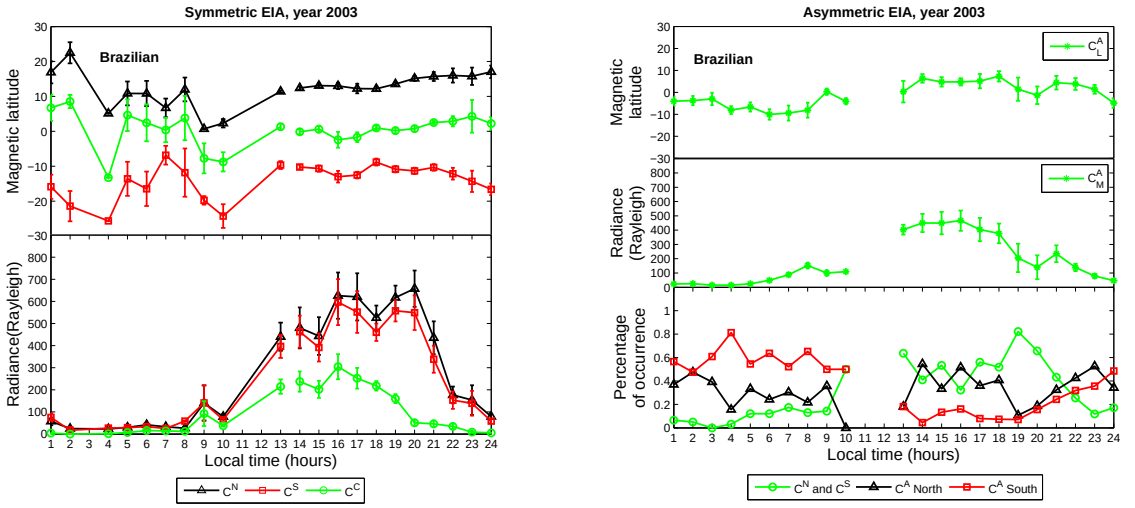

Fig. A.4: Magnetic latitude and radiance for the EIA crests and troughs in the Brazilian sector, 2003 ($> 300°$ and $\leq 360°$).

A.2 Seasonal Variation in 2003

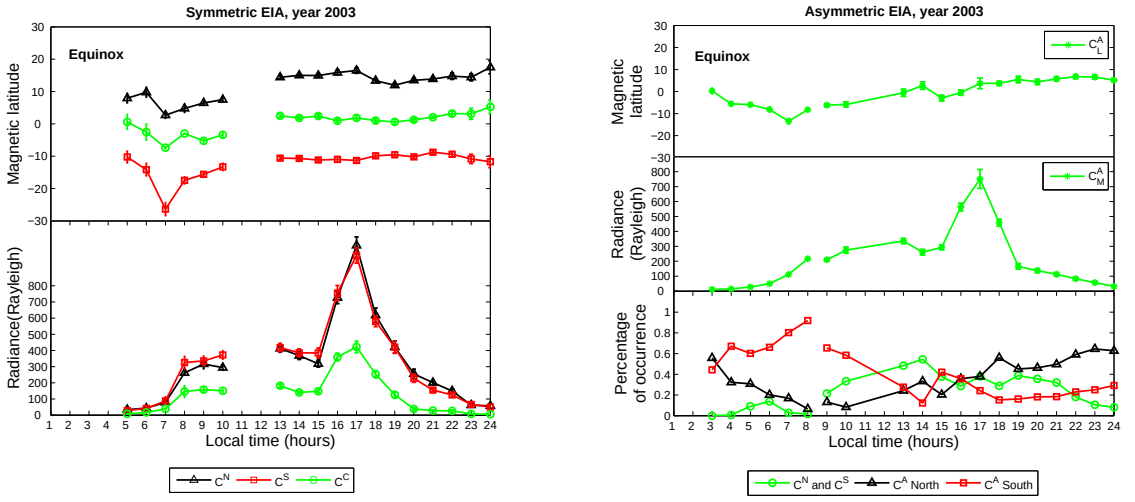

Fig. A.5: Magnetic latitude and radiance for the EIA crests and troughs during the spring and vernal equinoxes, 2003.

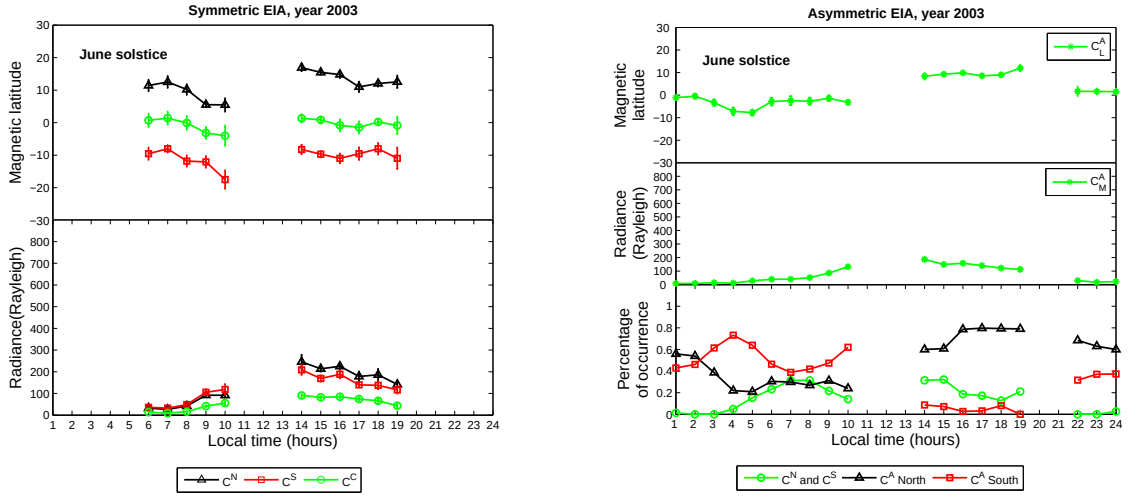

Fig. A.6: Magnetic latitude and radiance for the EIA crests and troughs during June solstice, 2003.

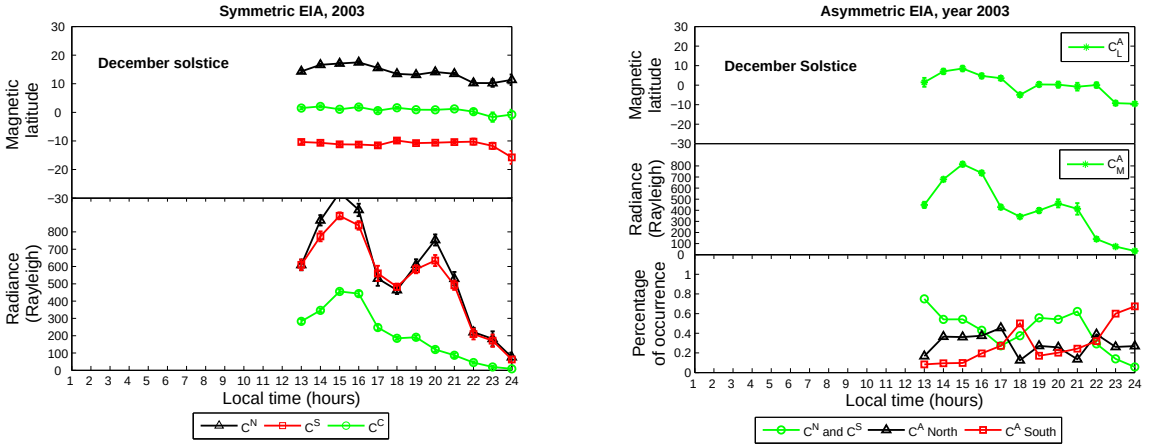

Fig. A.7: Magnetic latitude and radiance for the EIA crests and troughs during December solstice, 2003.

A.3 Longitudinal Variation in 2005

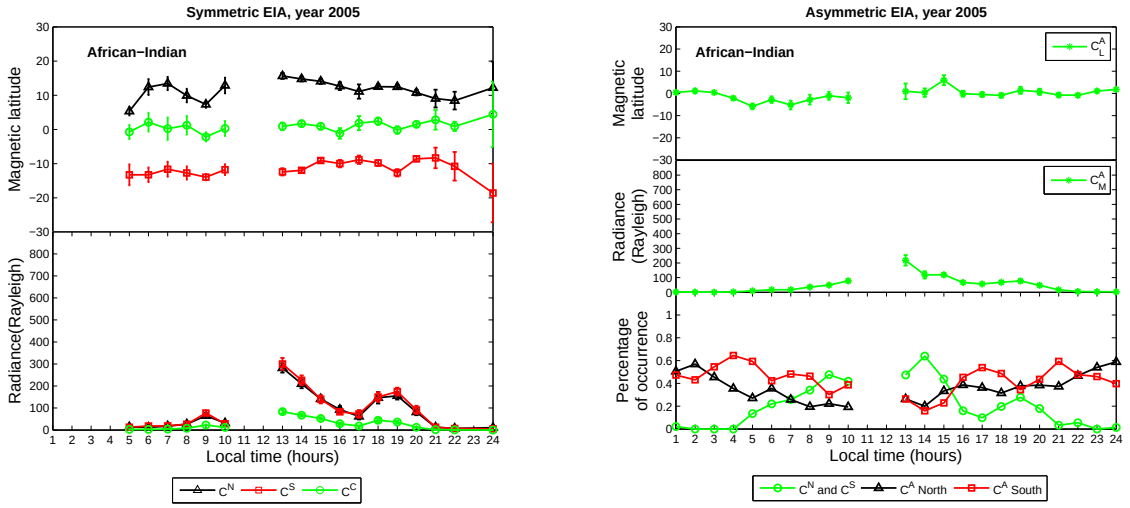

Fig. A.8: Magnetic latitude and radiance for the EIA crests and troughs in the African-Indian sector, 2005 ($\leq 150°$).

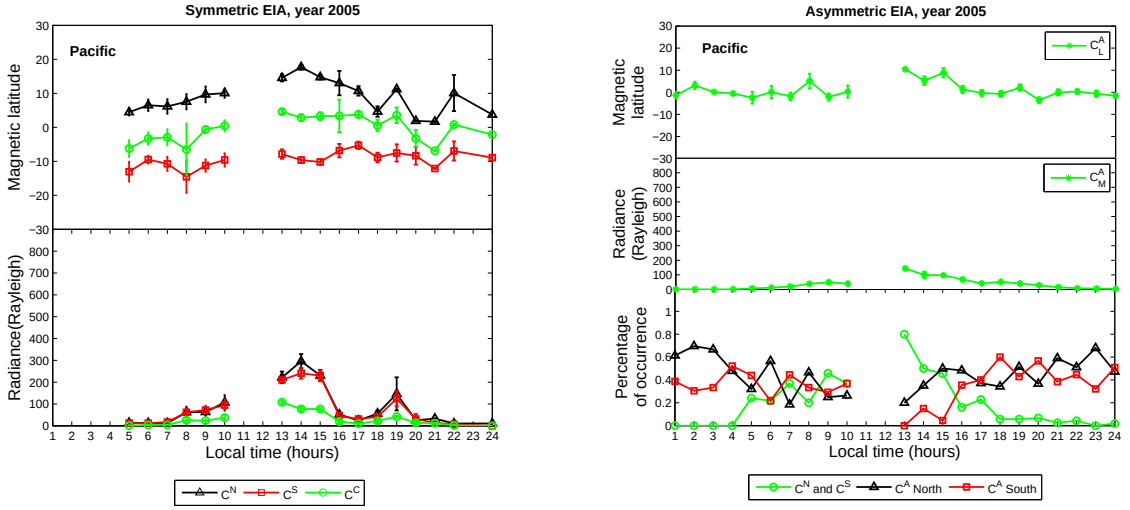

Fig. A.9: Magnetic latitude and radiance for the EIA crests and troughs in the Pacific sector, 2005 ($> 150°$ and $\leq 210°$).

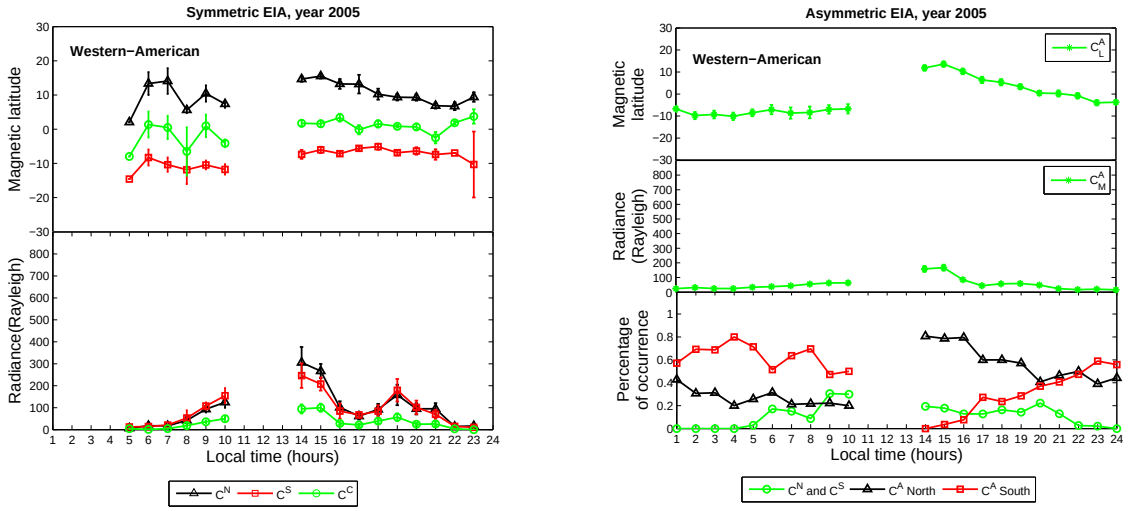

Fig. A.10: Magnetic latitude and radiance for the EIA crests and troughs in the Western-American sector, 2005 ($> 210°$ and $\leq 300°$).

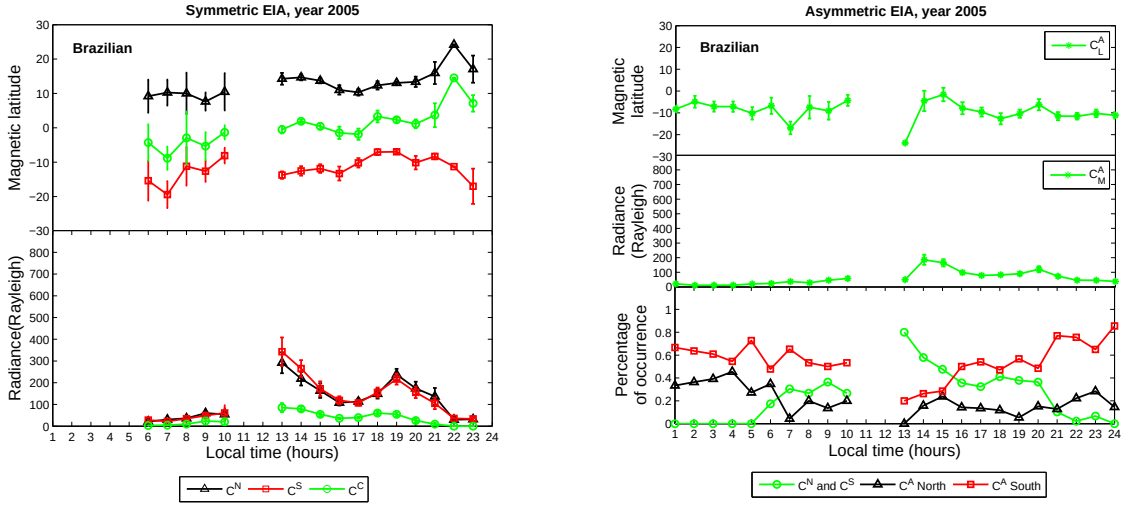

Fig. A.11: Magnetic latitude and radiance for the EIA crests and troughs in the Brazilian sector, 2005 ($> 300°$ and $\leq 360°$).

A.4 Seasonal Variation in 2005

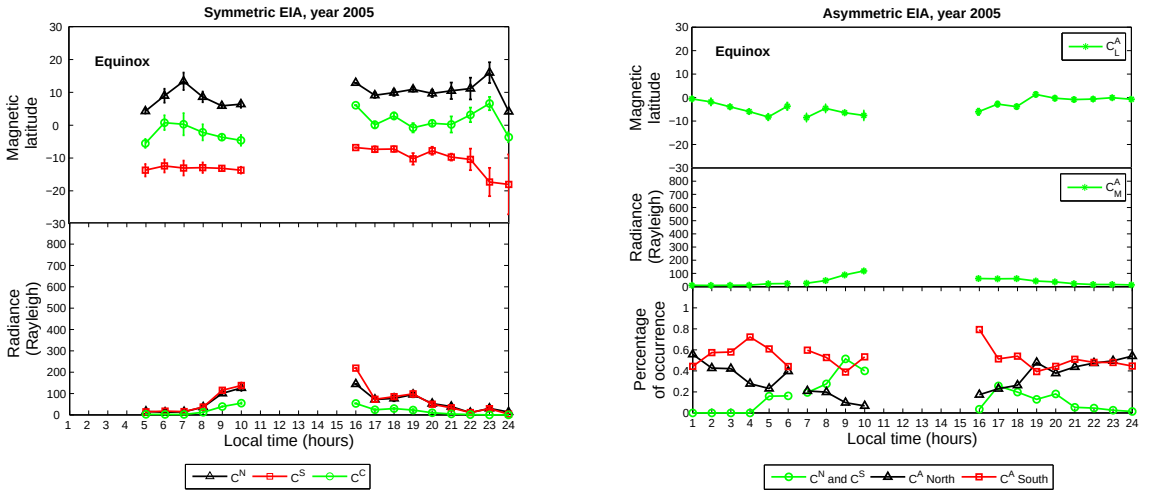

Fig. A.12: Magnetic latitude and radiance for the EIA crests and troughs during the spring and vernal equinoxes, 2005.

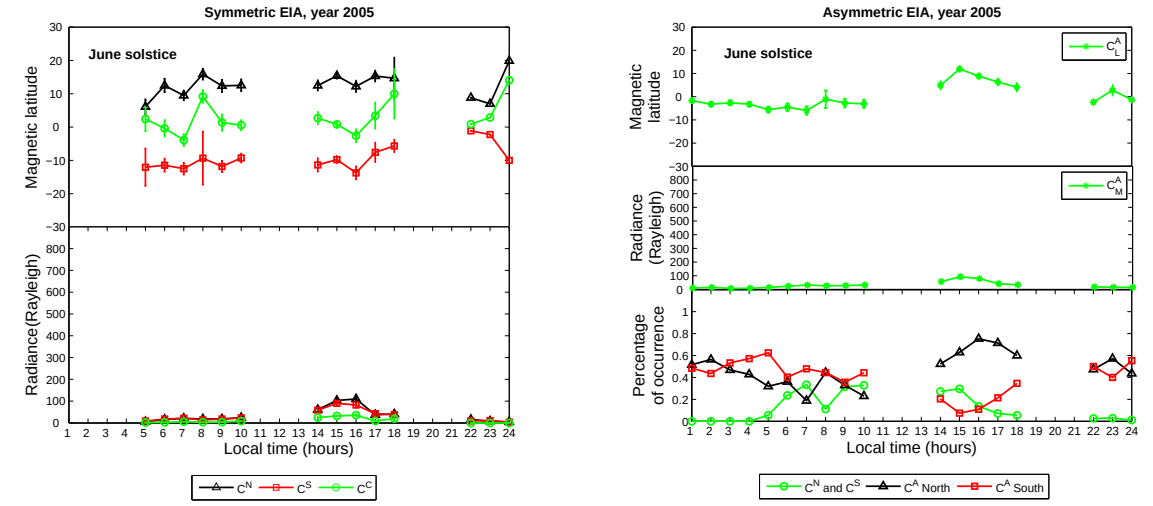

Fig. A.13: Magnetic latitude and radiance for the EIA crests and troughs during June solstice, 2005.

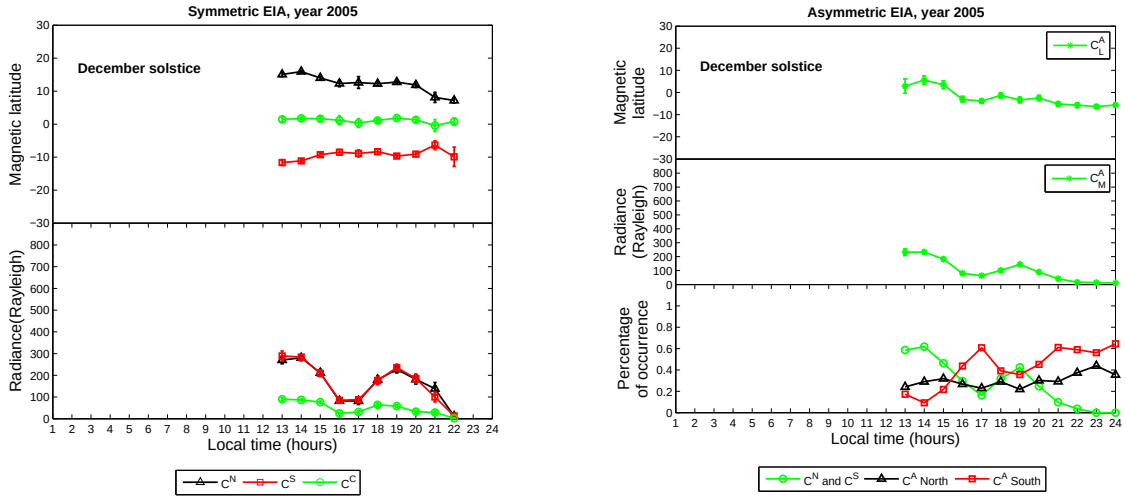

Fig. A.14: Magnetic latitude and radiance for the EIA crests and troughs during December solstice, 2005.

Appendix B

Movies with GUVI Limb Files

As mentioned in Chapter 2, movies were created for all available GUVI limb data in order to look at the day to day development of EIA with UT. Radiance from reduced limb files with the stars and glints subtracted were integrated along the higher altitude pixels spanning an altitude range of 380 to 500 km. Data from successive orbits were merged together in order to show both ascending and descending nodes of the orbit. Data was shown as a function of magnetic latitude. The corresponding 3-hour Kp indices for the previous 3-day period were plotted along with. A sample frame from the movies is shown in fig. B.1. These movies are provided in the accompanying CD.

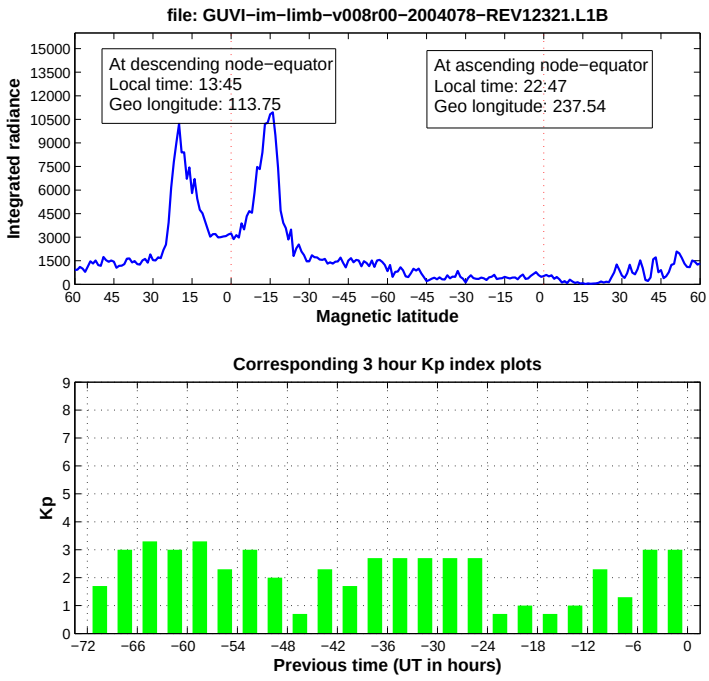

Fig. B.1: Sample frame from GUVI limb data movie for year 2004.